Johannes Emanuel Fröch, BSc

Focused Ion Beam assisted Deposition of Metals: Process-Parameters and Functionality Relationships

MASTER THESIS

For obtaining the academic degree
Diplom-Ingenieur

Master Programme of
Technical Physics

Graz University of Technology

Supervisor:
Univ.-Doz. Dipl.-Ing. Dr. techn. Harald Plank

Institute of Electron Microscopy and Nanoanalysis

Graz, March 2016

Abstract

Since its introduction, Focused Ion Beam (FIB) microscopes have evolved into a central technology for a diverse range of applications in research and development. Besides the possibilities of sub-surface investigations, 3D metrology, site-specific preparation of ultrathin lamellas for transmission electron microscopy and rapid prototyping, FIBs are widely used for device modification, as it allows localized circuit editing down to the lower nanoscale. In more detail, the latter is enabled by FIB assisted gas etching to open finished devices, followed by on-demand editing of electronic circuits via nanometer accurate deposition of conductive materials such as Platinum, Tungsten or Gold. However, latter deposits are fundamentally influenced from a high incorporation of carbon and gallium which can increase the electric resistivities up to three orders of magnitude in dependency on the preparation conditions. This, in turn, can strongly influence subsequent electric device characterization which is highly unwanted for industrial trouble-shooting. To overcome this problem, this thesis is dedicated to figure out fundamental side effects and improve the entire deposition process for electric connections in terms of reliability, predictability and reproducibility. In more detail, this study focuses on the typically used precursor materials $W(CO)_6$ and $(CH_3)_3Pt\ CpCH_3$ for the FIB based deposition of metallic structures. Comprehensive insights are gathered via a multi-disciplinary approach using Scanning Electron Microscopy (SEM), FIB Microscopy, Transmission Electron Microscopy (TEM), electron based Energy Dispersive X-ray characterization (EDX), TEM based Electron Energy Loss Spectroscopy (EELS) in conjunction with in-situ electric characterization after FIB deposition. The thesis provides a detailed insight in the relationship between deposition process parameters and final electric properties including scaling laws which have not been thoroughly investigated before. This, in turn, enabled the optimization of deposition processes together with the highly demanded predictability and reproducibility. Finally, a strategy could be derived which allows to transfer the findings to different machines via initial test experiments which leverages the findings to a generally relevant level. By that this work spans the bow from fundamental insights towards practical aspects by means of an easy-to-use guide for FIB based deposition of metallic structures in the demanding field of device modification in science and industry.

Kurzfassung

Seit seiner Einführung entwickelte sich das Focused-Ion-Beam (FIB) Mikroskop zu einem zentralen Werkzeug in vielseitigen Anwendungsbereichen der Forschung und Entwicklung. Neben den Möglichkeiten der Untersuchung unter der Oberfläche, 3D Metrologie, ortsspezifischer Präparation von ultradünnen Lamellen für die Transmission-Elektronenmikroskopie und schnellen Prototypen-entwicklung, werden FIBs auch weitgehend als Instrument zur Veränderung von Bauteilen verwendet, da es möglich ist Schaltkreise lokal bis in den niederen Nanobereich zu editieren. Im speziellen wird die letztgenannte Methode möglich durch FIB unterstützte Ätzung um fertige Bauteile zu öffnen und anschließender Editierung des elektrischen Schaltkreises durch nanometergenaues Abscheiden von elektrisch leitenden Materialen, z.B. Platin, Wolfram oder Gold. Jedoch werden letztgenannte Abscheidungen fundamental durch eine hohe Inkorporation von Kohlenstoff und Gallium beeinflusst, welche abhängig von den Herstellungsbedingungen den elektrischen Wiederstand um bis zu drei Größenordnungen erhöht. Dies wiederum kann anschließende elektrische Untersuchungen des Schaltkreises stark beeinflussen, was für die industrielle Fehlersuche höchst unerwünscht ist. Um solche Probleme zu überwinden, widmet sich diese Arbeit der Bestimmung von fundamentalen Nebeneffekten und der Verbesserung des gesamten Abscheidungsprozesses von elektrischen Leitungen bezogen auf die Zuverlässigkeit, Vorhersagbarkeit und Reproduzierbarkeit. Im speziellen werden in dieser Studie die üblichen Precursor Materialien, $W(CO)_6$ und $(CH_3)_3Pt\ CpCH_3CH3)3PtCpCH3$ zur FIB unterstützten Abscheidung metallischer Strukturen untersucht. Umfassende Einblicke werden durch einen multidisziplinären Ansatz erlangt, mittels Rasterelektronenmikroskopie, FIB Mikroskopie, Transmissionselektronenmikroskopie (TEM), Elektronenbasierte energiedispersive Röntge-ncharakterisierung, TEM basierte Energieverlustspektroskopie in Verbindung mit in-situ Charakterisierung der elektrischen Eigenschaften nach dem Abscheidungsprozess. Diese Arbeit gibt einen detaillierten Einblick in die Beziehung zwischen den Abscheidungsparametern und den elektrischen Eigenschaften, einschließlich einem Skalierungsgesetz, welches bisher nicht vollständig untersucht wurde. Dies wiederum erlaubte die Optimierung der Abscheidungsparameter mit der erforderten Vorhersagbarkeit und Reproduzierbarkeit. Schlussendlich konnte eine Strategie abgeleitet werden, welche es erlaubt die Ergebnisse auf andere Geräte durch ein Testexperiment zu übertragen, wodurch die Ergebnisse auf ein generell relevantes Level gehoben werden. Schlussendlich spannt diese Arbeit einen Bogen von fundamentalen Erkenntnissen zu den praktischen Aspekten, mit Hilfe einer Benutzerfreundlichen Anleitung zur FIB unterstützten Abscheidung von metallischen Strukturen im anspruchsvollen Feld der Gerätemodifikation für Wissenschaft und Industrie.

Acknowledgements

First of all I thank Prof. Ferdinand Hofer, head of the institute, for giving me the chance to do my master thesis at Institute for Electron Microscopy and Nanoanalysis.

I would also like to thank Dr. Michael Rogers, head of the work group at ams AG, who made it possible for me to do my thesis in cooperation with ams AG.

My greatest appreciation goes to my supervisor Univ.-Doz. Harald Plank for his support, for trusting me and giving me the freedom to follow my ideas, while still guiding me into the right direction. Especially I thank him for always supporting and motivating me, and his great enthusiasm. Also I thank him for being part of his work group S^3. And I am grateful to every member of the S^3 work group, Sebastian Rauch, DI Robert Winkler, DI Thomas Ganner, DI Jürgen Sattelkow and Ulrich Haselmann. I am just thankful to have met such awesome guys.

Furthermore, I am grateful to Dr. Thomas Haber, my supervisor at ams AG, for his support and encouragement. I thank him for accepting me into the FIB team and for his trust. I especially appreciate his critical approach, which widened my general perspective. Moreover, I would like to thank him for his big patience with me!

I thank the FIB team at ams AG, Melanie Fuchs, DI Dominik Kastner and DI Thomas Stermitz for providing me with know-how and ideas for my work.

My deepest gratitude goes to DI Angelina Orthacker for performing the TEM measurements and help with the interpretation of the results. And also because she is awesome.

My gratitude goes as well to all the FELMI staff members and the staff at ams AG for help and advice when I needed it.

I am deeply thankful to my closest friends who were always standing by my side. I want to thank each and every of them for just being there for me, not only during the time of this thesis but always. And I am thankful to all the good times and bad times I could spend with them.

Finally, I want to thank the persons who have known me the longest - my parents, Luise and Wolfgang, my brother Christopher, and my sisters Anna and Lisa. I am so happy to have them and I am more than grateful that they are always there for me. Without all their love and support I would never have come this far, therefore my biggest and deepest gratitude goes to them.

Table of Contents

1 Introduction ... 7
2 Instrumentation ... 9
2.1 Dual Beam Microscope (DBM) ... 9
2.1.1 Basic Concept ... 9
2.1.2 Fields of Application ... 9
2.1.3 Setup of a Dual Beam Microscope ... 12
2.1.4 Scanning Electron Microscope (SEM) ... 13
2.1.5 Electron Source and Lenses ... 14
2.1.6 Electron – Matter Interaction and Detection ... 14
2.1.7 Image Formation, Magnification and Resolution Limit ... 17
2.1.8 Focused Ion Beam (FIB) ... 19
2.1.9 Ion beam – Matter Interaction and Detection ... 20
2.1.10 Patterning ... 21
2.1.11 Particle Assisted Deposition ... 22
2.1.12 Electrical Transport ... 26
2.2 Transmission Electron Microscopy ... 27
2.3 Prober Shuttle ... 28
2.3.1 Technical Setup ... 28
2.3.2 4 Point Measurement Principle ... 28
2.4 Previous Works ... 29
2.4.1 Side Effects ... 29
2.4.2 Deposition Process ... 29
3 Experiments and Results ... 31
3.1 Side Effects ... 32
3.1.1 Introduction ... 32
3.1.2 Specifications ... 32
3.1.3 Investigations on the Volume Growth Rate (VGR) ... 35
3.1.4 Position and Sequence Related Effects ... 39
3.1.5 Deposit Proximity Effects ... 40
3.1.6 Side Effects Summary ... 42
3.2 Functionality ... 43
3.2.1 Introduction ... 43

3.2.2 Substrate / Test Structure 43

3.2.3 Probe Pads 43

3.2.4 Resistance Measurement 45

3.2.5 Dwell Time (DT) Variation 48

3.2.6 Overlap 51

3.2.7 Defocus 52

3.2.8 Relation between Resistance, Resistivity and Volume Growth Rate 54

3.2.9 Tungsten 55

3.2.10 Height and Length Dependence 58

3.2.11 Internal Structure and Chemistry of Pt and W Based Deposits 61

3.2.12 Final Comparison between Pt and W 64

3.2.13 Uncertainty 65

3.2.14 Functionality Summary 65

3.3 Easy to Use Guideline and Spreadsheets 66

3.4 High Current Induced Functionality Tuning 70

4 Summary and Outlook 73

5 Appendix 75

5.1 Appendix 1 – Spreadsheet for calculating the empirical parameters 75

5.2 Appendix 2 – Spreadsheets for updating the diagrams 75

List of Abbreviations

BSE … *back scattered electrons*

BSI … *back scattered ions*

CCD … *charge coupled device*

CE … *circuit edit*

D_{pt} … *point dose*

D_{tot} … *total ion dose*

d_B … *beam diameter*

DBM … *dual beam microscope*

DF … *defocus*

DT … *dwell time*

EDX … *energy dispersive x-ray spectroscopy*

EELS … *electron energy loss spectroscopy*

EFTEM … *energy filtering transmission electron microscopy*

ESA … *excited surface atoms*

ETD … *Everhart Thornley Detector*

FA … *failure analysis*

FEB … *focused electron beam*

FEBID … *focused electron beam induced deposition*

FIB … *focused ion beam*

FIBAD … *focused ion beam assisted deposition*

FWHM … *full width half maximum*

Ga … *gallium*

GIS … *gas injection system*

HAADF … *High angle annular dark field*

IC … *integrated circuit*

ICE … *ion conversion and electron detector*

IEE … *insulating enhanced etch*

LMIS … *liquid metal ion source*

OL … *overlap*

PoP … *point pitch*

Pt … *platinum*

ROI … *region of interest*

RT … *refresh time*

SE … *secondary electrons*

SEM … *scanning electron microscope*

SI … *secondary ions*

STEM … *scanning transmission electron microscope*

TEM … *transmission electron microscope*

TET … *total exposure time*

VGR … *volume growth rate*

W … *tungsten*

XS … *cross sectioning*

1 Introduction

Since the development of integrated circuits (**IC**) it was possible to observe how these building blocks of our devices became smaller and smaller, which even follows a certain mathematical expression, known as Moore's law [1]. Along with the miniaturization of ICs, more and more application fields were conquered which developed into integral and essential parts in the field of automotive, mobile electronics or industrial monitoring. However, with the development of faster, smarter and smaller ICs also longer development times arose, resulting in higher costs and higher error rates, simply because such devices become progressively complicated in their layout and functionality. The costs for design and development of new devices sometimes exceeds 10 mil. €, thus errors during the development should be solved as quickly as possible during initial stages. But debugging may not be always easy and straightforward, sometimes parts of an IC actually have to be completely redesigned, to obtain the desired functionality. In semiconductor industry this would imply new sets of lithography masks in a trial and error fashion until the final and ideal design is found. This would result in considerably long time-to-market and cause enormous costs. However, this is luckily not the case, as there are certain high-end development tools which allow on-demand manipulation of ICs in the micro - and nanometer range, enabling circuit design without the usage of many different masks.

One such tool is the dual beam microscope (**DBM**), a combination of scanning electron microscope (**SEM**) and focused ion beam microscope (**FIB**). By integration of both microscopes into the same machine versatile fields of application have arisen, e.g. ultrathin lamella preparation for transmission electron microscopy (**TEM**), site specific failure analysis by slice-and-view approaches as well as direct-write rapid prototyping [2]. This is made possible by one of the main features, the potential to modify material down to the nanometer scale, which can be done both subtractive and additive by means of sputtering, gas assisted etching and gas assisted deposition using precursor gases. While structuring with the FIB, the process itself can be observed *in-situ* using the SEM or vice versa, hence giving the FIB the status of a nano-scalpel.

For a semiconductor manufacturer this feature is of high interest, as it makes it possible to physically edit an IC up to a certain degree, thus advancing the debugging process. Therefore, the DBM has become an essential tool for most semiconductor manufacturers, as it is used for device modification in the initial stages of the development of novel ICs, effectively reducing time-to-market and overall cost. For the aspect of device modification, especially the on-demand deposition of conducting leads plays an important role. Unfortunately, process related circumstances will always lead to an incorporation of carbon (up to 90 at %) and gallium (up to 28 %) in such deposits [2,3]. It has been shown that this factor significantly increases the resistivity, which can be up to 3 orders of magnitude higher, than the value for the respective bulk material [3]. This property can significantly influence the final functionality of a device, specifically when the modified device is an analog circuit, thus making the knowledge of the resistance crucial, as the signal strength in such a circuit strongly depends on it. Hence, for the practical application of such metal deposits, the information of the absolute resistance, which is a function of the resistivity and the volume of the deposit, is inevitable.

However, most studies undertaken within this field focus either on the improvement of the resistivity itself, low dimensional connections (i.e. nanowires) or curing and purification of nanostructures [2,4,5,6]. In the last decade remarkable results have been achieved in these fields, which certainly

show that such structures could be used as sensors, post-deposition purification is possible, and many other things [2]. However, for circuit edit, the question of a most efficient procedure, i.e. having the least effort with highest outcome, in particular the lowest possible total resistance of a connection in the shortest time, is of highest interest.

Therefore, this master thesis was set up in cooperation with ams AG [7] with the dedicated goal to find the parameter set for the most efficient, reliable and reproducible metal deposition process.

2 Instrumentation

2.1 Dual Beam Microscope (DBM)

2.1.1 Basic Concept

The dual beam microscope (**DBM**) enables a broad variety of applications by its combination of a focused ion beam (**FIB**) and a scanning electron microscope (**SEM**). These two main components have a similar principle of operation and will be discussed thoroughly in section 2.1.4 and 2.1.8. The FIB is mostly used to locally remove material via sputtering while it is possible to use the SEM for high resolution imaging and simultaneous visualization of FIB related processes. Additionally, both particle beams can, in combination with a gas injection system (**GIS**), be used for deposition and etching. A theoretical imaging resolution for electrons and ions in the range of 1 nm and 5 nm, respectively, and the fast handling make the DBM an incomparable mask-less high resolution 3D micro and nano-processing tool, like no other instrument. In Figure 1 (a) an example of subtractive structuring using FIB milling of a gold film on SiO_2 is shown, next to it, Figure 1 (b) shows an example of additive 3D structuring using the electron beam for deposition of Pt-C.

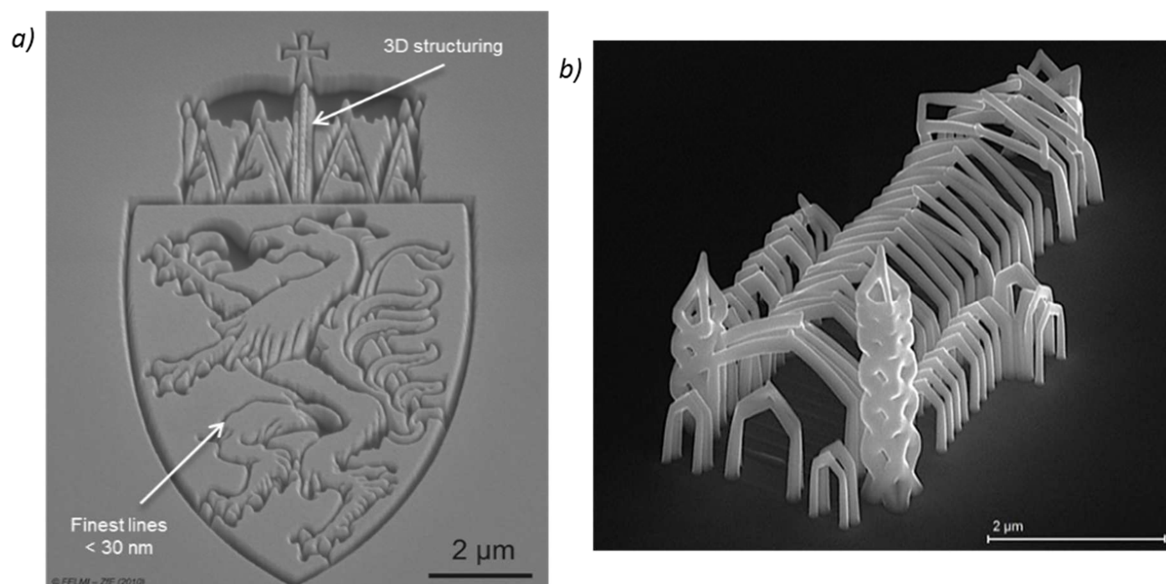

Figure 1: a) using the FIB as a nano scalpel to modify a gold film on SiO_2 with 3D features and line widths below 30 nm [2,8,9]; b) using the electron beam as a mask-less 3D nanofabrication tool to create a model of the Herz-Jesu-Kirche (Graz, Austria) with branch diameters of about 60 nm [10].

2.1.2 Fields of Application

In commercial use for a semiconductor manufacturer the DBM is typically used equally in the fields of failure analysis (**FA**) and circuit edit (**CE**). The techniques of FA are cross sectioning (**XS**), slice-&-view, ultrathin lamella preparation for TEM, energy dispersive x-ray spectroscopy (**EDX**) and electrical measurements. Cross sectioning is the site specific investigation of the sample. Therefore, the material in the vicinity of the region of interest (**ROI**) is removed via FIB milling, subsequently the cross section is imaged and investigated with the SEM (Figure 2 (a)). If this process is done continuously one can reconstruct the 3D structure of the removed volume, this process is called slice-&-view (Figure 2 (c)). In case the resolution with the SEM is still too low, then an analysis with a transmission electron

microscope (**TEM**) is necessary. In order to do so the ROI has to be extracted from the sample and is continuously thinned with the FIB until an appropriate thickness is achieved (Figure 2 (b)). To obtain information about the chemical composition, one can use EDX, which can be used in combination with XS or slice-&- view (Figure 2 (d)) to access chemical information with 3D character. With an additional Prober shuttle electrical measurements, like 4 point measurements or electron beam induced current measurements can be performed within the microscope (see section 2.3.2). With these techniques it is possible to identify physical defects and manufacturing errors.

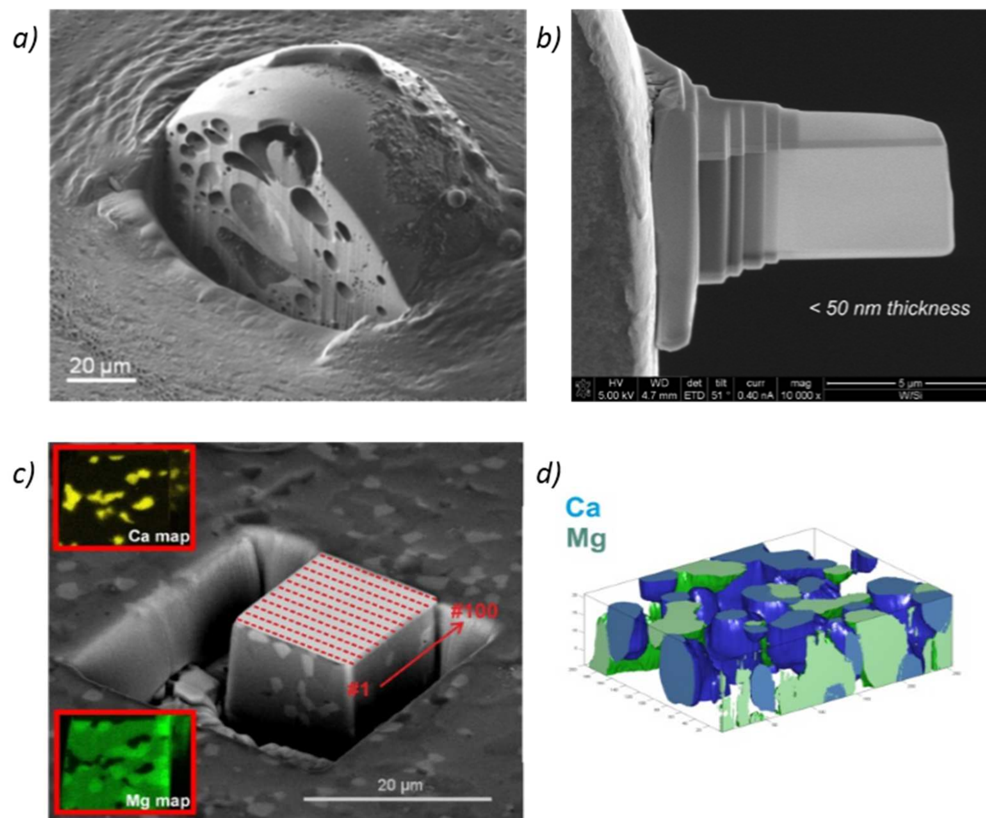

Figure 2: a) a cross section for site specific failure analysis; b) a TEM lamella, fabricated by FIB with a final thickness of less than 50 nm; c) slice-&-view of a via, sequential sputtering of layers via FIB; d) the distribution of Ca and Mg in a volume, reconstructed by combination of slice-&-view and EDX.

By means of CE it is possible to modify an integrated circuit (**IC**) up to a certain degree, which is done to figure out flaws in the design. The possibility of CE became an important key feature of DBMs, since instead of generating new sets of masks until the optimal design is found, an IC can be edited until the device shows the desired functionality. To emphasize the importance of this step a diagram of the design-to-market process of a novel IC is shown in Figure 3. It shortens the time-to-results and time-to-market by a considerable factor, therefore, saving a considerable amount of costs.

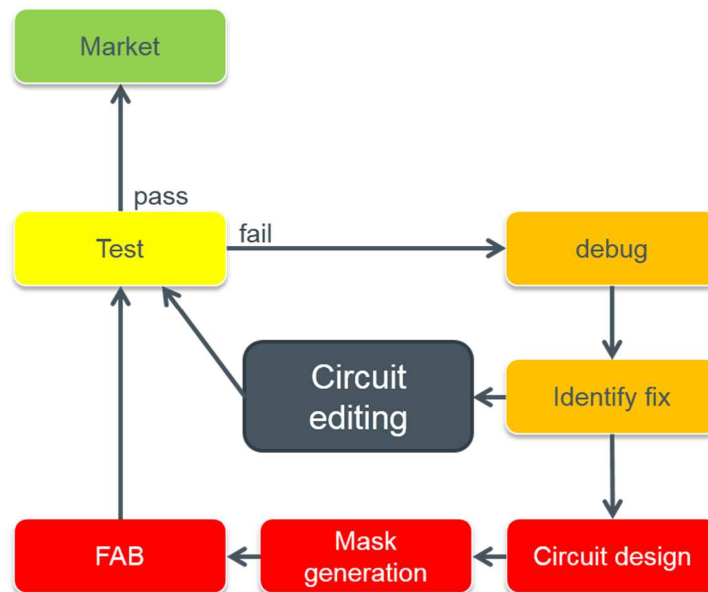

Figure 3: the role of circuit editing during the development of a novel IC (starting bottom right). Time-to-results and time-to-market is considerably shortened by CE.

During the process of CE an IC can be modified by separating (Figure 4 (a)), shorting or connecting metal lines(Figure 4 (b)), placing new vias between metal layers or deposition of probe pads (Figure 4 (c)) for site-specific-electrical probing, which makes it possible to address only a certain part of the whole IC via an electrical prober, instead of measuring and evaluating the whole device. All these processes have one common initial step, which is etching away the topmost passivating layer. This layer shields the metal layer of the device from any environmental influence. By means of gas assisted etching (XeF_2) a small area is etched and subsequently modified, a detailed description of the etching process is given in section 2.1.11.2. Functional modifications can be done by means of gas assisted deposition of metal containing precursors, like tungsten (**W**) or platinum (**Pt**) or deposition of insulating material like SiO_2 , which is discussed thoroughly in section 2.1.11.

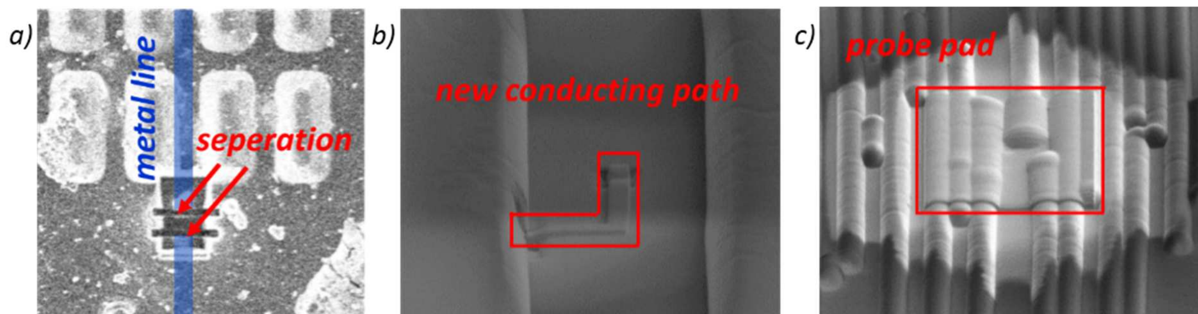

Figure 4: a) separation (red) of a metal line (blue) in order to rewire it at another position; b) a new conducting path (red frame) is deposited c) deposition of a probe pad (red frame) for subsequent electrical tests of specific areas of an IC [11].

2.1.3 Setup of a Dual Beam Microscope

The DBM used for this thesis is a Helios NanoLab 650 [12], shown in Figure 5 (a), the SEM column is built in vertically, while the FIB column is built in tilted with respect of 52° to the SEM column. Both particle beams coincide in one special point, which is called "eucentric height" (Figure 5 (b)). Positioning the sample to this special position enables simultaneous operation with both particle beams. This means that observation of FIB related processes with the electron beam becomes possible. Furthermore, the point in focus will stay in focus for both particle beams, if the stage is tilted. Therefore, the common procedure to find the eucentric height is to focus the electron beam on a sample feature, tilt the stage and move the stage in z direction until this distinct feature is in the center of the electron beam. The eucentric height defines the working distance for both particle beam columns, which is approximately 4 mm for the SEM and 16.5 mm for the FIB (for the Helios NanoLab 650). All additional features, like GISs, EDX detector, micromanipulator and others are specifically aligned to the eucentric height to ensure simultaneous DBM processing, Figure 5 (c).

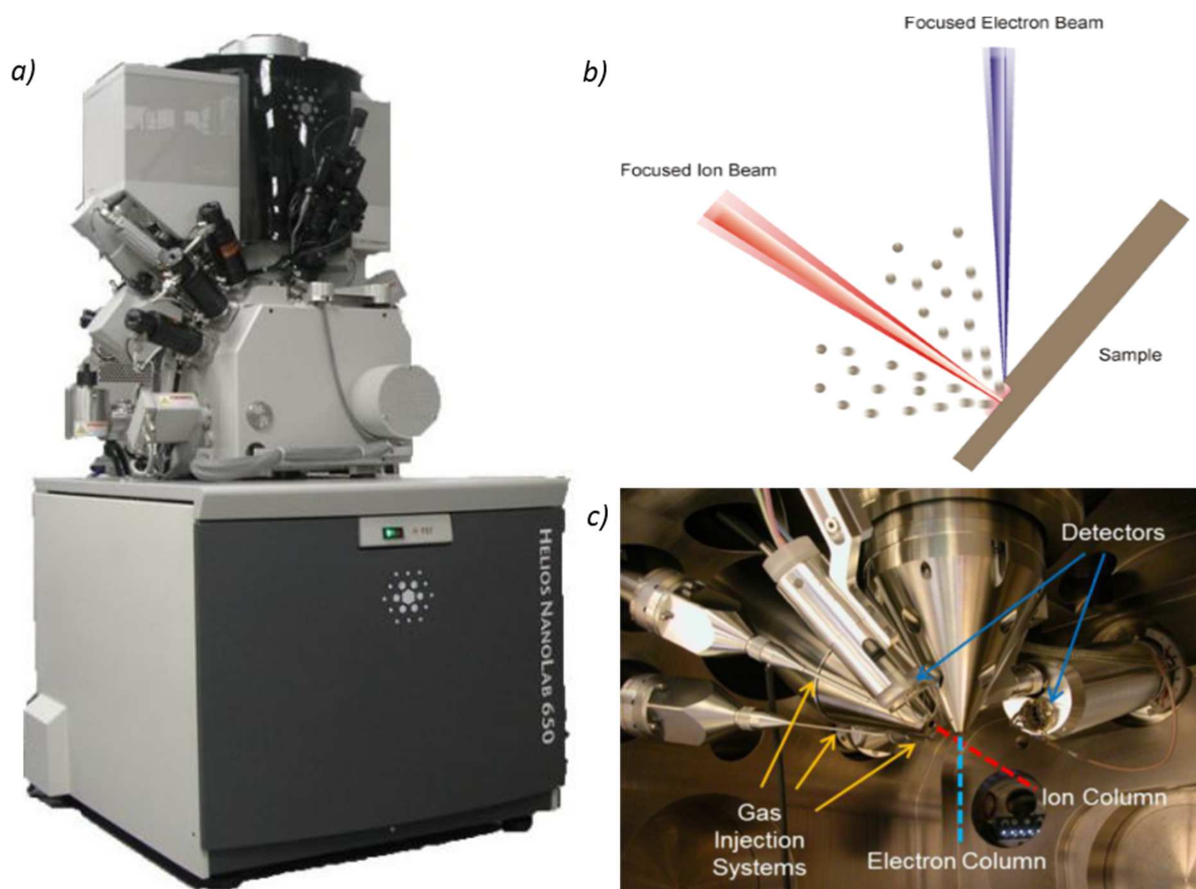

Figure 5: a) the used FEI Helios NanoLab 650 DBM; b) both particle beams coincide at one point, which defines the eucentric height; c) the inside of a DBM, showing the beam columns, detectors and several GIS.

The sample chamber is kept under high vacuum by a pump system consisting of a rotary vane pump and a turbo molecular pump, resulting in a base pressure between $7x10^{-6}$ and $2x10^{-5}$ Pa. The vacuum systems for beam columns are discussed in the respective sections. Additionally, attached to the sample chamber is a so called quick-loader, which enables loading of the sample chamber without

breaking the chambers working vacuum, increasing the sample throughput of the DBM. However, the quick-loader limits the lateral sample size to 32 mm while bigger samples and additional equipment, like a prober shuttle, can only be loaded by opening the entire chamber, resulting in a break-down of the base pressure.

2.1.4 Scanning Electron Microscope (SEM)

The theoretical limit of resolution for any microscope is given by the Rayleigh criterion (equation 1), stating that the smallest distance δ that can be resolved is a function of the wavelength λ, the refractive index n and the semi-angle of collection β. One can see from the Rayleigh criterion that in general the resolution can be improved with a shorter wavelength of the probing particle.

$$\delta = \frac{0.61\,\lambda}{n\,\sin(\beta)} \qquad (1)$$

Theoretically, a value in the range of several pm would be possible with a high energetic electron beam. An additional advantage of an electron beam is the interaction with the sample which allows analytical characterization of the material. However, the limitation of the resolution is determined by the interaction of the electron beam with the sample and lens aberrations, both discussed below. The schematic diagram of a SEM is shown in Figure 6. At the top, electrons are emitted from a source, then guided through a lens system onto the sample. The interaction of the beam with the sample generates a signal, which is registered by a detector together with the spatial position of the scanning electron beam. In the following section a brief discussion of the column components and sample interaction are given. One can find a more detailed explanation and further information on the here rather shortly discussed topics in literature [2,13].

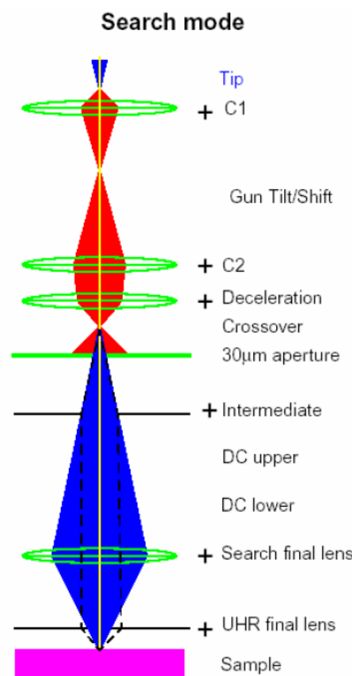

Figure 6: schematic diagram of a SEM, showing the lens system (green), the electron beam (red) passing through the condenser lens system (C1 and C2) and the electron beam (blue) passing the objective lens. [12]

2.1.5 Electron Source and Lenses

At the top of the column electrons are emitted from a source, for the used SEM a field emission gun. A heated tungsten tip is placed in a strong electric field which is then called Schottky emitter. At the very end of the tip the electric field (governed by the small tip radius) becomes so high that electrons are able to tunnel through the potential barrier and can leave the tungsten tip assisted by the elevated tip temperature. They are subsequently bundled with a Wehnelt cylinder into the 1st crossover, which can also be seen as the virtual electron source of the SEM. By changing the acceptance aperture of the 1st crossover the beam current can be varied in a range from 0.8 pA to 26 nA. Subsequently electrons are accelerated to an energy of 30 keV and guided through the condenser lens system, reducing the size of the electron beam and aligning it parallel and in the center of the main optical axis. After going through the second condenser lens the electron beam is decelerated to the final beam energy (1 – 30 keV) and focused through another aperture. In the following section of the SEM column the beam is guided through two duplex lenses, which change the direction of the beam in X and Y direction, enabling rastering of the sample. Furthermore, these lenses are used to compensate axial astigmatism, which is discussed later on. Finally the beam passes the objective lens, which focuses it on the surface, referring to it as focused electron beam (**FEB**). Due to the relatively long distance from source to sample, the electron column must be kept under high vacuum in order to achieve a long mean free path to minimize scattering of the electrons. The impinging electron beam at the sample surface is not confined to a single spot but typically has a Gauss-like intensity distribution. The diameter of the beam on the sample surface is defined as the full width at half maximum (**FWHM**) of this intensity distribution.

2.1.6 Electron – Matter Interaction and Detection

After the electrons are guided through the column they will impinge on the surface of the sample and enter the bulk, where they interact with the atoms and electrons of the sample elastic and inelastic. In both cases they will change their direction, which leads to an unavoidable broadening of the formerly confined beam, thus the electrons spread out in the sample and form the interaction volume, depicted in Figure 7 (a). The size of the interaction volume depends mostly on the primary beam energy, mean atomic number and density of the bulk material and is typically determined by means of Monte Carlo simulations. The interaction volume itself can be seen as the origin of various effects, i.e. secondary electrons, backscattered electrons, Auger electrons, as well as x-ray and light from a more abstract point of view. The energy distribution of re-emitted electrons is shown in Figure 7 (b).

For elastic scattering (Rutherford scattering) the deflection angle can be quite high and therefore subsequent elastic scattering can lead to resurgence of the electrons. Those electrons will have lost only a small fraction of their energy and are referred to as back scattered electrons (**BSE**). The intensity of the BSE signal is a function of the mean atomic number in the material, thus this signal can be used to depict material contrast in the image. BSE typically spread from a larger lateral range (compare blue and red paths in Figure 7 (a)), hence the resolution is low compared to other signals. A slightly different propagation type of elastic scattering can be found in crystalline or poly crystalline materials, at which the electron wave interacts with the lattice, thus leading to diffraction. Inelastic interaction will change the direction and will as well lead to a change in energy of the electrons. The major processes of inelastic scattering is ionization of inner shells and collisions with weakly bound electrons. Subsequently these electrons will leave the atom and can exit the sample surface, and will be referred

to as secondary electrons (**SE**) and typically show energies below 50 eV. As a consequence the mean free path is short and only near surface SE (< 5 nm) are able to exit the bulk. Together with the fact that the yield of SEs is higher than for any other species, they are predominantly responsible for the image formation. A further follow up process of ionization is the recombination of electrons, resulting in the emission of characteristic x-ray or Auger electrons [2,13].

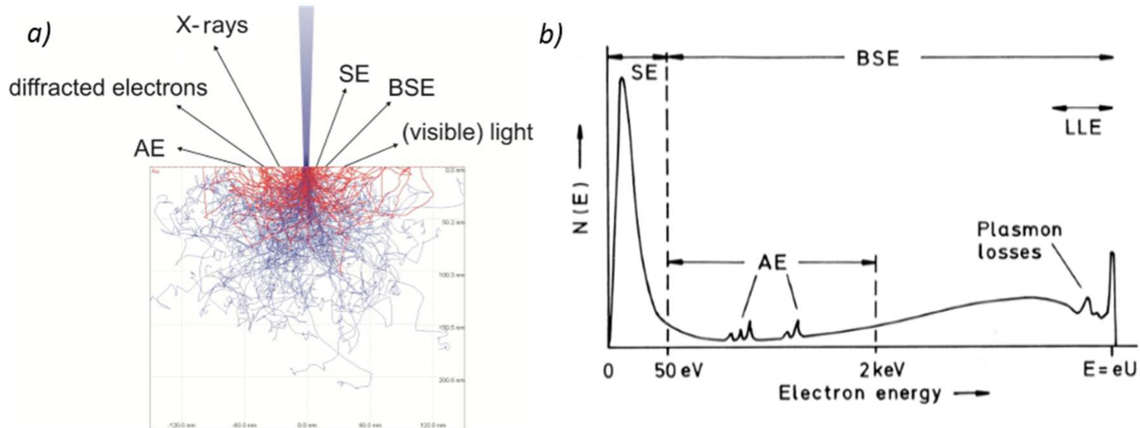

Figure 7: a) Monte Carlo simulation of the electron propagation in a bulk sample which shows the broadening of the primary beam including the differentiation to BSE (red paths); b) energy distribution of electrons as they are leaving the sample after interaction. The depicted signals are secondary electrons (SE), auger electrons (AE), back scattered electrons (BSE), low loss electrons (LLE). The maximum energy of the electrons is determined by the acceleration voltage of the primary beam (marked in the diagram as E=eU) [8].

For detection of SE and BSE an Everhart Thornley detector (**ETD**) is typically used. It takes advantage of the energy spectrum of the electrons to distinguish between SE and BSE. The setup of the ETD is shown in Figure 8. For SE detection, electrons are attracted by a positively biased cage, which bundles them onto a scintillator. The generated signal in the scintillator is then guided into a photomultiplier tube, where it is enhanced and then processed. If the cage is negatively biased electrons with a low energy, like SE, are not able to reach the scintillator, since their path is deflected away from the collector grid. However, electrons with higher energies such as BSE are still able to generate a signal at the scintillator. The ETD is mounted at a certain tilt angle, which leads to a "shadow effect", thus giving surface features a 3D character in the final image.

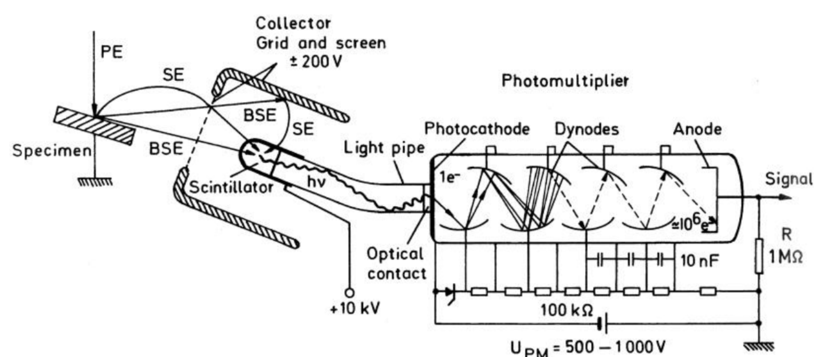

Figure 8: Schematic diagram of the Everhart Thornley detector. Also shown is the detection mechanism for SE and BSE.

As described above the interaction of the primary beam with the target atoms can lead to ionization of inner shells, i.e. an electron is removed from an inner shell. Subsequently, an electron from a higher orbital drops into this vacant position and energy in form of a photon or an Auger electron is emitted, the process is illustrated in Figure 9 (a). Since the electron orbitals have distinct energies, which are also element specific, this signal can be used to identify the materials in a sample and subsequently determine the chemical composition by evaluating this signal, considering several factors. Besides characteristic also x-rays with continuous energies appear, known as Bremsstrahlung, due to the deceleration of the electron in the coulomb field of the nuclei, which leads to the emission of energy in form of a photon, also represented in figure 9 (a). Since the deceleration doesn't have specific energies it appears as continuous in the spectrum. A typical spectrum of characteristic and continuous x-ray is depicted in Figure 10, at which the contribution of the signals are the red and blue filled areas, respectively. By comparing the peaks of characteristic x-rays with a given data base one can identify the elements present in the sample. For detection a silicon drift detector is used, at which the generated signal is proportional to the energy of one x-ray photon. In front of the sensor a window ensures that vacuum inside the detector is sustained and to protect the sensor from any kind of deposition. However, the detector window itself will absorb a considerable amount of low energy x-ray, which complicates the interpretation of an EDX spectrum. Furthermore, the intensity of x-rays generally decreases with increasing energy and is finally limited by the primary beam energy. In addition to that, complications arise for non-flat surfaces, as this considerably changes the EDX spectrum. These factors make the quantification of EDX spectra a very delicate topic, therefore full quantification was not undertaken. To obtain information only close the surface, an electron beam with a primary energy of 5 keV was used. Monte Carlo simulations with the software package CASINO [14], as representatively shown in Figure 10 Figure 9 (b) for a sample containing carbon (black), platinum (blue) and gallium (red) show the intensity distribution of generated x-rays as a function of depth below the surface. One can see that x-rays stem from a 150 nm region underneath the surface. Similar simulations have shown the same depth of origin for C-W-Ga deposits.

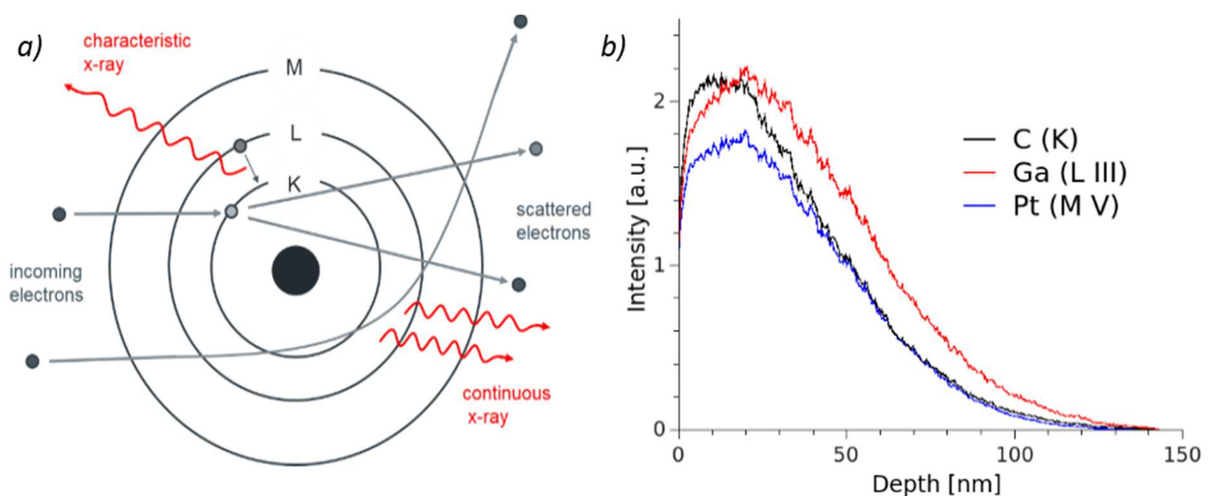

Figure 9: a) generation of characteristic x-ray by recombination of an electron into an inner shell and the generation of continuous x-ray due to deceleration; b) a simulation, using CASINO [14], shows that for the investigated deposits and a primary beam energy of 5 keV a depth of origin for the x-rays of up to 150 nm is possible.

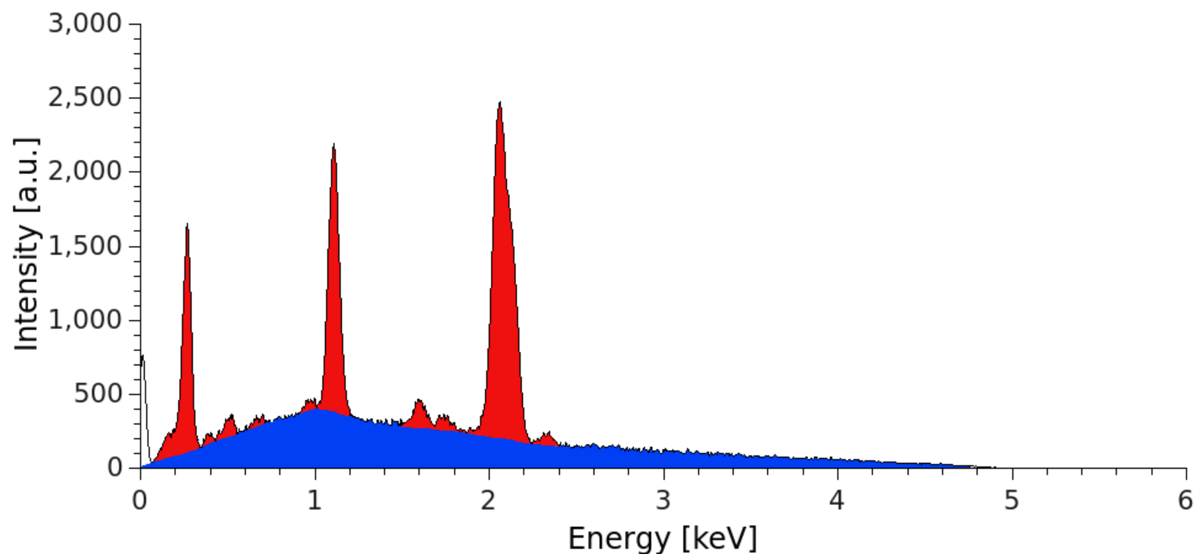

Figure 10: a typical x-ray spectrum showing continuous Bremsstrahlung (blue) and characteristic peaks (red), due to the presence of certain elements. Identifying the positions of the characteristic peaks and comparing them with a data base makes it possible to identify the elements present in the sample.

2.1.7 Image Formation, Magnification and Resolution Limit

Focusing the beam on the surface leads to the generation of the previous mentioned signals due to the electron-sample interaction and can be detected to gain either morphological or analytical information. If the beam is systematically scanned over the sample surface and the intensities are recorded for any XY position, the information can then be depicted by different levels of a gray scale which ultimately forms the image. If the intensities are too low and the signal-to-noise ratio is low, the pulse duration can be increased to obtain images with better contrast. It is also possible to integrate the intensity or average over several frames, also resulting in a better signal to noise ratio. However, one has to be aware of the intrinsic sample and stage drift, which can lead to a worse resolution for too high recording times.

By decreasing the scanning area and the point to point distance between the spots of irradiation, the magnification of the image is increased. To obtain a representative picture of the sample the pixel size ought to be the size, or smaller than the beam diameter. Otherwise the signal is only representative for the center of the pixel. On the other hand the maximum magnification is limited to the beam size. Since a certain amount of pixel is necessary to even obtain an image, the beam size should be significantly smaller than the image width.

As already mentioned, the SEM is able to achieve higher resolution than a light microscope due to its considerably lower wavelength of electrons. According to the Rayleigh criterion (equation 1) this resolution limit could be in the pm range which, however, is barely achievable on bulk samples. This can be regarded to two factors: the interaction volume and consecutive effects (discussed above) as well as lens aberrations. There are many types of aberrations which lead in practice to a final resolution in the nm range. The most important, briefly discussed here, are the diffraction error, the spherical aberration, the chromatic aberration and the axial astigmatism.

The *diffraction error* occurs due to the wave character of the electrons, is proportional to the wavelength and unavoidable. If a wave is directed through an aperture, which are crucial in the beam column, then diffraction will lead to broadening of the beam and a Gauss-like intensity distribution, as shown in Figure 11 (a).

Spherical aberration is the result of different focus points for far-off axis electrons, shown in Figure 11 (b). It is possible to correct this lens aberration with a Cs corrector, which is not integrated in the used platform.

The *chromatic aberration* appears as a consequence of the energetic spread of the electron beam. Electrons with different energies have a different point of focus, shown in Figure 11 (c).

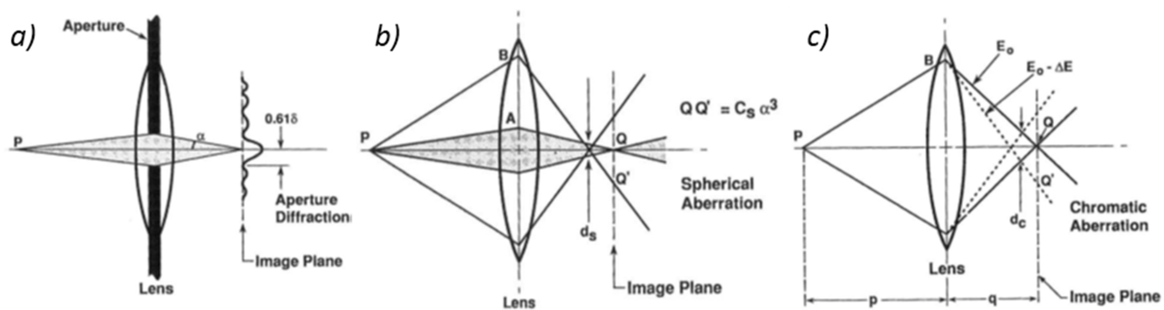

Figure 11: the principle of the diffraction error (a), spherical aberration (b) and chromatic aberration (c) as described in detail in [13].

Although the quality of electron lenses increased significantly since the first electron microscopes were built, lenses are still not perfect and additionally interfering fields may as well influence the particle beam. Hence they are differently deflected in X and Y direction, resulting in a distortion of the image in a specific direction, called axial astigmatism. This aberration can be relatively easily compensated by a lens system of at least four poles. The principle of this effect is schematically shown in Figure 12 (a), in this case the horizontal plane deflects the path of the electrons stronger compared to the vertical plane. During operation with the SEM this effect results in images like Figure 12 (b), for comparison the same image is shown when axial astigmatism is corrected in Figure 12 (c).

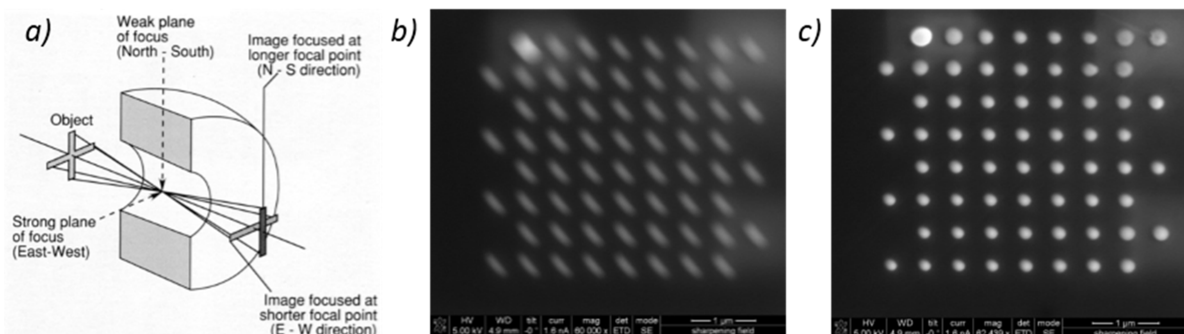

Figure 12: the principle of axial astigmatism (a), comparison of a strongly astigmatic SEM image (b) with a corrected image (c).

2.1.8 Focused Ion Beam (FIB)

The setup of the focused ion beam is basically the same as for the SEM, as schematically shown in Figure 13 (a). The particle source in the used DBM is realized by a gallium liquid metal ion source (**LMIS**), shown in Figure 13 (b). A reservoir filled with gallium is heated above its melting point (29.8 °C), which leads to wetting of an integrated tungsten needle with liquid Ga and formation of a droplet at the tip of the needle, with a special shape, referred to as Taylor cone, with a final size in the nm range at the apex [2,15]. Below the tungsten tip are extractor electrodes, biased with a high potential, resulting in a high electric field in the vicinity of the Taylor cone of about 10^8 V/cm. Because of the high curvature at the tip, the high electric field and the low vapor pressure of Gallium, the latter will be extracted from the Taylor cone as ions. These Ga+ ions are then accelerated towards the extractor electrodes and guided through the beam acceptance aperture. The condenser lens system will align the particle beam parallel and in the center of the main optical axis, also adjusting the energy of the ions. For ions typically the acceleration voltage (0.5 kV – 30 kV for the Tomahawk FIB column) instead of their energy is denoted. After the particle beam has passed the condenser lens system, the beam defining aperture determines the working beam current. This is done by choosing one from several apertures, each with a certain size, while the extraction current at the LMIS is constant at all times. The beam defining aperture allows the operator to choose a distinct beam current in the range from 0.1 pA to 65 nA. The following part of the ion column is the beam blanker, which can blank the beam within sub microseconds. After the beam blanker the ions are guided through octopole coils which make it possible to change the direction of the beam in X and Y direction, and are used to compensate axial astigmatism. Finally the objective lens focuses the ion beam on the sample. In order to achieve a long mean free path for the particles the ion column is operated under high vacuum conditions.

Besides the Ga LMIS several other ion sources and types are available [2,16,17]. However Ga is the most common ion source for a FIB for several practical reasons, which are its low melting point, its low vapor pressure and its immiscibility with the tungsten tip. More detailed information of the FIB can be found in literature [2,15].

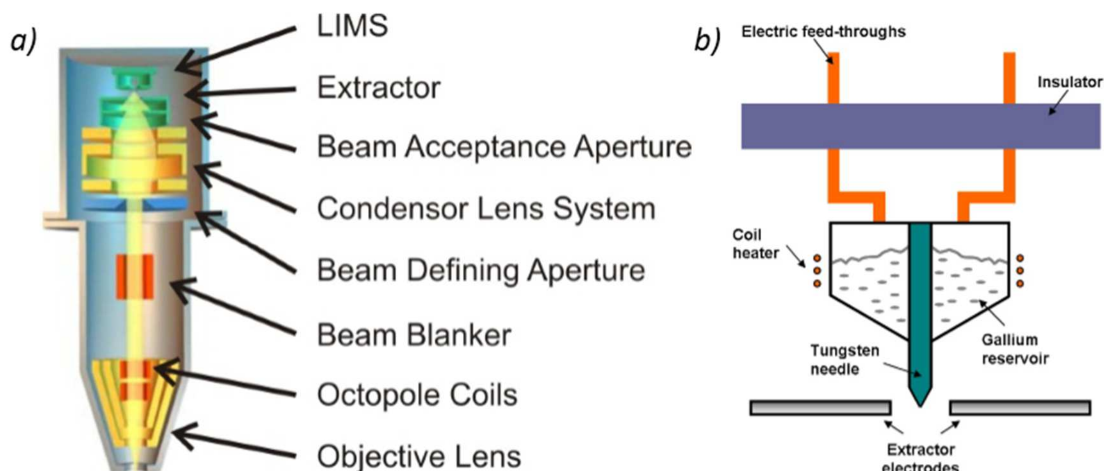

Figure 13: schematic diagram of the FIB column (a) a Ga LMIS (b) [12].

2.1.9 Ion beam – Matter Interaction and Detection

Just like electrons, Ga^{+} Ions will interact with bulk atoms or molecules either elastically or inelastically, resulting in an interaction volume below the sample surface, comparable to the case of electrons. However, one should consider that the penetration depth of the ions is far smaller than for electrons at the same energy. Simulations, depicted in Figure 14 (a) and (b), show the penetration depth of electrons and Ga^{+} ions, respectively, both accelerated by a voltage of 30 kV. The penetration depth of the electrons is up to 6 µm, while Ga^{+} ions would penetrate into the bulk up to 60 nm. This huge difference is due to a higher interaction cross section of the ions with the bulk atoms, because of their larger size and bigger mass, though this parameter is as well material dependent.

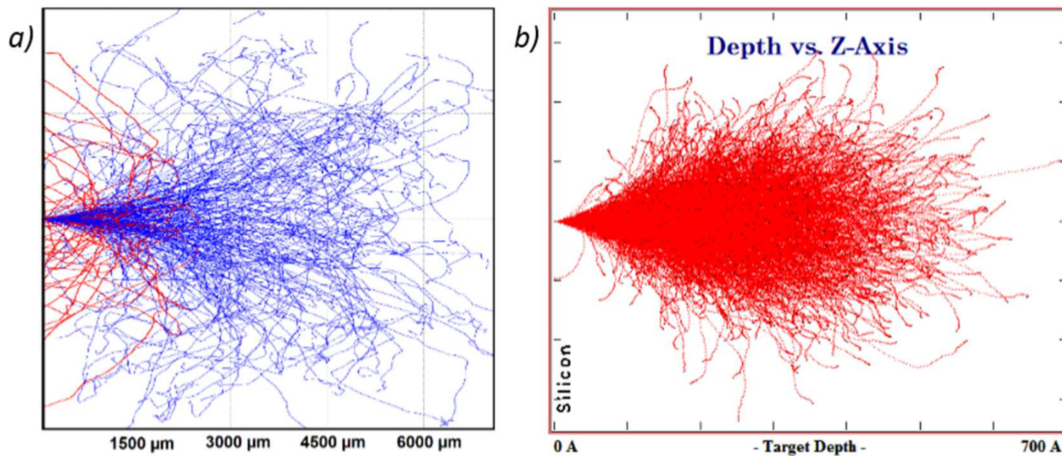

Figure 14: comparing the penetration depth in Silicon of electrons (a) and ions (b) with the same acceleration voltage (30 kV). One should notice the difference of the scale, showing a penetration depth of roughly 6 µm and 60 nm for electrons and ions, respectively. Simulations were performed with CASINO [14] and SRIM [18].

Undisturbed penetration of the ions will only happen in the range of a few Å, then collisions with bulk atoms and their electrons will occur, leading to a spreading of the beam, as can be seen in Figure 14 (b). The energy and direction of the ions changes, similar to the case of the electrons discussed before. The direct effects and follow-up processes of the ion beam interaction with the sample are pictured in Figure 15. A direct effect of the collisions is sputtering, at which the momentum transfer to the target atom enables it to leave the bulk. If the escaping atom is also ionized, one speaks of secondary ions (**SI**). After several collisions a Ga^{+} ion will either leave the bulk as a back scattered ion (**BSI**) or it will stay in the bulk and is permanently implanted. Therefore, ion implantation is unavoidable and leads to amorphization (for crystalline material) and/or chemical degradation (for molecules). Also SE are generated by collisions of the ions with weakly bound valence electrons and can be used for imaging, comparable to the case of the electron-specimen interaction. As the primary ion removes atoms, ions or clusters from their original bulk position through momentum transfer they start a collision cascade, as these particles again can cause the same processes as the primary ion. When such a collision cascade ends at the surface, the atoms may leave the sample if they have an energy higher than the surface binding energy, otherwise they will remain where they are and be in an excited state, these atoms are referred to as excited surface atoms (**ESA**).

Detection of SE and SI is done by an ion conversion and electron (**ICE**) detector, which works in a similar way as the ETD. Sputter rates and the generation of SE are dependent on the material and, if a crystalline material is investigated, on the orientation of the crystal structure, which can lead to ion channeling. Another considerable effect during sputtering is redeposition, at which already sputtered material is adsorbed to the surface around the sputtering region or even within the sputtered area. This effect becomes more significant for high aspect ratios. One can find more detailed information on ion beam-matter interaction, channeling and redeposition in literature [2,15].

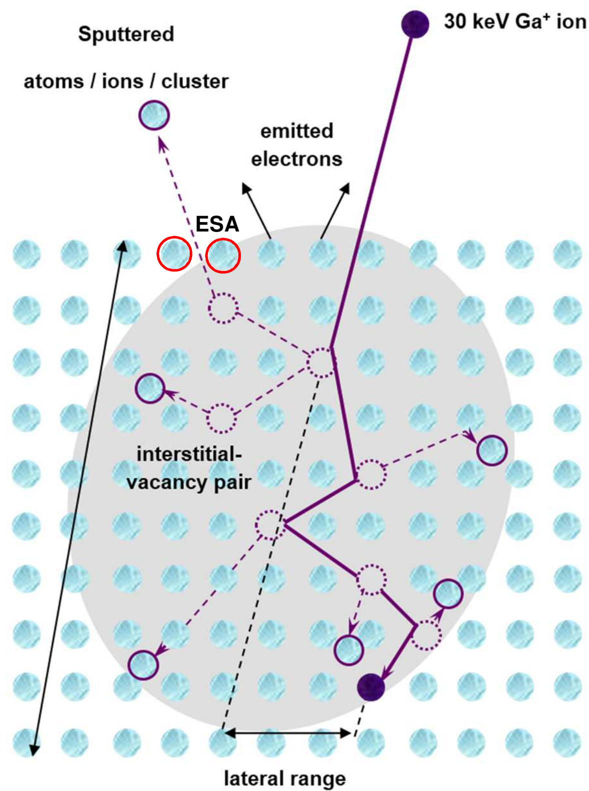

Figure 15: scheme of the ion interaction with the sample and follow-up processes. [19]

2.1.10 Patterning

Regardless of whether the surface is imaged, material is sputtered or a certain structure is deposited, for all applications the particle beam scans the surface in a certain way. For this purpose a pattern of points with a certain distance to each other is imposed on the surface, which are then successively scanned. There are two classic ways the beam can scan these points. One way is to scan line by line always from one side to the other, which is referred to as raster scan. Another possibility is to scan the points in a serpentine strategy. Therefore, the first line is scanned in one direction, the next line is scanned in the opposite direction, and so on, as depicted in Figure 16. The axis of consecutive scanning is referred to as the fast scan axis, the other axis is referred to as slow scan axis. Besides the two classical patterning strategies, recently other approaches have proven to be useful for certain applications. [20,21]

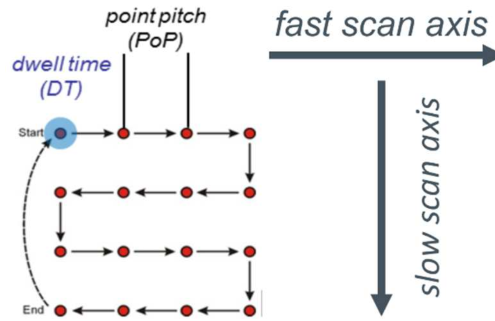

Figure 16: red points represent the patterning points, the arrows show the sequence, which is serpentine scanning strategy, the dwell time (DT) and point pitch (PoP) are depicted in the picture as well. Also showing the fast and slow scan axis, for the respective pattern.

The major parameters of patterning are the point pitch (**PoP**) and the dwell time (**DT**) which describes the distance between two consecutive points and the pulse duration per pixel, respectively. Relating the PoP to the beam diameter (**d_B**) gives the beam overlap (**OL**), which allows the usage of the same value for several beam currents. Further parameters are the number of passes (loops), which is the amount of how many times the same pattern of points is scanned. The refresh time (**RT**) is the time between two irradiation events at the same point, which is at least equal the number of points times the DT at each point, hence a relation between RT and DT exists. The total exposure time (**TET**) is the required time for the whole process which is equal to the RT times the number of loops. Furthermore, the beam can be purposely focused above or below the sample surface. The defocus (**DF**) of the beam also changes the intensity distribution and increases the beam diameter, and therefore also changes the PoP for a fixed OL.

Beam parameters and patterning parameters can be combined into one expression, thus the use of different parameters can be compared. Considering the whole patterned area the total ion dose (**D_{tot}**) can be defined (equation 2), including the pattern size, beam current, DT, OL and number of loops. If only one pulse is considered the point dose (**D_{pt}**) can be defined (equation 3). The mathematical expression for both of them is given below.

$$D_{tot} = \frac{DT \cdot I \cdot n}{(1-OL)^2 \cdot d_B^2} \quad (2)$$

$$D_{pt} = \frac{DT \cdot I}{d_B^2} \quad (3)$$

D_{tot} ... total dose
D_{pt} ... point dose
DT ... dwell time
I ... beam current
n ... number of loops
OL ... overlap
d_B ... beam diameter

2.1.11 Particle Assisted Deposition

2.1.11.1 Basics

Material deposition was first observed in SEMs as an unwanted carbon contamination on irradiated surfaces, at which these layers originated from the contamination gas in the sample chamber. Soon after this observation further investigations with several precursor gases were done, and since then

some of these precursor molecules with different physical behavior (e.g. conductive, insulating, magnetic) have been investigated [2]. In general there are several, sometimes conflicting demands, for the precursor molecule. First of all a molecule has to be found, which includes the material of interest leading to the intended functionality. The molecule itself consists of a non-volatile part, which includes this special material, and a volatile part, giving the further discussed properties. Ideally the precursor material has a low sublimation temperature and high vapor pressure, it should be easy storable and not decompose over time periods of several months. Furthermore a high sticking coefficient and a long residence time is favorable, while the volatile part of the molecule should desorb as fast as possible, to avoid undesired contamination of the deposit. It is however, only possible to meet all these demands up to a certain degree and sometimes trade-offs have to be met. For further and in depth information on this topic see [2].

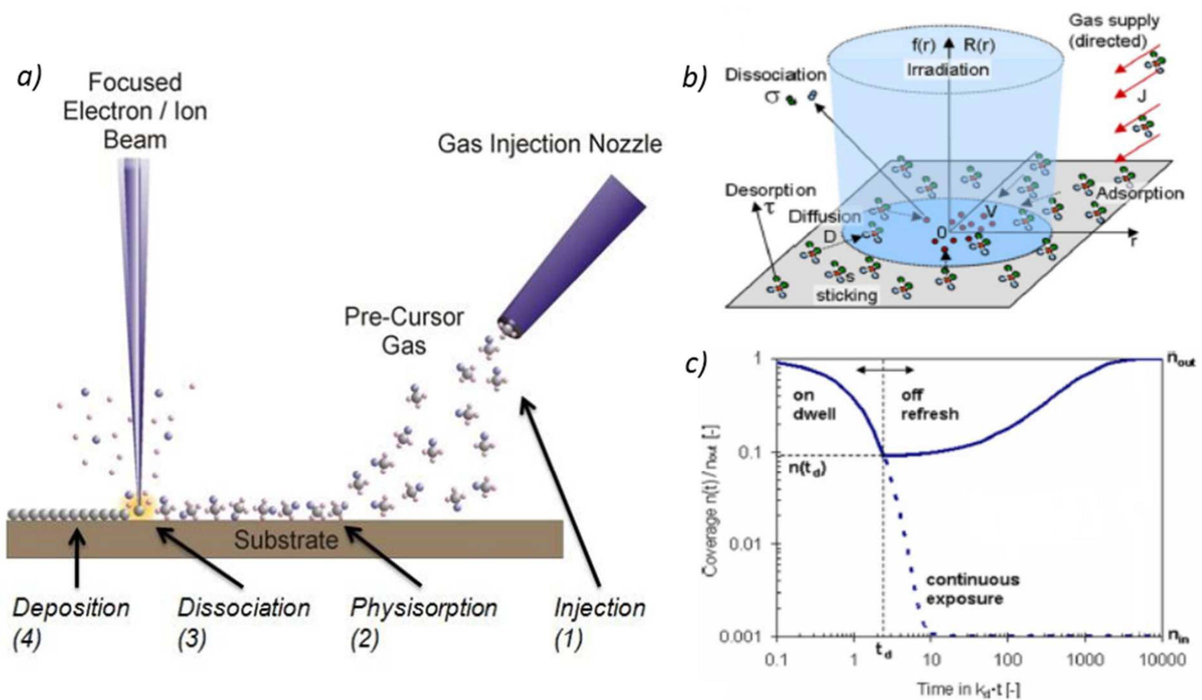

Figure 17: a) from injection of a precursor to deposition; b) deposition on a small scale c) coverage of the precursor molecule at the area of irradiation: depletion of the precursor coverage during irradiation (on dwell) and replenishment (refresh). [2]

The process of deposition itself is just as complex as the demands on the precursor molecule and consists of several steps, which are shown in Figure 17 (a). First the gas injection nozzle (**GIS**) directs the precursor gas to the sample (1), which will physisorb (2) with a certain probability, described by the sticking coefficient. As long as the precursor is adsorbed it randomly diffuses on the surface. Time of adsorption and behavior of the precursor are described by two parameters: the mean diffusion path and the mean residence time. The mean diffusion path is the net distance the molecule will travel on the surface. The residence time is the mean time the molecule will stay on the surface before it desorbs. The exact values of the above mentioned parameters are very complicated to access as it further depends on several factors, e.g. surface temperature, substrate, surface orientation of the substrate, precursor pressure, precursor kinetic energy. However, as will be discussed later, it is sufficient to understand individual tendencies instead of having the exact numbers in order to optimize

the process itself. The next step during deposition (3) is the dissociation of the precursor molecule. According to [2] there are several processes leading to the dissociation of the precursor on the surface, depending on the type of particle beam. In case of a FEB PE, SE and BSE will predominantly dissociate and immobilize the precursor molecules. In case of a FIB, the secondary electrons and excited surface atoms are regarded as the dissociating particles, which as well limit the resolution of the deposits. The predominant process depends strongly on substrate and precursor. However, in reality the molecules will not fully dissociate, which means that some of the bonds might not break up. In addition to that, some volatile groups might not desorb fast enough, which can lead to a high unwanted incorporation of these parts leading to carbon contents as high as 90 at.% depending on the entire process itself [2].

Looking at the deposition process from a more global point of view it is possible to identify 3 different working regimes, which depend mostly on the relation between RT, DT and beam current.

Considering only one single point, the precursor is depleted during the beam pulse related DT leading to reduced coverage as depicted by the left branch in Figure 17 (c). However, even during irradiation fresh molecules are brought to the area by surface diffusion and direct gas flux replenishment which explains the non-zero growth rate for even long DTs. After the pulse, or in other words in between consecutive beam pulses defined by the RT, the local area is replenished with fresh precursor molecules. Hence, the coverage rises towards saturation as shown by the right branch in Figure 17 (c). As the RT can vary depending on the pattern size, DTs and PoPs, the replenishment can be completed or still be reduced which then changes the growth during the next beam pulse. In principle one can distinguish between two extremes: 1) particle limited regime in which the number of available molecules always exceed potentially dissociating particles and 2) the molecule limited regime defined by a strong excess of dissociating particles. Intermediary is the diffusion-enhanced regime, where particles and molecules keep in balance, and the replenishment is mostly due to surface diffusion. The final volume growth rate (**VGR**) strongly depends on the deposition regime in close correlation with the final functionalities as different regimes induces different degrees of dissociation and by that a varying chemistry [2,22,23].

While working with the ion beam, two further points should be considered for the deposition process, which is material removal due to sputtering and beam induced charging for non-conductive samples. During irradiation the surface is exposed to high stress due to these two factors. Material removal exceeds the deposition process when too less precursor molecules are available. This is a major difference between ion and electron beam induced deposition, at which no material removal due to the electron beam occurs. Sputtering is always present to some extent during deposition and it becomes then predominant if there are simply too few precursor molecules to be deposited. Thus with increasing beam current, which means more dissociation particles, a higher sputter rate can be achieved [2]. For beam induced charging not much information in the literature can be found. However, as a rule of thumb the point dose should be kept below a certain value, in order to avoid charging induced damage. Both these factors implicate that certain beam currents should be only applied above a certain threshold value of processed area, in order to avoid a too high point dose.

The Platinum precursor used for this thesis is Trimethyl-Methyl-Cyclopentadien-Platinum with the chemical formula $(CH_3)_3$ Pt $CpCH_3$, depicted in Figure 18 (a). In the center is a Pt atom, bonded to three Methyl groups and a Cyclopentadien ring, also having different binding energies. A study has shown that the interaction of the particle beam with the bulk and the follow up processes lead primarily to a

breaking of the Pt-Me bonds, while the cyclopentadien-ring is almost not dissociating, hence a high amount of carbon is incorporated, which is the major drawback of this precursor molecule [24]. Otherwise it shows a relatively high diffusion rate and a long residence time, which is favorable. But the incorporation of Carbon can actually be up to 90 at%. Due to the high C incorporation this precursor gas shows a high VGR, while having a high resistivity compared to bulk Pt (10.6 μΩ cm), a comparison of reported values is given in [5], which lie in the range between 10^2 and 10^8 μΩ cm. Due to its high VGR Pt is widely used as a protecting layer during lamella preparation for TEM. Recent studies, however have shown the potential application of Pt C deposits as special sensors [25,26].

The Tungsten precursor for this study was Tungsten-Hexacarbonyl ($W(CO)_6$), depicted in Figure 18 (b) consisting of a W atom surrounded by 6 carbonyl groups . It is assumed that the residence time and diffusion length are smaller compared to other precursors, hence the working regime will be mainly governed by direct gas flux replenishment. Also for this precursor type full dissociation of all bonds is very unlikely, thus carbon and oxygen incorporation was reported of about 30 at% and 15 at%, respectively. Compared to the Pt precursor the VGR is about an order of magnitude lower, the resistivity is in the range between 100 and 300 μΩ cm [2], compared to 5.6 μΩ cm for bulk W. This precursor is widely used in CE for deposition of high aspect ratio vias and connections.

In conclusion one can state that the Pt precursor gives faster deposition at lower electric conductivities and vice versa as studied in detail in this thesis.

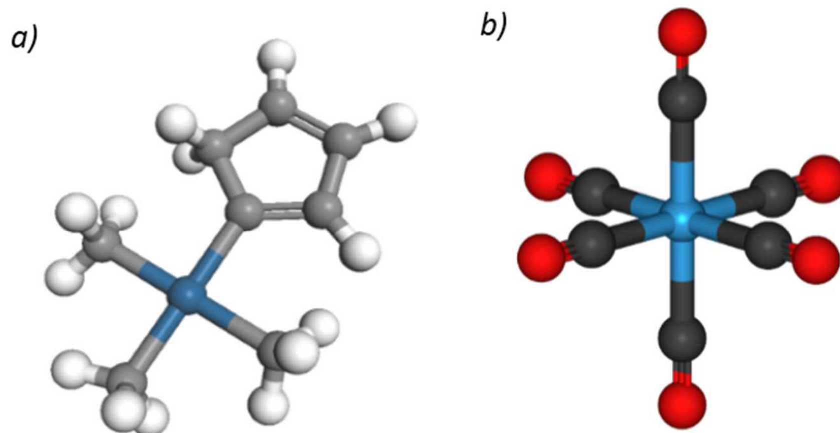

Figure 18: a) the precursor ($(CH_3)_3$ Pt $CpCH_3$) used for deposition of Pt. The Pt atom is colored blue, the C atoms are colored gray, the H atoms colored white. b) the chemical structure of the precursor ($W(CO)_6$) used for deposition of W. The W atom is blue, C atoms are black and O atoms are red.

2.1.11.2 Etching

Besides deposition, also gas assisted etching is possible, with the same basic principle as discussed above. Within the precursor molecule a reactive element is brought to the surface, where it can, once dissociated, react with the surface atoms, thus resulting in a molecule consisting of the surface atom and the reactive element. Subsequently, this molecule will desorb and in total enhancing the material removal rate. Furthermore, this process is independent of the crystal structure, hence channeling effects are negligible. Typical precursor molecules for gas assisted etching include XeF_2 for silicon based materials, I_2 for most metals and H_2O for carbon. Recent investigation at FELMI even have shown that

with a post deposition treatment using H_2O assisted etching, Pt deposits can be fully purified and even achieve a pore-free structure [27].

2.1.12 Electrical Transport

As mentioned above, the deposits have a high amount of carbon incorporated, if not further treated. The microstructure of a deposit normally consists of metal clusters embedded in a carbon matrix. Whereupon the size and distribution of these clusters depend strongly on the process parameters as shown later in this thesis. Conduction in such deposits with high C content and low resistivity is best described by the model of variable range hopping [26,28,29]. In this model electrons and holes move by tunneling processes through localized states, thus such materials reveal a positive temperature coefficient, as the tunneling probability increases with temperature. For deposits with low carbon content, thus high conductivity, the conduction mechanism becomes more metal like. It is possible for some cases to increase the conductivity by post treatment curing, at which the electron scans the deposit and subsequently dissociates further Pt-C bonds, which leads to a growth of Pt clusters in the material [30]. Another effect, which has shown to increase the conductivity is current induced post treatment heating, which can as in the case shown for W nanowires lead to the segregation of W and Ga and subsequently to the crystallization of W, thus achieving a resistivity as low as 50 μΩcm [31].

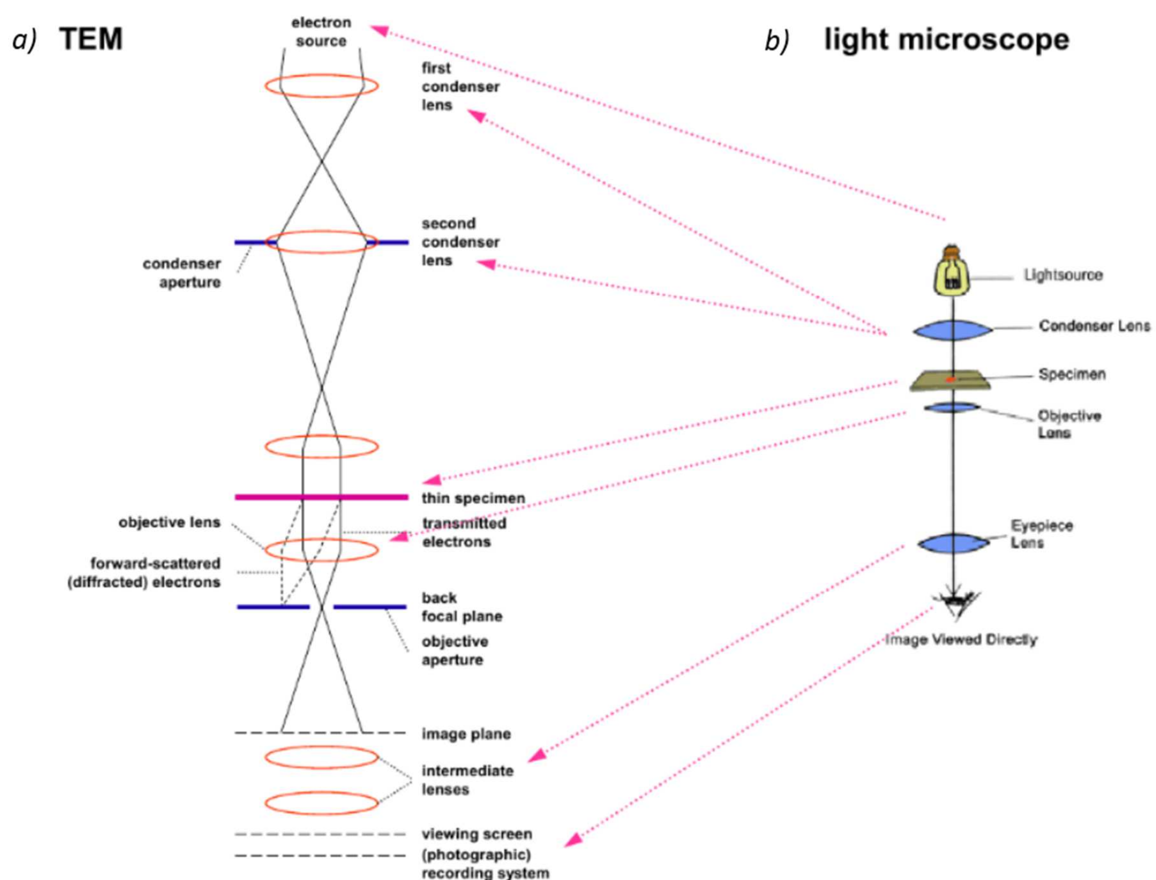

Figure 19: schematic diagram and mode of operation of a TEM (a) in comparison with a transmission light microscope (b). [32]

2.2 Transmission Electron Microscopy

As mentioned above, the resolution of a SEM is amongst other things limited by the interaction volume with the sample. This problem is bypassed in a transmission electron microscope (**TEM**), where the sample is so thin, that the primary beam is almost not broadened as it interacts only once in ideal cases. For this purpose the sample should be thinner than the mean free path of the electron, which is in the range of about 100 nm for most materials. Compared to a SEM the components of a TEM are the same, just differently arranged, as the detection of electrons is after their interaction with the sample, comparable to an optical transmission microscope, as shown in Figure 19. The electron beam is generated at the top, by the same source as for a SEM, then guided through a condenser lens system, which focuses the beam onto the sample. The electron beam is either confined to a single spot and rastered, comparable to a SEM, which is referred to as scanning TEM (**STEM**), or a larger area of the sample is simultaneously irradiated by the electron beam, which in this case is comparable to a plane wave. After the electrons pass the sample the beam is magnified by a further lens system, which consists of the objective lens and intermediate lenses. At the bottom of the column the final image is either observed on a fluorescence screen, recorded with a CCD or guided into an energy spectrometer. In order to obtain a long mean free path and to achieve a high resolution, the electrons are accelerated to energies, typically between 100 keV – 300 keV, additionally the microscope is kept under UHV for the same reason as the SEM.

Contrary to the SEM the primary electrons are detected after passing the sample, where they interact with the bulk atoms either elastically or inelastically. The same interaction mechanisms as previously discussed in section 2.1.6 take place. Rutherford scattered electrons can be used for imaging of the sample and depiction of material and thickness contrast. On the other hand electrons scattered by diffraction can be used to determine the crystal structure and crystal orientation, by applying Bragg's law. Inelastic scattered electrons can be used for analytical information of the sample. For this purpose electrons are deflected in a magnetic prism at the bottom of the TEM column, according to their energy loss. By looking at the energy loss of the electrons one can reconstruct the ionization processes, which must have taken place, thus making it possible to obtain chemical information. This method is referred to as electron energy loss spectroscopy (**EELS**). Benefits of this method are their high lateral resolution, thus making it even possible to distinguish between chemical bonds. Furthermore no problems arise for detection of low elements, compared to the case in EDX, although for EELS the analysis of higher elements can be precarious. Therefore, these techniques are mostly used complementary to each other or even simultaneously. Using a special lens system after the magnetic prism makes it possible to reconstruct the image. By using a further energy filter it is possible to use the information of EELS for imaging, this method is called energy filtering transmission electron microscopy (**EFTEM**). Additionally it should be stated that due to the low interaction volume and flat morphology of TEM samples and the higher energy of the electrons, the interpretation of such spectra is generally less prone to errors than for SEM. For those reasons this techniques were used for full quantification of the structure and composition. For further and more in-depth information about the TEM one can find many fine introductory books such as [33].

2.3 Prober Shuttle

2.3.1 Technical Setup

To perform electrical measurements within the DBM a Kleindiek Prober Shuttle (PS4) is used, equipped with 4 movable probers, which can be moved in X,Y and Z direction with a sub nm resolution [34]. The used prober shuttle is depicted in Figure 20 (a), as it was mounted on the DBM stage. The prober needles consist of a tungsten shank with a tungsten tip, which was bent 20° downwards in order to contact the sample surface. Shuttle and prober are connected to a control unit and source meter (Keithley 2612B), outside the microscope, also depicted in Figure 20. With the used setup current sourcing/measuring in the range of 100 fA to 1.5 A and sourcing/measuring voltage in the range from 100 nV to 200 V was possible. The source meter can be connected to a computer and controlled via a software, which makes it possible to apply special current voltage sweeps. A special stub was manufactured to elevate the sample above the shuttle, enabling full use in the eucentric height. Thus the stage could also be tilted to work with the FIB while the prober shuttle was mounted.

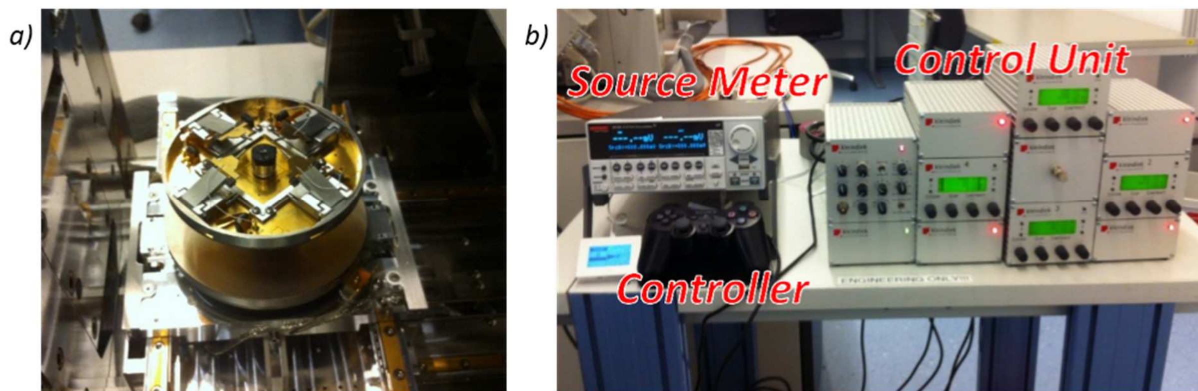

Figure 20: the Kleindiek Prober Shuttle (PS4) mounted on the DBM stage (a) and the control unit & controller plus source meter and controller (b).

2.3.2 4 Point Measurement Principle

The classical measurement setup to determine the resistance of a wire, as shown in Figure 21 (a) has a major flaw, that is to say the resistance of the prober and the contact resistance are measured as well, indicated as the red path in the same figure. Especially for small dimensions (µm region) the contact resistance of the prober to the wire is hardly reproducible for several measurements. One way to work around this problem is to use a 4 point measurement setup, illustrated in Figure 21 (b). A variable voltage source on the outer two probes is adjusted in such a way that the current which flows through the wire is set to a constant value, therefore one also speaks of current sourcing. If the contact resistance changes, the voltage is readjusting in such a way that the current remains the same. The potential difference is measured with a voltmeter between the inner two probes. Since the input resistance of an ideal voltmeter is extremely high, the contact resistance is negligible to the inner resistance in the voltmeter. With this method, one can choose a certain current on the outer probes, measure the potential difference between the inner two probes and calculate the resistance. The resistivity can be determined by taking into account the length and cross section of the measured path.

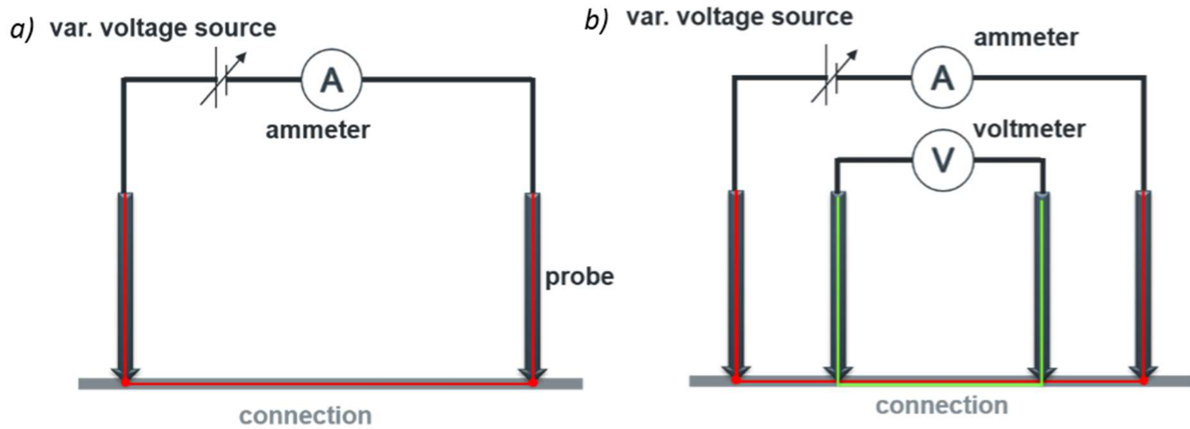

Figure 21: a) 2 point measurement setup (Ohmmeter), the resistance is measured along the red path; b) 4 point measurement setup, the resistance is measured only at the overlap between red and green path.

2.4 Previous Works

This section serves as a short overview and summary about several studies that have been carried out before, in order to give a starting point for this work. Although this thesis will focus on FIB assisted deposition (**FIBAD**) of electrical conductive materials, some aspects (i.e. side effects) from FEB induced deposition (**FEBID**) also have to be taken into account, as they give fundamental restrictions on the depositions process.

2.4.1 Side Effects

Investigations by Winkler et al. [23,35,36], have shown, that for FEBID the distance of the GIS with respect to the sample surface and the alignment of the main axis of the nozzle in respect to the beam center can have a significant influence on the morphology and the composition, mostly due to the inhomogeneous gas flux. These circumstances can substantially affect the functionality of the deposits, therefore must be considered in this work, as one of the major aims is to achieve a high reproducibility of the deposition process.

2.4.2 Deposition Process

In general, a higher acceleration voltage of the ions will give rise to the interaction volume, as shown by simulations for 5 kV and 30 kV, depicted in Figure 22 (a) and (b), respectively [18]. Along with that, a higher beam energy will theoretically result in a higher yield of ESA and SE, which would in general increase the deposition rate [2]. However studies [37,38] showed that varying the acceleration voltage of the ion beam between 5 kV and 30 kV will not change the overall deposition rate. Furthermore the energy spectrum of ESA seems to be mostly independent of the primary ion beam energy, as has been stated in [2], according to SRIM simulations. Thus one might assume that the same type of dissociation will take place during the deposition process, regardless of the primary ion beam energy. As it seems to be, that this parameter will neither change the deposition yield considerably, nor change the chemistry of the deposits, it was set to a constant value of 30 kV in the investigations. This value was chosen such, since with higher energy the beam diameter becomes more narrow, thus allowing to

work more precisely. Furthermore, from a practical point of view, all other procedures (i.e. sputtering, etching, deposition of coating layers) with FIB are undertaken with this particular acceleration voltage, hence the operator doesn't need to think about changing this value during processing.

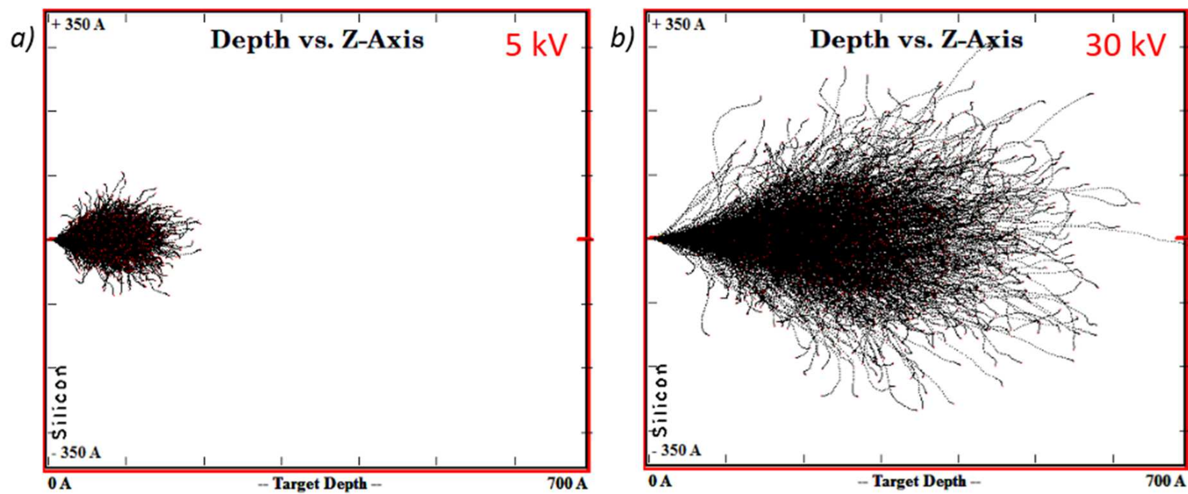

Figure 22: comparison of two ion stopping range simulations using SRIM for ions with an acceleration voltage of 5 kV (a) and 30 kV (b). [18]

Considering the influence of the ion dose (see equations 2 and 3) on the chemical composition, resistivity and VGR, there seems to be more contradictory information in the relevant literature. One of the first studies carried out on this topic [39] concluded that, in general Pt precursors yield a lower ratio of resistivity to VGR than W precursors, thus they assumed Pt precursor would have a higher efficiency than W. Furthermore, this study shows that for optimal outcome a certain relation between DT, OL and beam current density exists. In other studies it was reported that varying the DT will not change either the VGR or the resistivity [37]. Another recent work has implied that for FIB assisted deposits the resistivity is mostly determined by Ga incorporation [40]. This study investigated Pt and W deposits and even suggested, that the final resistivity is rather dependent on the amount of Ga and Metal as on the type of precursor used.

Other recent studies focused on the fabrication and characterization of nanowires deposited by FIB or FEB. One of these studies also bring into account a dependence of the resistivity on the height for deposited nanowires [5]. In particular an insulator to metal transition takes place as the wire grows within the first 50 nm. According to the author the composition changes during the growth, which might have two root causes, which are the changing SE yield (going from substrate to deposit) and the changing heat flow conditions (going from 3D to quasi 2D). In general, results of different studies seem to contradict each other, which can be regarded to the dimension, different experimental conditions (e.g. GIS alignment, substrate) and also to the different patterning parameters of the deposits investigated and simply by the fact, that no two DBM are completely alike.

Based on these partly very different result this thesis was initiated to understand FIBAD processes from a more general point of view. As will be shown later, most of the inconsistencies can be attributed to the precursor working regime which was mostly neglected in previous works!

3 Experiments and Results

As already mentioned in the introduction this thesis was done in cooperation with ams AG [7], a manufacturer of high performance analog semiconductors. Therefore, it aims on the practical aspects of focused ion beam assisted deposition of conductive materials in the field of device modification and rapid prototyping. In particular, the objectives of this work are depictured in Figure 23. In the first part of this work (section 3.1), side effects, induced by the pattern arrangement, the deposit geometry and the arrangement of the deposit relative to the GIS are investigated. This section is followed by the main part of this work (section 3.2), finding the optimal parameter set for most efficient deposition, i.e. to unravel the relation between parameters and functionality. Additionally the predictability and reproducibility are considered within this section. Finally the results are summarized in chapter 3.3, where an easy-to-use guideline for practical applications in CE is derived. Furthermore, a short investigation (section 3.4) about the possibility of current induced functionality tuning for the connections is provided. Before showing the experiments and their results, a few requirements for the deposits are discussed.

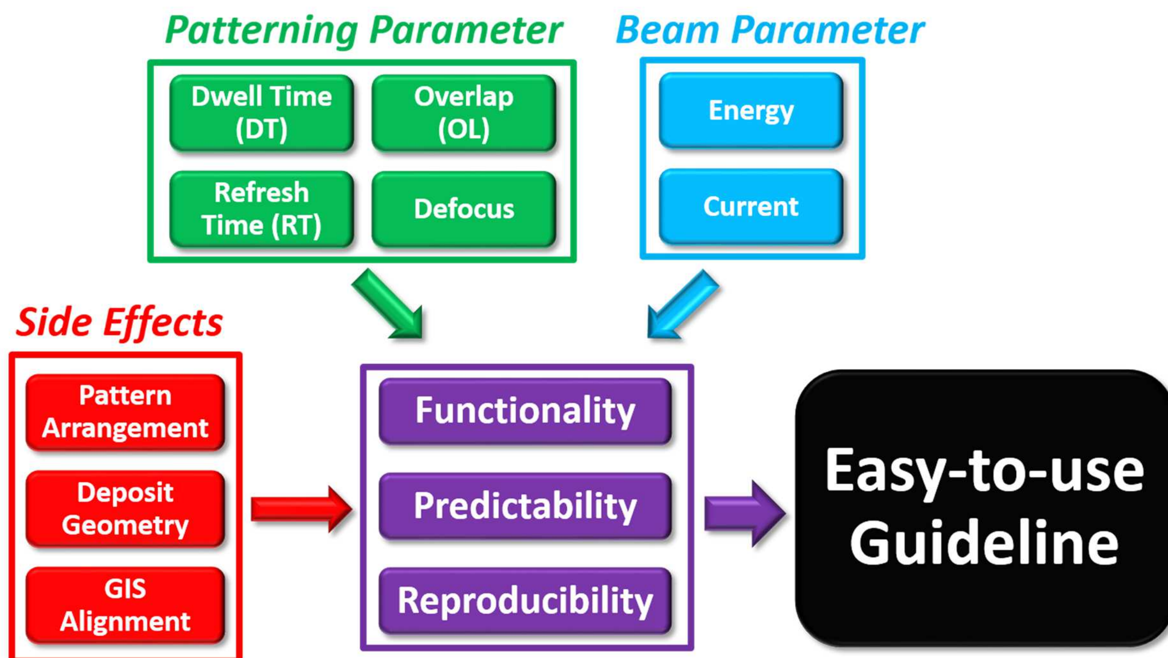

Figure 23: representation of the objectives of this thesis: identification of side effects (red) relating them to the functionality (purple), which is optimized with respect to the parameters (patterning: green, beam: blue) of the deposition process, to enable predictability, to ensure a high reproducibility and finally a summary is given in the form of an easy-to-use guideline.

The connections deposited for CE typically have a length between 3 µm and 500 µm. Due to the high intrinsic resistivity of the deposits, a trade-off is met between total resistance on the one hand and deposition time on the other hand, which results in values for resistance per length between 1 and 10 $\Omega\ \mu m^{-1}$. Given by typical CE related applications at the ams AG, useful widths and heights of the connections are between 1 and 3 µm, thus, this study focuses on deposits with such dimensions. Furthermore, the cleaning procedure of the connections, due to overspray, afterwards ought to be as short as possible and in general the whole process of deposition should be as less damaging as possible.

3.1 Side Effects

3.1.1 Introduction

It is known from literature as well as from practical work that the pattern arrangement itself can have a huge influence on the morphology and the chemical composition of the deposit. Since most studies focused on pattern arrangement related effects on the nanoscale, a short investigation on some effects was done here regarding the scale of the objective dimension. In many cases the device to be modified also brings some restrictions for the deposition process. These can be manifold, e.g. already established contacts to the pads (Figure 24 (a)), which limit the movement of the GIS, resulting in shadowing along a particular direction (Figure 24 (b) and (c)) and others. As these side effects are sometimes non-avoidable, the operator should be aware of them, since the properties of a deposited connection might be considerably influenced, subsequently changing the functionality of a whole analog circuit. Therefore the aim of this section, is to investigate the correlation between VGR, morphology, chemical composition and the above mentioned root causes.

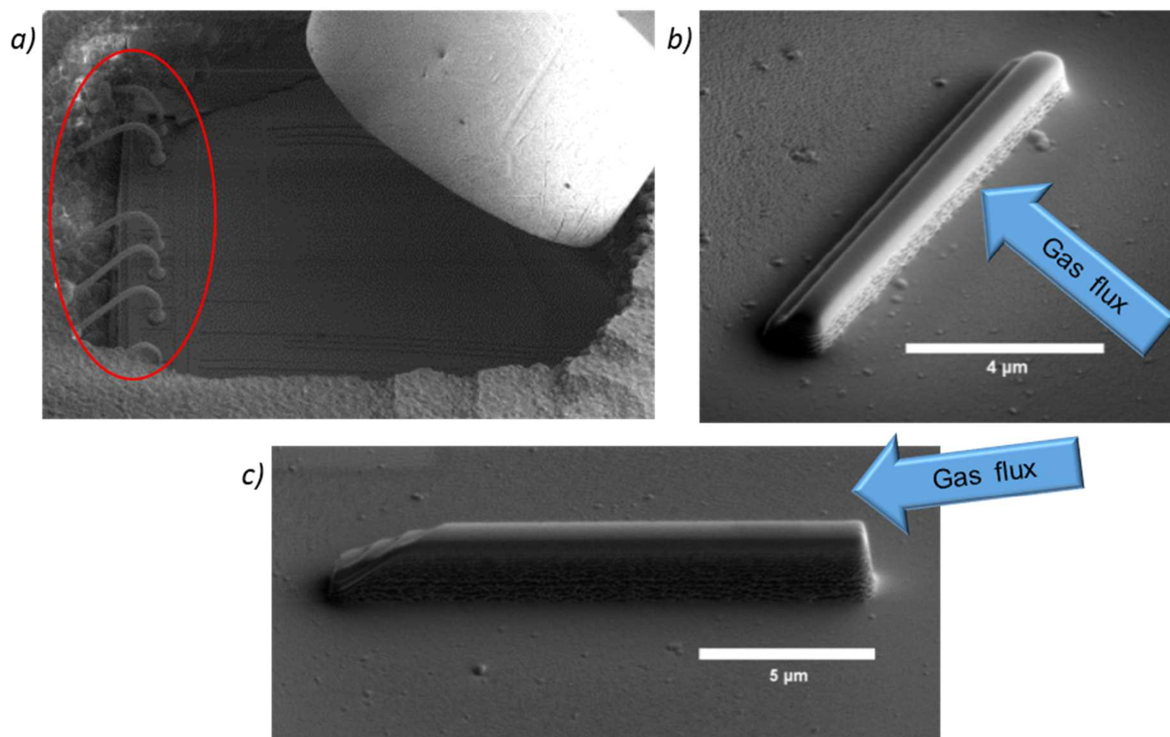

Figure 24: a) contacts (red circle) limit the movement of the GIS nozzle; b) and c) shadowing effects at a 15 µm long connection determined by the nozzle position relative to the pattern.

3.1.2 Specifications

Before the actual investigations started, the used DBM had to be specified, since some important information of the system were not known yet. These specifications mostly consider the alignment of the GIS nozzle for reasons mentioned in the section before.

3.1.2.1 Gas Injection Nozzle

To determine the height of the GIS nozzle above the sample surface in the eucentric height the following procedure is done: while the nozzle is inserted the z value of the stage is increased (i.e. the sample is brought closer to the nozzle) until the nozzle moves, due to physical contact with the sample surface. This procedure is undertaken for the Pt and W GIS nozzle, for 0° and 52° stage tilt, 10 times each. The results are listed in Table 1.

Table 1: distance of the GIS nozzle in eucentric height.

GIS	distance at 0° [µm]	distance at 52° [µm]
Pt	60 ± 1	85 ± 2
W	-232 ± 3	157 ± 3

To determine the position of the beam center with respect to the main axis of the nozzle, an image using the SEM and no tilt as well for the FIB, while tilted, with the lowest possible magnification is taken, while the GIS nozzle is inserted. An example for SEM is shown with inserted Pt nozzle in Figure 25. The main axis of the nozzle is marked as the blue dot dashed line, while the center of the beam focus is marked with a red cross.

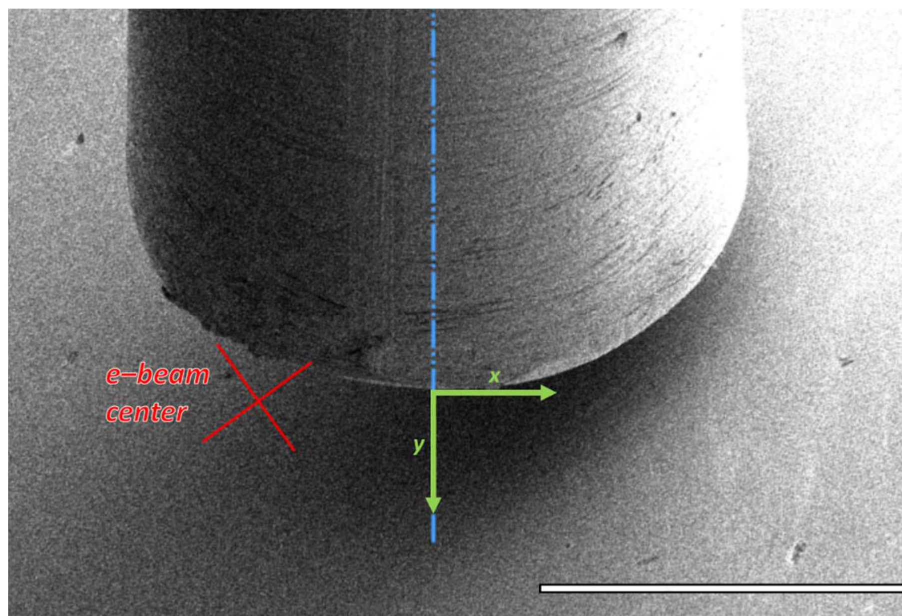

Figure 25: determining the lateral distance of the beam center (red cross) to the nozzle main axis (blue line), at which X and Y are defined by the green coordinate system centered at the apex of the GIS nozzle. In this particular case the Pt GIS nozzle was investigated with the SEM, the white bar represents 500 µm.

The results for the electron beam and ion beam are given in Table 2. For the W GIS nozzle the main axis is well aligned with the beam center. While for the Pt GIS nozzle the beam center is significantly off the main gas axis.

Table 2: The lateral distances of the beam centers relative to the GIS main axis (X) and relative to the apex of the nozzle (Y) in the eucentric height determined for operation with the SEM and the FIB. (*) as shown in Table 1 the nozzle of the W GIS is below the eucentric height, therefore no specification was undertaken in this case.

GIS	SEM X [µm]	SEM Y [µm]	FIB X [µm]	FIB Y [µm]
Pt	-245	17	-227	-10
W	*	*	-50	30

3.1.2.2 Stage Drift

As mentioned in the introduction the used DBM has a QuickLoader installed. Although this practical attachment increases the sample throughput and keeps the working vacuum quite stable, it has some disadvantages. The sample is attached to the sample holder by a mechanical system, therefore, a high and rather long-lasting stage drift after tilting is the consequence. To quantify this drift, the beam was centered on a certain sample feature (e.g. a particle on the surface) and tilted from 0° to 52°. Subsequently, the feature was imaged at certain times after tilting, while measuring the distance between the beam center and the sample feature. An example for such a measurement is shown in Figure 26. The measured values were put into relation to the initial distance between beam center and sample feature right after tilting. This experiment was done after direct loading (series 1), and after the sample holder had been loaded before (series 2), 3 times each.

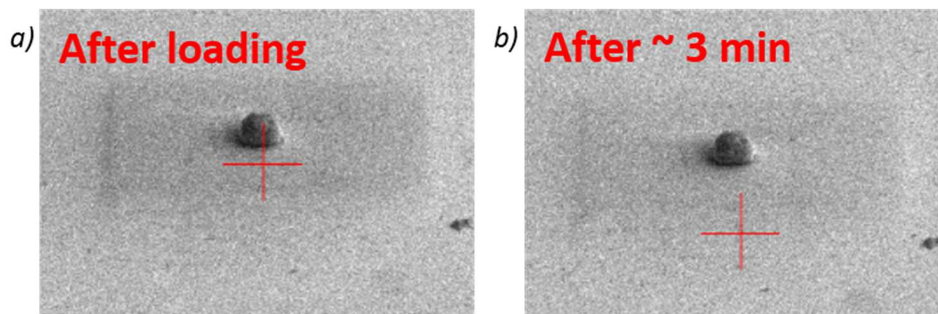

Figure 26: Example of the stage drift: after initial loading (a) the beam center is close to the sample feature, after about 3 min. (b) the sample has drifted considerably away.

The results are summarized in Figure 27 (a), showing the relative stage drift, which is the stage drift between two measurement points divided by the time span in between these measurements. The curve shows initially a very high drift, which settles after about 3 min for series 2 and after 7 min for series 1 to a value of about 1 nm/s. Hence this effect should be considered especially after initial loading of the sample holder. Furthermore, the measurements have also shown that stage drift mainly occurs in the same plane as the tilt angle of the stage, which is another evidence for mechanically induced drift, as it seems that the sample slowly slips down the sample holder. Due to this effect (and some other as discussed later) structures which are deposited with a high TET will show a slanted cross section, as representatively shown in Figure 27 (b).

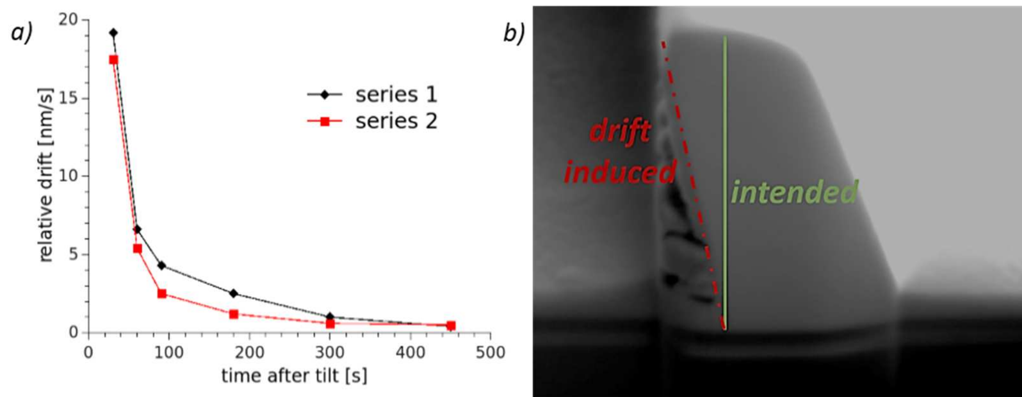

Figure 27: a) results for the determination of the stage drift. The black curve represents the measurement series at certain times after initial loading, the red curve shows the result for the second series. b) a structure deposited with a TET of about 25 min. showing a highly slanted cross section due to stage drift. For visualization of the effect the drift induced slant (red) of the structure is compared to the intended structure (green).

3.1.3 Investigations on the Volume Growth Rate (VGR)

The first investigations on the deposition process focused on the VGR at different amount of loops at currents of 40 pA, 80 pA and 230 pA. The aim of this investigation was to find out, how the deposition process changes during growth. The OL and DT were kept constant at -150 % and 200 ns, respectively. The beam diameter for currents of 40 pA, 80 pA, 230 pA and 430 pA are 16 nm, 21 nm, 38 nm and 52 nm respectively. The layout of this experiment is shown in Figure 28. Size of the deposits is 2 x 2 µm², arranged in a field of 4 x 4 pads, distance between neighboring pads was about 4 µm. The slow scan axis of the pads was aligned parallel to the nozzle main axis. Processing of the pads started with the row farthest away, in order to decrease shadowing effects. The number of loops was varied linearly, from 775000 loops (1) down to 100000 loops (16) in a serpentine manner. The variation of the loop number is equivalent to a variation of the TET. The height was measured using the SEM at a stage tilt of 52° at the edge of the pad. Each pad was deposited in such a way that the slow scan axis was pointing towards the GIS nozzle, as shown in Figure 28. EDX measurements were done with SEM 5 keV and 1.6 nA within a field of 200 nm x 200 nm in the middle of the pad. For all further EDX measurements these parameters were used.

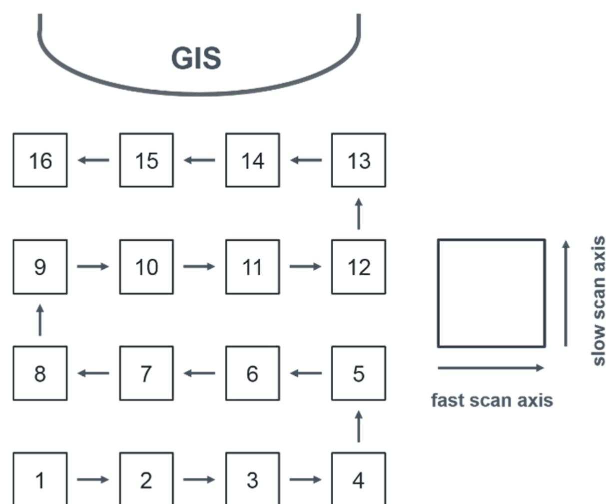

Figure 28: experimental layout for the determination of the growth behavior at different currents, also showing the general orientation for the slow and fast scan axis.

The result of the height measurements are shown in Figure 29. Just as one would expect the VGR increases with a higher beam current, indicated by a steeper slope of the height vs. TET (see legend). Furthermore, we see that for the 3 different beam currents the growth is widely linear, as the linear fits indicate. Going one step further and plotting the height vs. TET for the ion beam dose instead of the beam current, as done in Figure 30 shows that the VGR primarily depends on the ion beam dose, concluding that the working regime is constant for those 3 beam currents. Furthermore, all data points together were linearly fitted through zero, indicated as the green line, at which the slope gives the dose dependent volume growth rate: (440 ± 5) $x10^6$ μm^3C^{-1}. The general behavior can be easily explained by the fact, that the current is simply the value representing the number of particles impinging on the sample, hence more particle will lead to a higher amount of dissociation processes, induced by SE and ESA. Furthermore, it can be deduced that the growth regimes in all cases are precursor limited, since the ion curves are the same for the same ion doses. In addition to that it can be stated that the main replenishment mechanisms during irradiation is by the direct gas flux and on top surface diffusion, since the height of the deposits exceed the diffusion length.

Next, the chemical composition is determined via EDX measurements. As carbon is strongly involved, absolute quantification becomes tricky, further convoluted by simultaneous carbon contamination during EDX. Therefore, extracting relative ratios is much more suited for determining qualitative tendencies. For that, we calculate the peak areas for C, Pt, Ga and W and put them in relative ratios. The EDX results for the above described experiments are summarized in Figure 31 versus the deposit height. In general, one can see that with increasing heights the C/Pt ratio (a) decreases while Ga/Pt (b) increases. This behavior would indicate that relative to Pt, less C is incorporated, while the amount of Ga increases. However, as the Ga dose per loop and by that the total Ga in relation to the TET is kept constant this means that the Pt content is reduced which implies a regime change. While this has some implications on the functionalities as will be discussed later, there is another observation which is even more important. A close look at the chemical ratios reveal a position related variation, indicated by the green circles in the same figure. For better visualization the Ga/Pt ratios for 40 pA and 80 pA are shown as a contour plot in Figure 32 (a) and (b), respectively. The figure shows the ratio related to the position and sequence of the pad in the pattern (indicated by white numbers and arrows), thus position and / or sequence related effects become immediately visible, in particular the ratios seem to increase in two directions, i.e. with further distance from the GIS and from the left to the right of the experimental layout. However, one has to keep in mind that the number of loops was varied in this experiment, which can explain the increase of Ga/Pt in Y direction. But the strong variation in X direction cannot be explained by the variation of loops. Furthermore, the strongest ratio shift, regarding the deposition sequence seem to happen between the furthest row and the subsequent deposited row. Thus several different effects might play together at the same time and cause the overall strange behavior of the Ga/Pt curve. Therefore, a closer look has to be taken to unravel the observed tendencies, at which the number of loops and TET will be kept constant, to obtain fully comparable deposits.

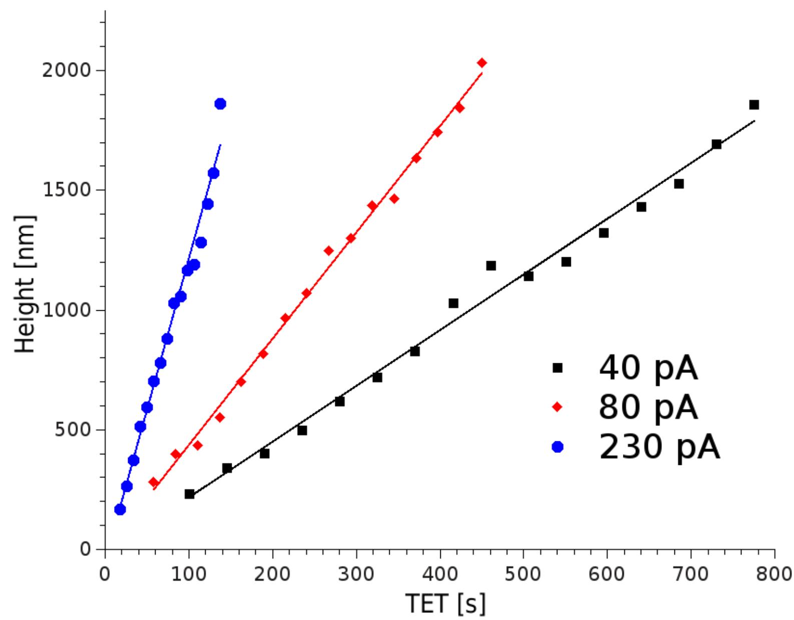

Figure 29: the dependence of the height on the TET for currents of 40 pA (black), 80 pA (red) and 230 pA (blue). For each series a linear fit was inserted to emphasize the linear dependence of the height on the total exposure time, within the considered working regime.

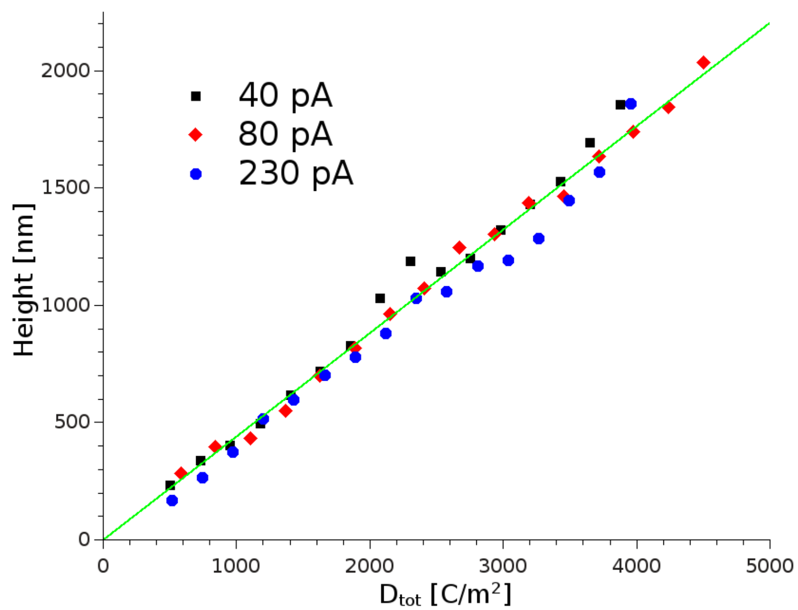

Figure 30: the dependence of the height on the total ion dose (D_{tot}) for beam currents of 40 pA (black), 80 pA (red) and 230 pA (blue). Additionally, the slope of a linear fit (green) for all data points gives the value for the dose dependent VGR.

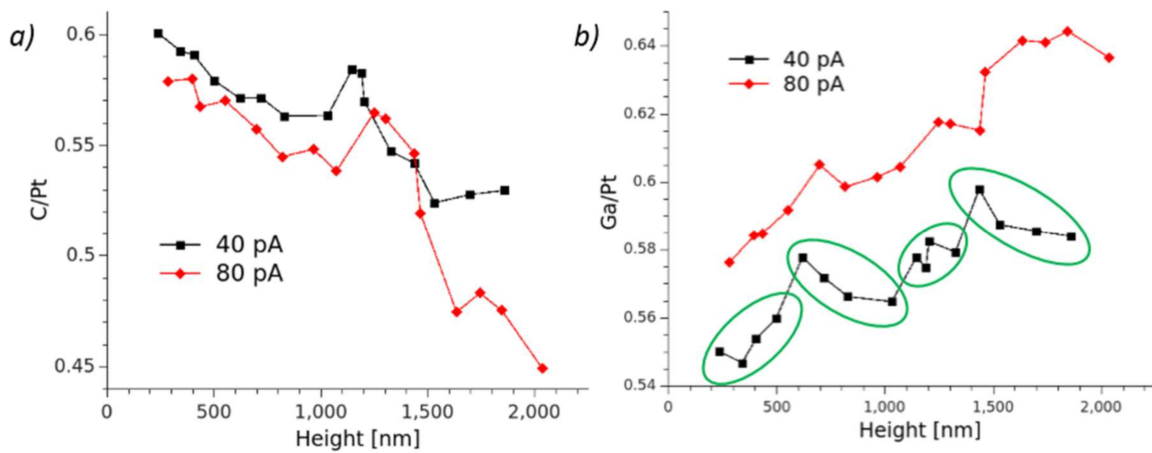

Figure 31: the ratio of carbon (left) and gallium (right) with respect to platinum, as a function of the height.

In general, we identified the following possible root causes:

- An influence of the pad position relative to the GIS nozzle in X and Y direction, which seems to be very important as can be seen in Figure 32. Such an effect has been observed and studied before in case of FEBID structures [23]. In the mentioned study, the inhomogeneous gas flux was attributed as the underlying effect. Since the properties of the gas flux are independent, of the particle used for deposition, this effect has definitely to be considered.
- The oscillating behavior in the Ga/Pt ratio also indicates a patterning sequence related effect, hence it would make a difference if the patterns are processed left to right or right to left.
- An effect, which occurs as pads are deposited too close together, which is referred to as pad proximity effect at this point. A similar effect is already well known, i.e. shadowing effects, at which the geometry of the area surrounding the deposit can block the precursor gas flux, hence leading to a decreased replenishment, which can lead to disruptions in the morphology.

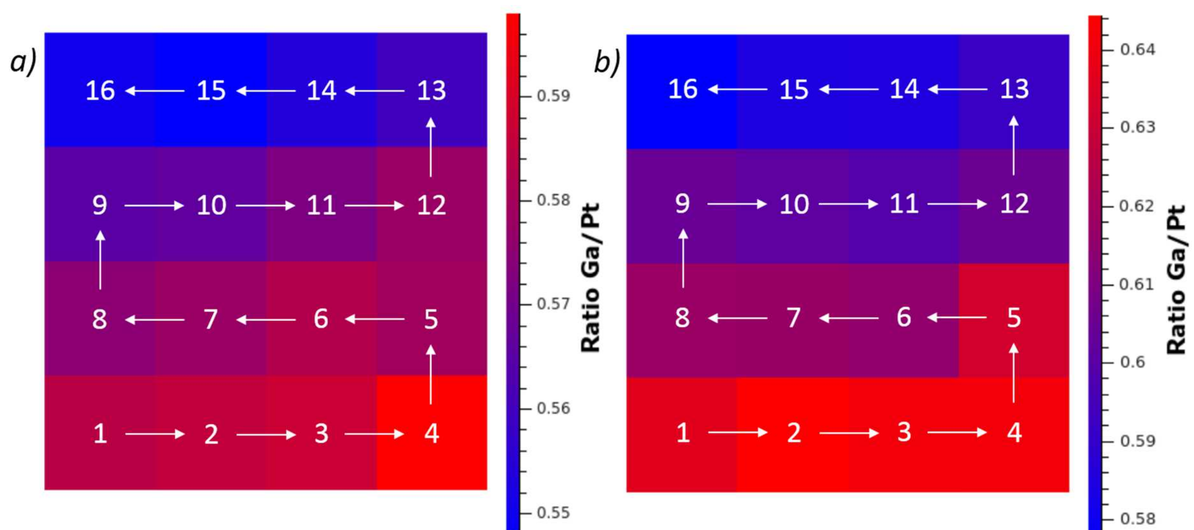

Figure 32: the ratio of Ga/Pt in dependence of the position and the patterning sequence (white numbers and arrows) for 40 pA (a) and 80 pA (b).

3.1.4 Position and Sequence Related Effects

Due to the spatially inhomogeneous gas flux of the precursor, a position related effect is expected in X and Y direction. To separate these effects apart two experiments were designed. At first, the position relative to the nozzle main axis (X) and also the patterning sequence (left to right / right to left) was changed as shown in Figure 33 (a). This was done for 3 series with different distances to the GIS nozzle: 25 µm, 40 µm and 55 µm. In a second experiment 10 pads were deposited in a diagonal manner, at which the distance to the GIS nozzle (Y) was varied from 13 µm to 63 µm (see Figure 33 (b)). For deposition a beam current of 80 pA, a TET of 200 s, DT of 200 ns, OL of -150 % and a pad size of 2 x 2 µm² was used.

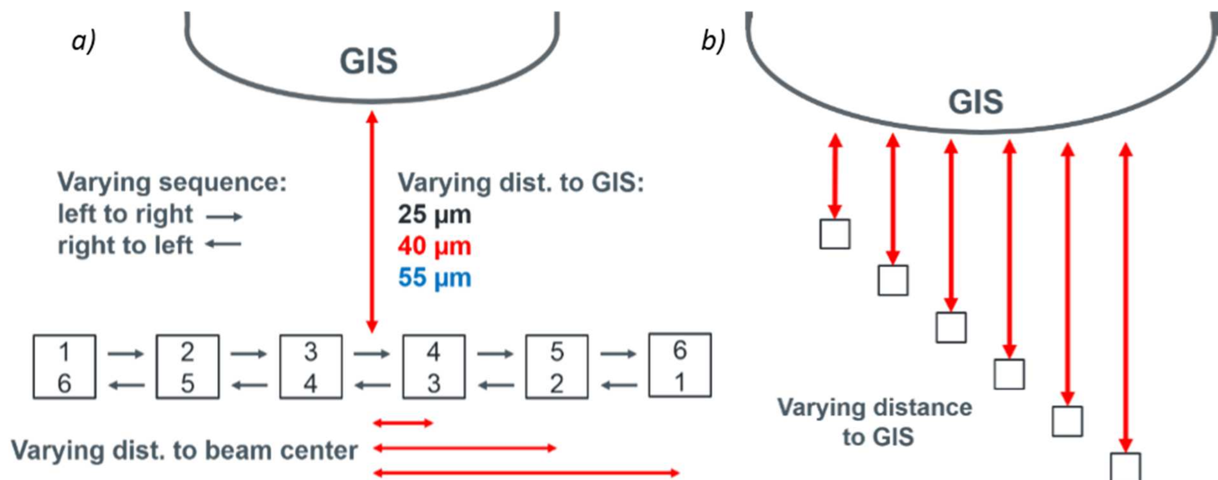

Figure 33: Experimental layout to determine the dependence of the patterning arrangement (X (a) and Y (b)) on the height and chemical composition.

The results from the first investigation show that the height of the deposits seem to be predominantly dependent on the distance to the GIS, rather than on the distance to the main axis or the sequence. This can be seen in Figure 34, which reveals that for both sequences the height increases with a shorter distance to the GIS (a). The Ga to Pt ratio (b) is then widely constant (put attention on the absolute X scale) for all cases at the same distance to GIS, hence no significant position related effect in X direction is observed. Furthermore, one can see that the patterning sequence does not play an important role, as the curves of both sequence directions pair up at the same GIS distance.

The results of the second investigations (Figure 35) confirm the above seen behavior, as we see increasing height (blue) and lower Ga/Pt ratio (red) as the pads are deposited closer to the GIS. The lower Ga/Pt ratio points out that, since the ion dose was kept constant, a bigger volume is formed, hence the ratio is lower.

These experiments show that in the investigated range the influence in Y direction (parallel to the GIS main axis) is stronger than in X direction (lateral position). Therefore, the shorter side of a pattern should be aligned parallel the nozzle axis, to ensure widely constant deposition conditions.

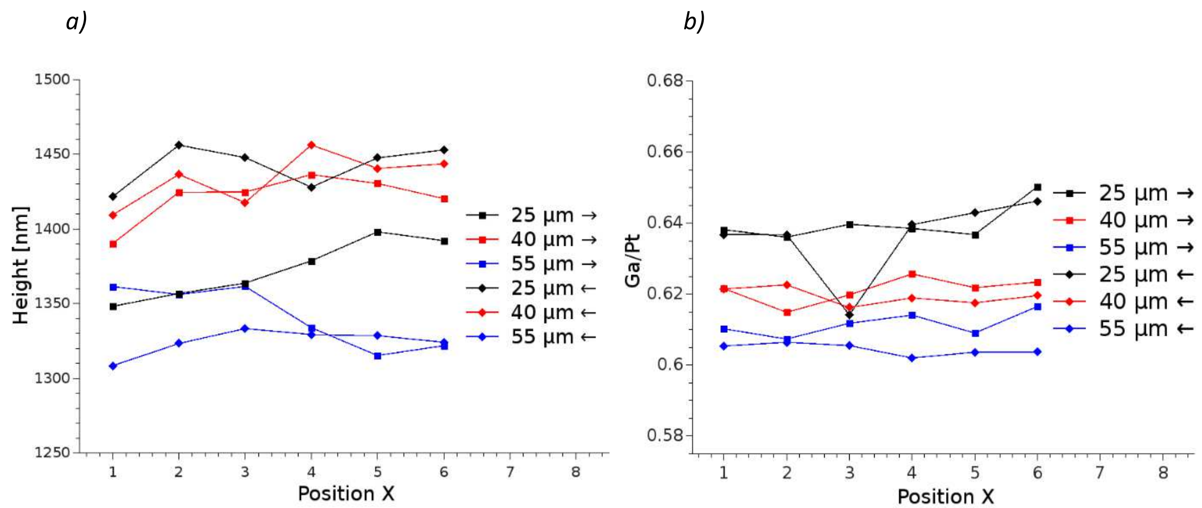

Figure 34: the results of the investigation to determine the influence of patterning arrangement in X direction and patterning sequence on the height (a) and the composition (b). For both figures the color indicate the distance to the GIS nozzle, black for 25 µm, red for 40 µm and blue for 55 µm, the squares represent the sequence from left to right, the diamonds represent the sequence from right to left.

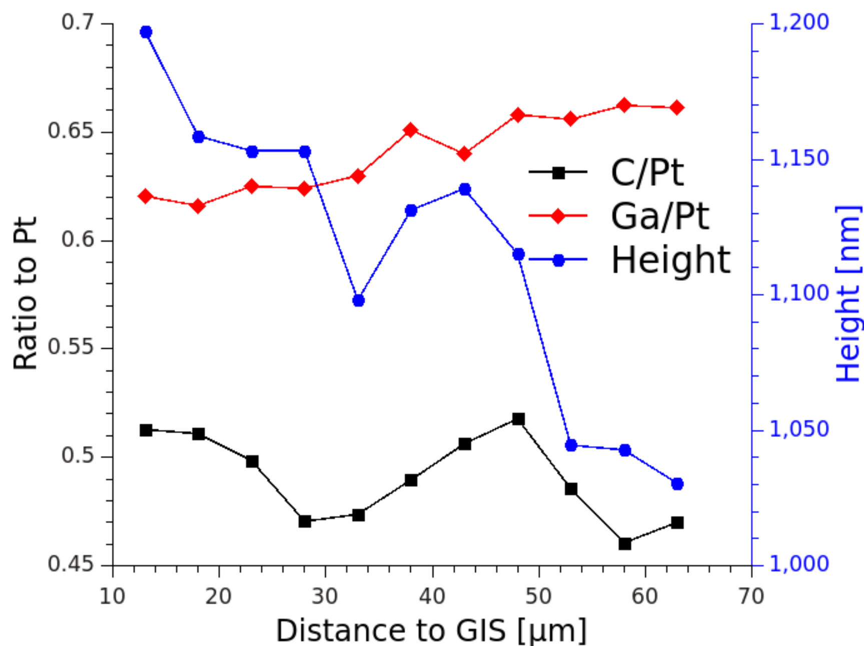

Figure 35: dependence of the C/Pt (black), Ga/Pt (red) ratios (left axis) and the height (blue – right axis) on the distance to the GIS nozzle.

3.1.5 Deposit Proximity Effects

The next effect to be investigated is due to the proximity between the deposits, which was also observed before by [41], where it was referred to as precursor molecule reflection. However, this effect and its root cause are not entirely understood, which will be pointed out here. For this investigation the pads were arranged in a layout, as shown in Figure 36 for three test series. First 10 pads were deposited at a certain distance to the nozzle (40 µm for series 1 and 2, 60 µm for series 3),

further 10 pads would be deposited in front of the first row, while varying the distance relative to them. The deposition parameters for series 1 and 3 were kept at the same values as for the previous experiment. For series 2 only the TET was changed to 100 s.

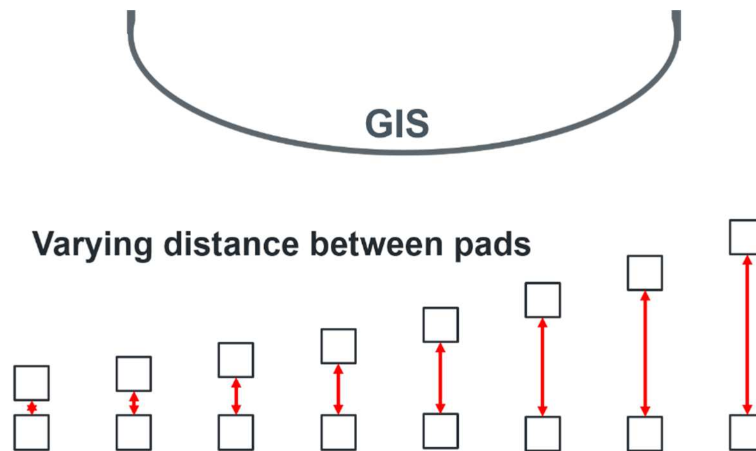

Figure 36: the experimental layout to investigate the dependence on the distance between deposits.

The results show, as in the 2 experiments before, the increase in height with decreasing the distance to the nozzle, the right branch in Figure 37. But this time also an increase in height with decreasing distance to the first pad was observed. This result is consistent with the Ga/Pt ratio, which reveals a high decrease as deposits are deposited closer to each other. The same effect vice versa is observed for the ratio of C/Pt. This behavior, however, has a very short range as already at a distance of about 5 µm and above the ratios and height will not change until coming sufficiently close to the nozzle.

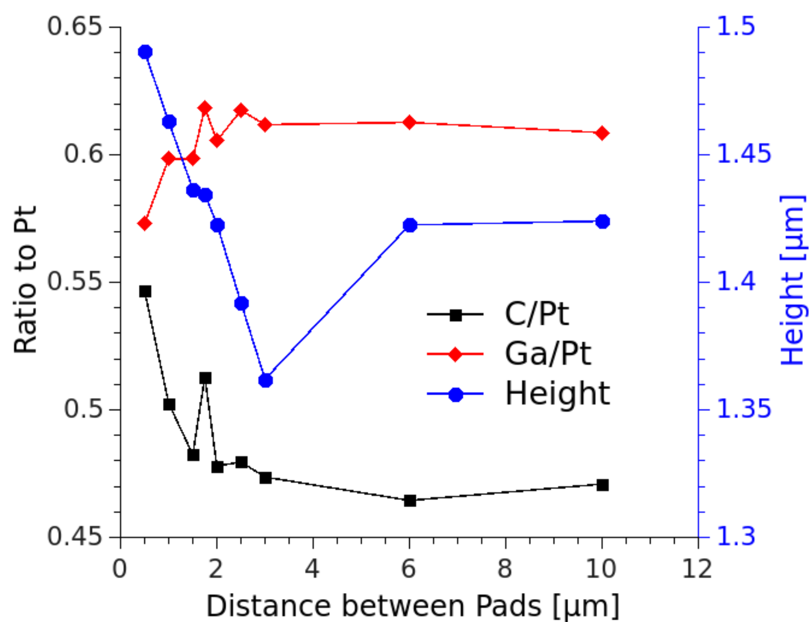

Figure 37: dependence of the C/Pt (black), Ga/Pt (red) ratios (left axis) and the height (blue – right axis) on the distance between deposits.

For this effect however there might be 3 root causes.

1. **Direct gas reflection**, as shown in Figure 38 (a): the direct precursor gas flux (dark blue) is reflected at the side of a deposit facing the focused particle beam, hence enhancing the gas flux (light blue).
2. **Adsorption – Desorption**: precursor gas is adsorbed at the side of the deposit facing the focused particle beam, subsequently it desorbs and a part of the precursor gas is directed to the irradiated area. Comparable to the former, but the additional gas flux would have no predominant direction in contrast to gas reflection.
3. **Proximity effects**: another possible cause of a pad proximity effect, as shown in Figure 38 (b), might emerge due to backscattered ions (red arrows), which are entering the side of the pad, subsequently generating secondary electrons (green arrows), thus enhancing the dissociation process.

However, it is assumed, that the enhanced growth can be credited to gas reflection, as the first measurements have shown, that the deposition regime is precursor limited, thus more dissociating particles would not give a higher C/Pt ratio.

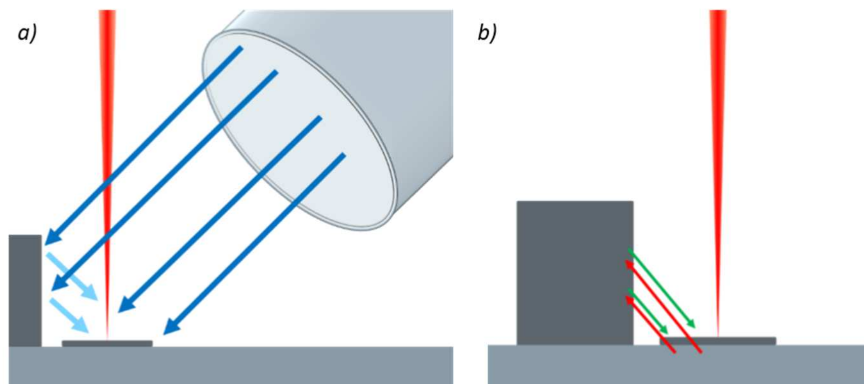

Figure 38: a) enhancement of the replenishment by gas reflection at deposits. b) enhancement of the dissociation process due to a higher SE yield.

3.1.6 Side Effects Summary

It was possible to show that as long pads are deposited in the same working regime, the VGR for the target dimensions is widely dependent on the ion dose and not solely on the currents investigated (40 pA, 80 pA, 230 pA). Also the experiments undertaken in this section have shown that side effects may have mainly 2 root causes, which are the inhomogeneous precursor flux and the patterning arrangement. In general, we observed increasing deposition rate and therefore decreasing Ga/Pt ratio with a shorter distance to the GIS nozzle. On the other hand, the VGR and composition of the pads seem to be less dependent on the distance relative to the GIS main axis. Furthermore, it was shown that a decrease of distance between deposits results in a higher deposition rate, therefore, a lower Ga/Pt ratio. The investigations in the next section about the functionality will give a qualitative correlation between composition and functionality which is more relevant for the aimed CE application.

Generally, it is recommended, to keep a distance of more than 5 µm between the pads and to align smaller side parallel to the GIS nozzle main axis. For long connections one should also consider effects due to gas flux inhomogeneity in X direction.

3.2 Functionality

3.2.1 Introduction

To get a comprehensive understanding of the deposit functionalities, information about the VGR and chemical composition are not sufficient. It is also required to relate these properties to the resistivity which are essential for any kind of electrical measurements. In particular, 4 point measurements are necessary, as mentioned in chapter 2.3.2. This technique allows to eliminate contact resistances between the electrical prober and the deposit and by that access the real resistance of the FIBAD structures. The main aim of this chapter is to determine the patterning parameters in order to deposit a connection with the highest possible conductance in the lowest time. This is done for deposition beam currents of 80 pA, 230 pA and 430 pA by systematic variations of the patterning parameters, while keeping the TET and by that the total ion dose constant. Other criteria for the quality of the deposits are their morphology and the necessary post deposition treatment, at which the surrounding area is etched to avoid shorts to other structures. This becomes especially important if several paths are deposited in close proximity to each other.

3.2.2 Substrate / Test Structure

As the aim of this work was to improve the functionality of the deposits for CE applications, the measurements ought to be as close as possible to the finally aimed situation. For this purpose actual ICs, provided by ams AG [7], were used instead of specially prepared test structures, making the results fully representative and applicable without any further restrictions. The substrate itself consist of a 1 µm thick SiO_2 top layer which serves as a passivation for the circuits underneath. The most upper metal layer consists of Al metal lines with widths and heights of 500 nm sandwiched by 100nm TiN_x layers above and below the metal lines.

3.2.3 Probe Pads

Probe pads are necessary for this investigation, as they provide a sufficient area in order to contact the deposit in a reliable way. Probe needles were bought from Micromanipulator, made of tungsten, with a final tip radius of about 5 µm. Hence contacting deposits with a size of 1 µm or less is quite hard and may result in physical damage. Since probe pads were used for all further measurements some basic investigations were done on this topic.

Deposition of probe pads is depictured in Figure 39 and was done as following: the passivation would be etched off (a) in a 2 µm x 2 µm field with Iodine precursor (insulating enhanced etch processes, further denoted as **IEE**) above the metal line. The GIS was turned on simultaneously with the ion beam. Etching was done at 80 pA with a TET of 30 s using 200 ns dwell times and OL of 0 % (PoP of 21 nm). Subsequently, the etched hole was filled (b) with Pt or W by depositing a 1.5 µm x 1.5 µm pad with 45 s TET, 200 ns DT, - 150 % OL at 80 pA. Next, a 5 µm x 2 µm connection was deposited with the same parameters and a TET of 210 s. Finally, a pad with a size of 7 µm x 7 µm, 300 s TET, 200 ns DT, -150 % OL at 230 pA was deposited, thus the metal line could be connected with a prober (c) via a pad. After deposition the area surrounding the probe pad was sufficiently etched with IEE to avoid conducting paths to other deposits.

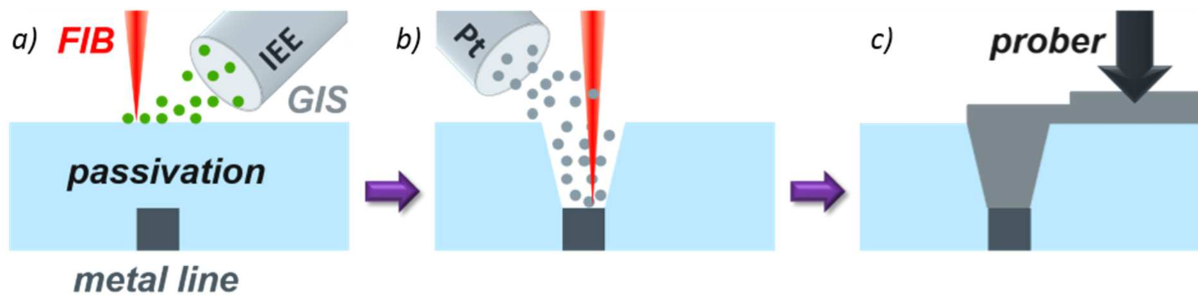

Figure 39: schematic of the procedure for the deposition of probing pads. At first the passivation is etched, using IEE (a), followed by the deposition of conductive material (b), thus the metal line can be connected to an electrical prober via a pad in the end (c).

At this point it was not clear if there would be a difference between Pt and W as probe materials for this investigation. To clarify this aspect, 4 pads connecting the same metal line were deposited and a 4 point measurement was done along this metal line, indicated red in Figure 40, to determine the resistivity. In addition, 2 areas (10 µm x 5 µm) were etched in order to expose the metal line (indicated green), making it possible to directly contact the metal line (blue) with the prober, thus a comparison between measurements using a pad and direct contacting is possible.

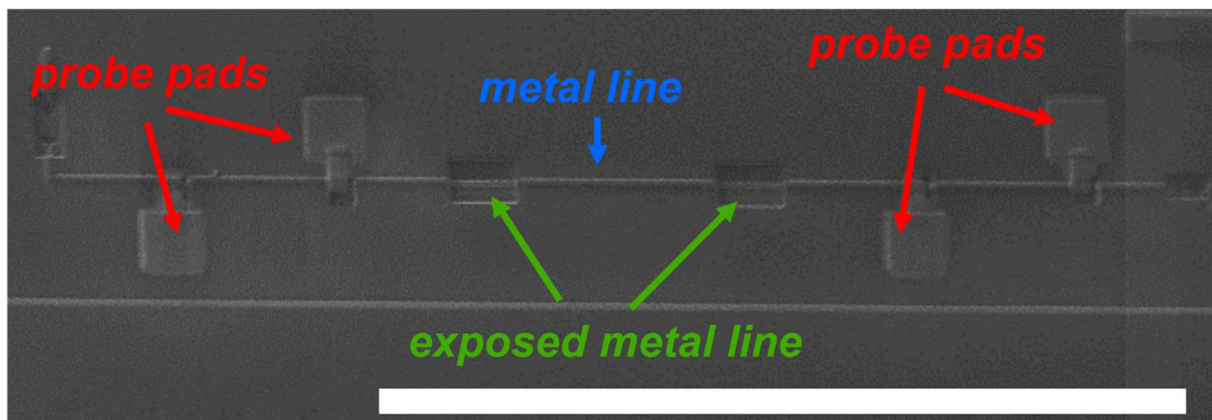

Figure 40: 4 pads (red) were deposited on the same metal line (blue) along with two etched areas (green) to determine the influence of the pads on final electric measurement. The white scale bar corresponds to 100 µm.

The results are given in Table 3. As expected the so determined resistivities lie within the same range, without any significant difference between used precursor, nor pad or direct measurement, thus no influence of the pads for the measurements undertaken in this thesis is observed. Furthermore, the measured values are in agreement with the resistivity of aluminum, thus it is assumed that the measurements represent the real values and no further effects have to be considered.

Table 3: The resistivity of an Al metal line measured through W and Pt pads, also direct measurement on the metal line in comparison to the true value for Al. The uncertainty was determined by taking into account the size of the pads and the prober needle.

Pad	Resistivity [nΩ m] (± 3)
Pt	26
Pt on wire	25
W	26
W on wire	28
Al	26

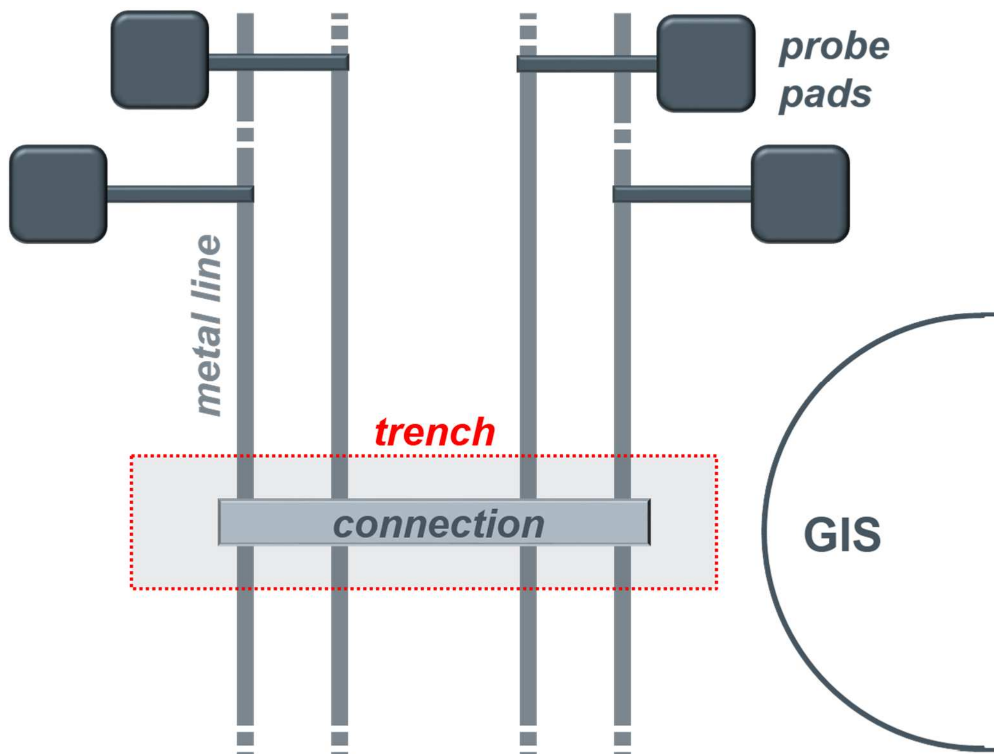

Figure 41: 1st experimental layout for the 4 point measurements: each metal line was connected with a probe pad, a trench was etched into the passivation to deposit a connection and measure the resistance of it.

3.2.4 Resistance Measurement

3.2.4.1 First Layout

The first layout for the resistance measurement used 4 metal lines, which would be each connected by a probe pad as shown in Figure 41. In order do deposit a connection to the metal lines the passivation covering them was etched using IEE, resulting in a trench of 16 x 5 µm². Connections with a base area of 1 x 12 µm² were deposited in the trench using Pt with 200 ns DT and -150% OL. The GIS nozzle was aligned parallel to the fast axis, in order to have the least favorite arrangement. Investigations were carried out for beam currents of 40 pA, 80 pA, 230 pA and also 430 pA. During this investigation we saw no further need to deposit structures with 40 pA, as it was possible to deposit

the smallest structures sufficiently with 80 pA and a much lower TET. However, during investigation a major problem of this layout became evident, which is depicted in Figure 42. A comparison between a connection deposited on the surface without any structure nearby (a) and a connection deposited in a trench (b) shows that proximity effects as discussed in section 3.1.5 occur. Due to the trench walls gas flux replenishment was enhanced (green arrow). To emphasize this circumstance, the cross section is outlined red in both figures, clearly showing a larger volume for the deposit within the trench. Therefore, this layout is not representable for real CE and a different layout had to be found.

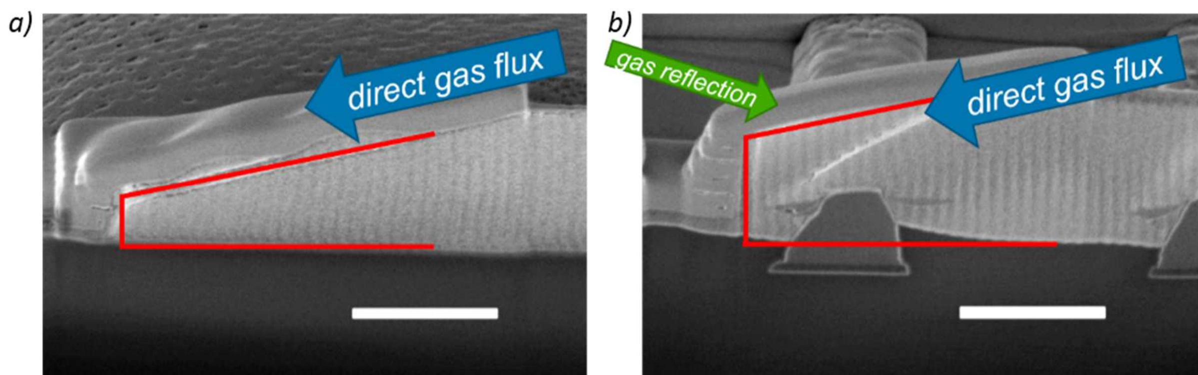

Figure 42: a direct comparison of a connection deposited without any structures nearby (a) and deposited within a trench (b). The direct gas flux (blue arrow) is enhanced through gas reflection (green arrow) due to the trench walls. Thus the structure is bigger in the end, which is indicated by the red outline. The white bar represents 1 µm.

3.2.4.2 Second Layout

The design for an improved layout was motivated by the requirement to avoid pad proximity effects and to approach a more realistic CE situation, where connections are only deposited between two metal lines, but still allow 4 point measurements. A compromise between these demands was found with a layout as shown in Figure 43, where the distance between inner and outer probe becomes virtually zero. The metal lines become accessible for electrical measurements by depositing 2 probe pads at each of their respective ends. Subsequently, the metal lines would be connected by the connection of interest. The connection is sourced for 180 s with an electric current of 100 µA through opposite probe pads (A), while the voltage is measured by the other two probe pads (V). Thus, the resistance is accessed only along the overlapping path of both “signals”, indicated as the purple line in Figure 43, which is a sum of the contact resistance between the central connection - metal lines and the resistance of the deposit itself, also including morphologically different areas, which was not feasible with the 1st layout. Another advantage of this measurement setup is the easy accessibility to metal lines with varying distance to each other. The contact resistance can be estimated by connecting several pairs of metal lines with varying distance between them and plotting their resistance vs. the distance would give an intercept at zero length. According resistance measurement yield the same results regardless of changing the side of sourcing and measuring, or the position of the connection relative to the probe pads. However, it should be emphasized that the surface around the pads and connections has to be absolutely clean in order to obtain the resistance only at the desired pad.

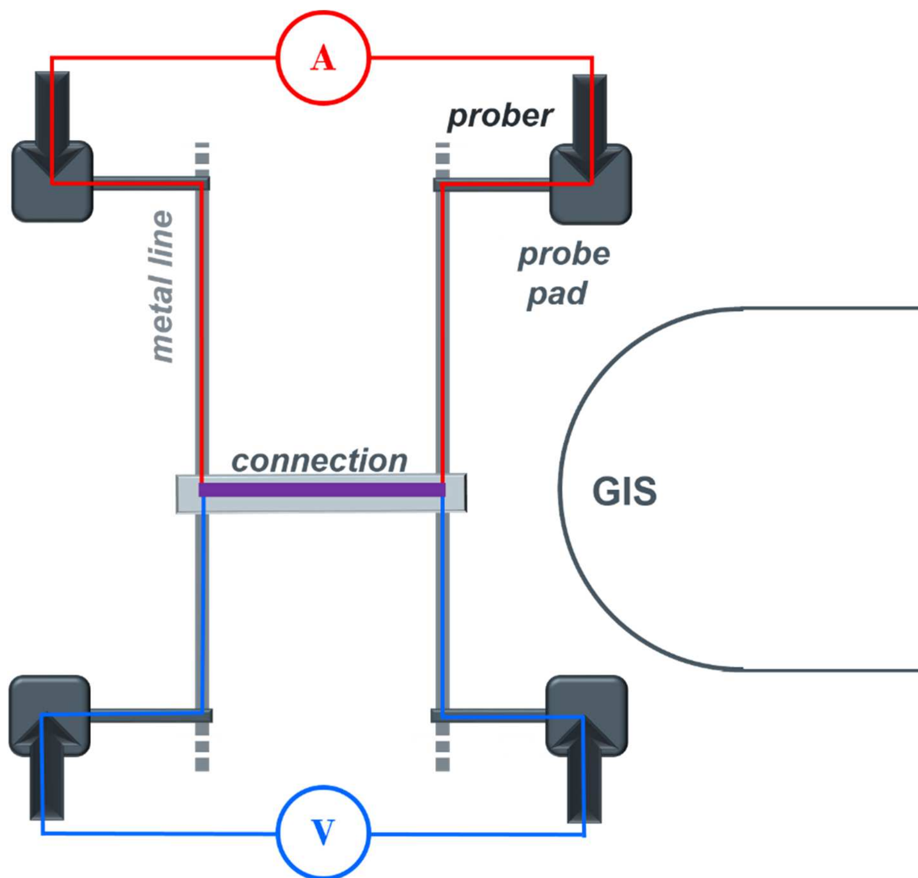

Figure 43: 2nd measurement layout to determine the resistance of a connection. The resistance is only measured along the purple line.

The procedure of the connection deposition process is shown in Figure 44. The etch and fill step (a), in order to make a contact between the connection and the metal lines, was done in the same manner as for the probe pads (Figure 39). After deposition of the connection with the length L (b), considerable amount of overspray was present. Overspray is the unwanted deposition around the intended structure, due to the spatial extent of the interaction volume of the particle beam with the bulk. An example of a connection and its surrounding overspray is shown in (e). Hence, to avoid shorts to other deposits, an area (red shaded) of about (30 + L) x 15 µm², with a cutout of (L+4) x 5 µm² for the connection itself, was sufficiently etched using IEE (c). After resistance measurements the connections were cut (red shaded) in the middle to make sure only one deposit would contribute to the resistance measurement at a time (d). Subsequently, this process was repeated, thus it was possible to deposit several connections at the same pair of metal lines. In order to determine the resistivity of a connection a protective layer of W or Pt was deposited for Pt and W connections respectively, followed by cross sectioning the connection at this position and measuring the height in the middle.

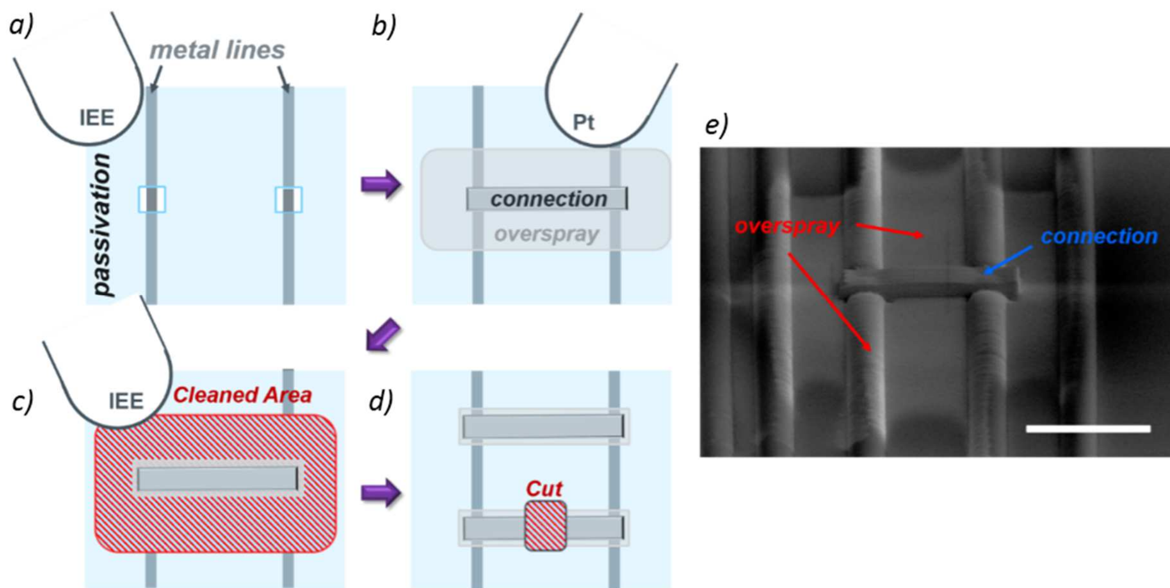

Figure 44: a) etching the passivation at 2 positions in order to gain access to the metal lines. b) A connection between the metal lines is deposited. At this step a high amount of overspray (light grey) was present surrounding the actual deposit. c) Therefore the area (red shaded) around the connection was cleaned using IEE. After the resistivity measurement the connection was cut, and steps a – c was repeated. Thus a pair of metal lines could be used for several connections (d).

3.2.5 Dwell Time (DT) Variation

Optimization of deposition parameters started by varying the DTs, as it is the most significant patterning parameter. For that, connections with a base area of 20 x 1 µm² were deposited as shown in a layout as shown in Figure 43 in a manner as shown in Figure 44 using a beam current of 230 pA, -150% OL (PoP of 95 nm) and a TET of 400 s. The results are shown in Figure 45 and show a distinct resistance minimum for a DT of 550 ns (black squares). However, another test series with a connection length of 6 µm and a TET of 120 s shows a distinct minima of resistance for a DT of 250 ns (red diamonds).

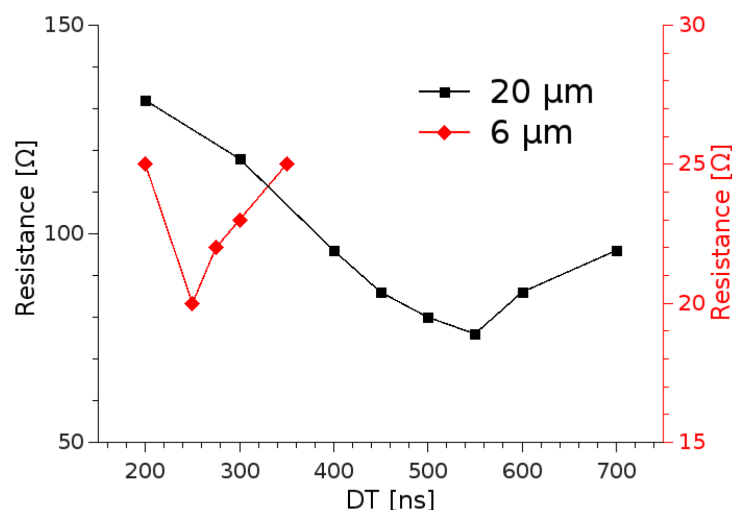

Figure 45: DT sweeps for connection lengths of 6 µm (red diamonds) and 20 µm (black squares) with an identical TET per length of 20 s/µm revealing distinct minima for different DTs.

To get a better understanding of the relationship between lengths and optimal DTs more measurements were performed with lengths of 6 µm, 7.5 µm, 10.5 µm, 16 µm, and 20 µm with a TET of 20 s/µm each and 40 µm with a TET of 400 s, thus keeping the total ion dose constant, except for the 40 µm connection. The TET was chosen such to be about the mean value of the target regime. The results, shown in a semi logarithmic plot Figure 46 (a), clearly indicate a logarithmic dependency of the optimal DT on the length. Plotting the resistance at optimal DT vs. the length, as shown in Figure 46 (b), and linear fitting of the data points, reveals linear behavior. Thus making it possible to estimate the contact resistance, which is in this case about 9 Ω for each contact between connection and metal line.

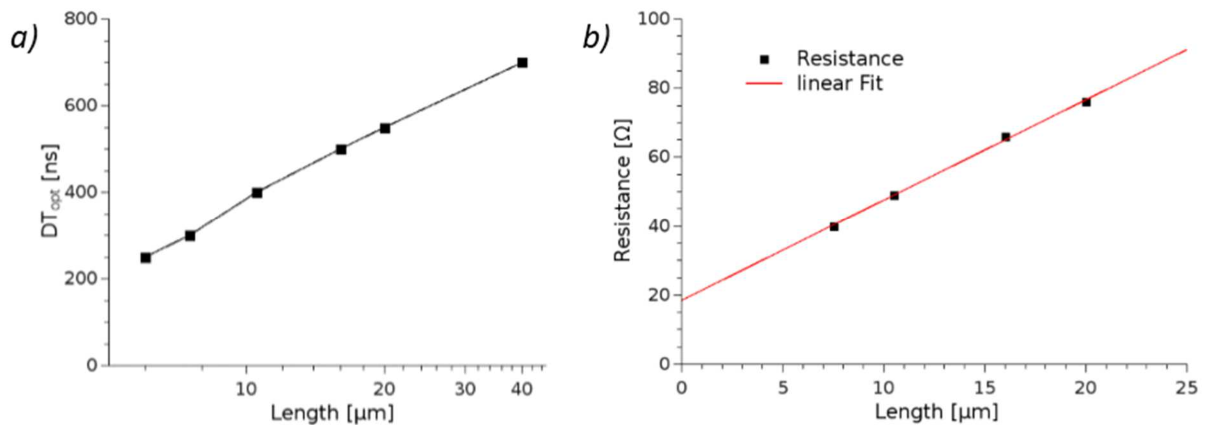

Figure 46: DT behavior for several deposit lengths with constant footprints on a semi-logarithmic scale (left) and the total resistance for deposits with an equivalent TET per length of 20 s/µm for the determination of the contact resistance (right).

However, the question arose, if the same curve would be found for other beam currents and if not how they would scale with the length. Therefore, a series of measurements was done with a beam current of 430 pA, a TET of 10 s/µm and OL of - 150 % (PoP of 132.5 nm). The results showed as well semi-logarithmic behavior depicted in Figure 47 by the red diamonds / line. However, the higher ion dose leads to a shift of the ideal DTs towards lower values (compare to 230 pA by black squares / line). Considering the beam current and the length of the deposit it was possible to formulate a mathematical expression (equation 4) which holds for both data sets as given in Figure 47 and further refined in the following.

To prove that this law would also apply for other beam currents, the optimal DT curve for 80 pA was predicted with the modified equation 5, written below. The curve for the optimized DT was experimentally determined (TET of 40 s/µm) and showed consistency between experiments and prediction in Figure 48.

In order to gain a better understanding of the relation between geometry, and optimal DT further measurements were performed changing the width of the deposits, while keeping the TET constant for the respective beam currents. Therefore, the law was modified to be dependent on the number of patterning points and the beam dose. Measurements with smaller and wider widths at different beam currents and lengths showed an optimal DT in agreement to this law. Even if the area of the connection

would become as large as 210 µm² with a DT of 850 ns at a beam current of 430 pA, the prediction and the result showed perfect agreement. The fitting parameters are c_1=208.77 ns; c_2=0.0052 and were determined using the Matlab function nlinfit.

$$DT_{opt} = c_1 \ln(c_2 \frac{A}{(1-OL)^2\, d_B^2}) \qquad \textbf{(4)}$$

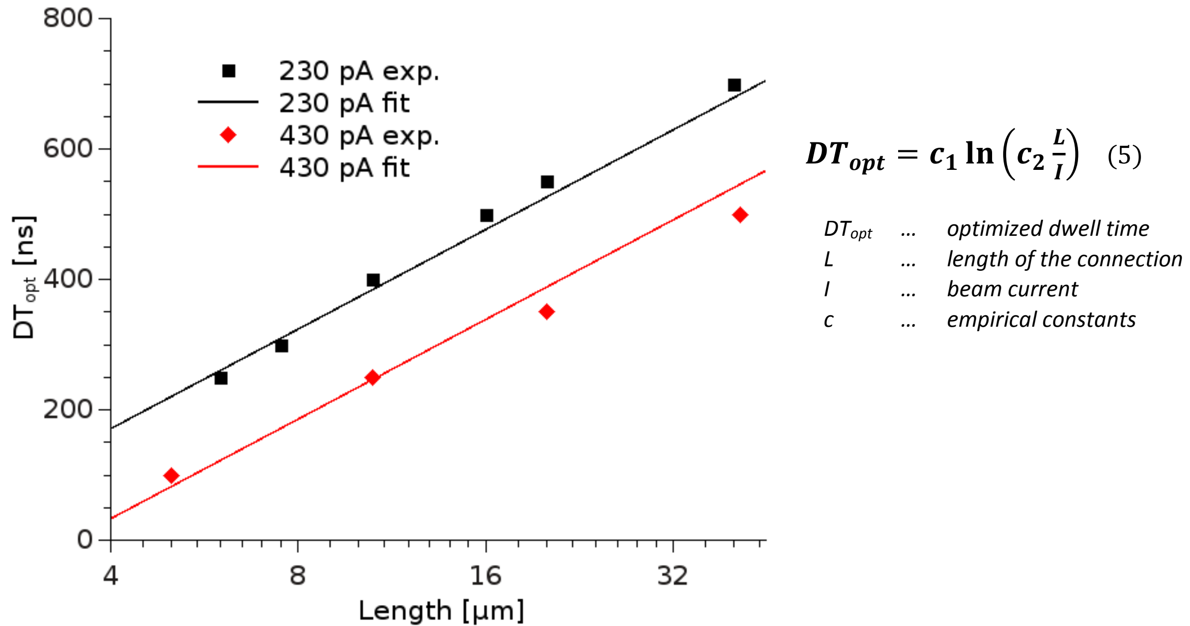

Figure 47: experimental results for optimum DTs vs. deposits lengths for 230 pA (black) and 430 pA (red) fabrication currents. The solid lines are calculated with the equation at the right.

Yet it has to be emphasized that the derived relation is most likely dependent on more parameters than only the DT, geometry and beam current. One should keep in mind that these experiments were performed with the same GIS alignment, thus we would expect a change in the constants if the nozzle alignment was changed. Hence, another system will most likely have different constants for the DT_{opt} law. However this law can be adjusted to every particular system by performing 2 DT optimization series at a certain beam current and inserting the results into equation 5, or by typing in the results in an excel table, which is provided in 5.1 Appendix 2 – Spreadsheets for updating the diagrams.

It has to be mentioned here that the dependence of the DT on the base area is rather artificial, in fact the base area is just the value which relates the DT to the RT. The relation between RT and DT indicates that for most efficient deposition the optimal ratio between replenishment and depletion of the precursor gas is the determining factor. As the RT increases more precursor gas will cover the area of irradiation, hence a higher DT is necessary to deplete the precursor molecules. Unfortunately, it was not possible to underlay this statement with any simulation, as there are several parameters not known, like the sticking coefficient or the exact residence time, furthermore there is no simple code for such a simulation, actually simulating the DT – RT behavior would probably be worth a whole thesis

on its own. Nevertheless, the relation between depletion and replenishment would suggest a saturation of the DT, as the coverage in dependence on the RT saturates at one point. The saturation value for DT_{opt}, however was not found in the frame of this work.

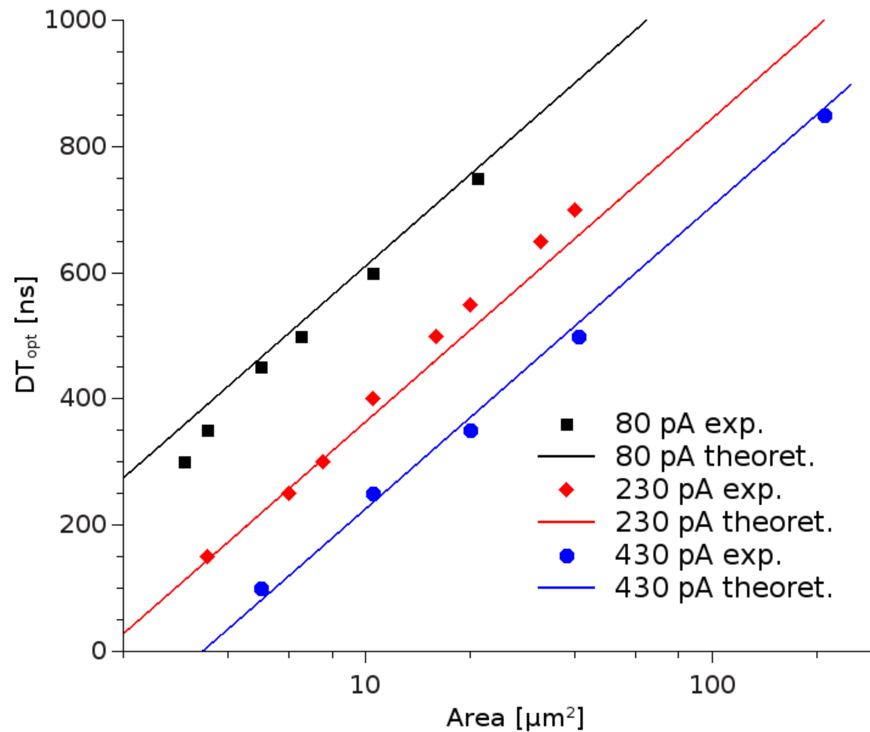

Figure 48: the optimization of the DT for several base areas (x-axis) and beam currents (points) and the derived theoretical DT_{opt} (straight lines) show that it is possible to predict the DT for a connection with the highest efficiency, regarding the total resistance.

The practical value of this section, however, is the fact that predictions can be done for any systems after performing one DT vs. length sweep which then acts as fitting base for the above given expression. By that, it becomes easy to transfer the predictability for any given machine and allows precise control for the optimal DT values.

3.2.6 Overlap

The next most important parameter considered for optimization is the overlap. As previously mentioned in section 2.1.10 the OL is a 2 dimensional parameter, due to a different replenishment – depletion situation in the fast and slow scanning direction. This was considered in the investigation, by changing both values in a matrix like sweep for connections with a base area of 9 x 1 µm² DT_{opt} of 350 ns, at 230 pA and a TET of 180s, OL_x and OL_y values of - 100 %, - 150 %, - 200 % (PoP of 76 nm, 95 nm and 114 nm, respectively). The result is shown as a surface plot in Figure 49. This experiment reveal that for the considered working regime no difference between OL_x and OL_y can be seen, as there is no significant difference in the resistance for a connection with -100 %, -150 %, -200 % for OL_x and OL_y or vice versa, except for the case of increasing both OL values up to -100 %, which resulted in a notable

increase for the resistance, accompanied by a highly disrupted morphology of the connection as the red framed picture in Figure 49 shows. Decreasing both OL values down to – 200 %, shows no increase or decrease for the resistance but a change in the morphology of the surface becomes visible, revealing a fine periodical wavy behavior of the surface, as can be seen on the left edge of the connection, depicted in the orange framed picture. The difference in resistance for low OL lies in the same nature as a too high DT. Due to the higher proximity of neighboring patterning points the beams of neighboring points overlap more, resulting in a higher depletion, thus the same result is observed as for a high DT, when massive depletion lead to a decrease of efficiency. Apparently an OL of -150 % seems to be the best choice and no further investigations were conducted, as it will not improve the functionality of the deposit.

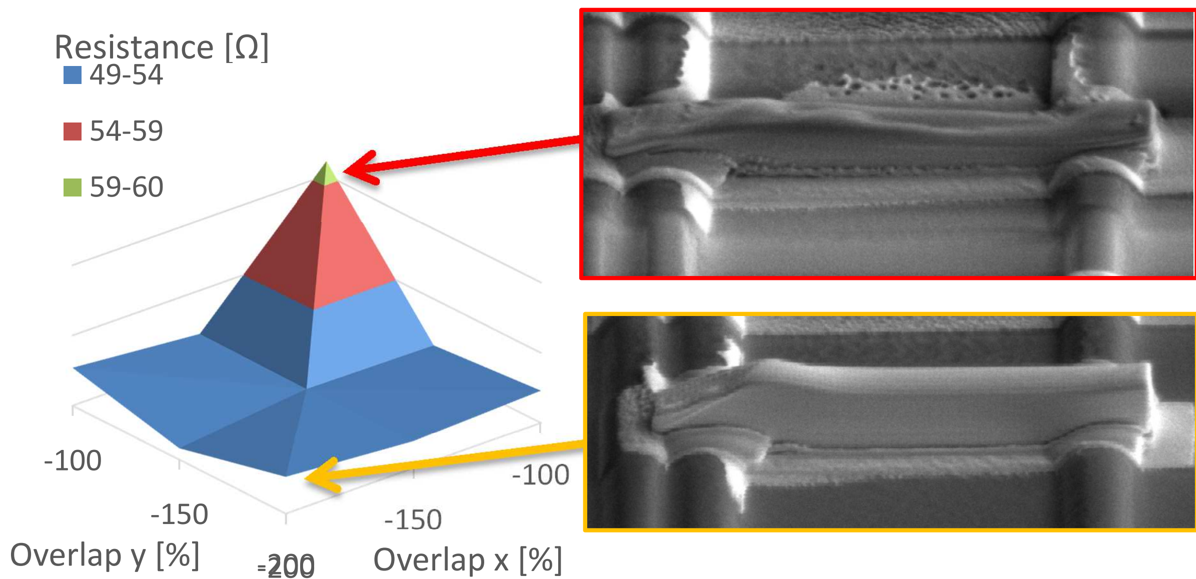

Figure 49: deposit resistance with varying overlap in x and y direction. The red framed picture shows a connection with a highly distorted morphology, the orange framed picture shows a wavy point pattern on the surface, which can be seen especially on the left edge.

3.2.7 Defocus

To see how the overall functionality relates to the beam defocus during patterning, 2 connections were deposited with 230 pA, 180 ns DT, 95 nm PoP (-150 % OL), and a defocus of 0 µm and 50 µm along -Z. The measurement revealed that the connection deposited with defocus has a lower resistance of 45 Ω compared to 50 Ω with no defocus applied. However, the decreased resistance comes along with a significantly higher overspray, which first became evident by a significant longer cleaning time after deposition. For a better understanding cross sections of such connections were investigated. An example is shown in Figure 50, at which at first (a) a protective layer (SiO_2) was deposited on the connection. Afterwards a field of 9 x 5 µm² with a depth of 2 to 3 µm was sputtered away in such a way that the cross section of the connection and the protective layer becomes visible (b). Magnifying the image (b) makes the amount of overspray clearly visible.

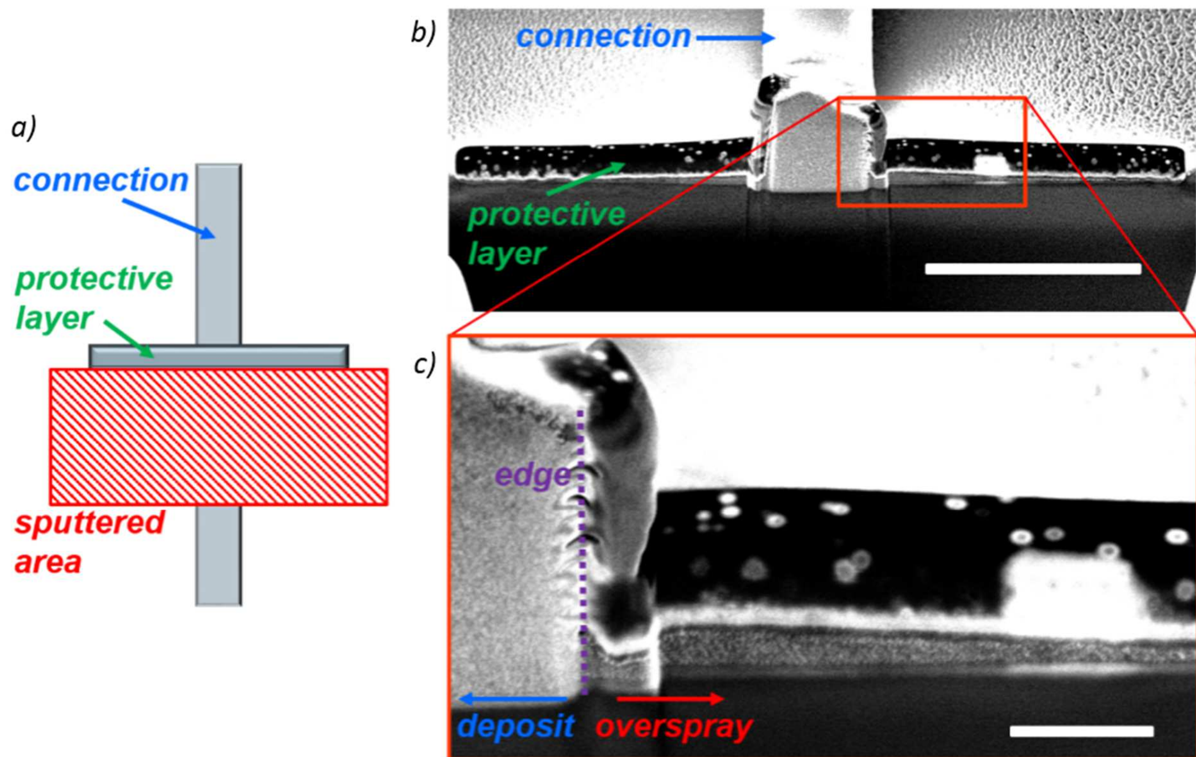

Figure 50: a) schematic overview of a cross section investigation, which was also used to determine the general height of connections. Across the middle part of the connection a protective layer is deposited. Subsequently an area is removed by sputtering. b) Now the cross section of such a connection can be investigated (white scale bar is 3 µm). c) Magnifying the cross section shows the edge of the deposit (indicated purple), which separates the intended deposit (blue) and the unwanted overspray (red), the white scale bar corresponds to 500 nm.

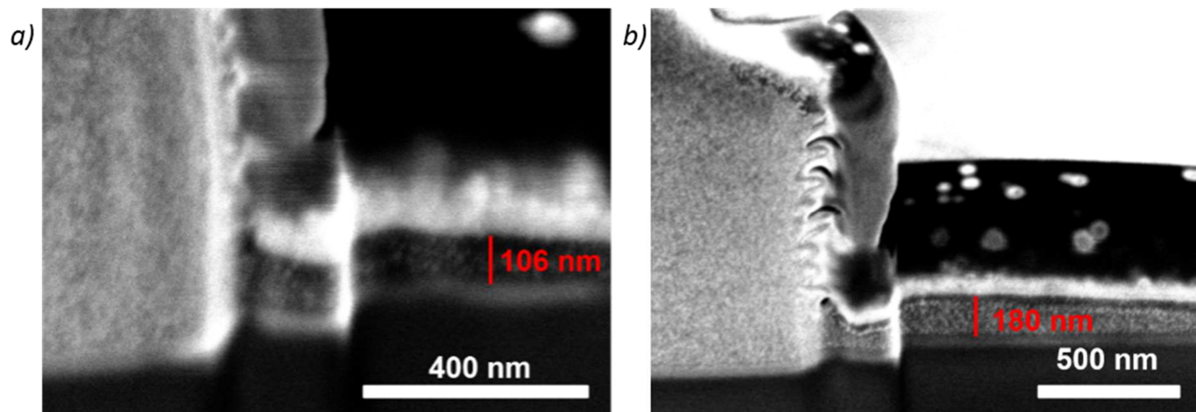

Figure 51: comparison between 2 connections deposited without (a) and with (b) defocus, shows that due to the applied defocus a significantly higher overspray close to the deposit occurs. The cross sections are made in the manner, which is described in Figure 50.

The comparison of the cross sections of the here investigated connections is shown in Figure 51. While the connection deposited with no defocus has an overspray thickness of about 106 nm at about 500 nm away from the edge of the deposit, the connection deposited with defocus exhibits a film thickness

at the same position of 180 nm. The increased amount of overspray necessitates a longer cleaning procedure after deposition, which also means that the total ion beam damage is increased. Therefore, a defocus does not improve the overall efficiency of a connection and should be avoided. This also shows that the operator should also keep in mind to focus the FIB at all times.

3.2.8 Relation between Resistance, Resistivity and Volume Growth Rate

In most studies the main focus lies on the resistivity instead of the resistance. The reason for it is simple, as the former is independent on the deposit geometry and by that a sole material parameter. In other words, the value is the same no matter whether the deposit is 1 µm or 100 µm long. However, in this section it is shown that only minimizing the resistivity or maximizing the VGR is not the road to success with respect to the most efficient parameter set for CE applications. This issue is discussed in this chapter for a 6.5 µm long connection, deposited with 80 pA, a TET of 260 s, OL of – 150 % (PoP of 52.5 nm) and varying DT. Figure 52 summarizes the results for total height (red) and resistivity (black), as well indicated is the DT with the lowest resistance (green dashed line). As immediately evident, the lowest resistance is NOT achieved for lowest resistivity but for a DT_{opt} around 500 ns. Looking only at the resistivity, no minima can be found at that point which seem to be in conflict on the first glance. Neither does the chemical composition show any saturation of the C/Pt or Ga/Pt ratio in this regime, as shown in Figure 53. In fact due to the increasing Ga incorporation for higher DTs, it can be assumed that in the extreme case the resistivity would only saturate close to the value of Ga itself, which would be 27 µΩ cm, thus even values were reported with a resistivity as low as 70 µΩ cm in [3], which was achieved at the highest used line dose. Like the resistivity, the VGR is enhanced at lower DTs (Figure 52) and decreases towards higher DTs. On the other hand C/Pt ratio decreases, while Ga/Pt increases, when increasing the DT (Figure 53). These factors indicate that for a lower DT the precursor gas is less depleted during irradiation, leading to a higher C incorporation, hence a higher VGR. For high DT lesser C incorporation leads to a higher amount of Ga, since the volume is smaller at the same total dose, which subsequently leads to a lower resistivity. The same result was reported in [40]. Furthermore, we see that the morphology for lower DT seems to be qualitatively better and less deteriorated than for higher DT, as examples of the connection at DT of 200 ns, 500 ns and 700 ns show in Figure 52. The morphological deterioration has its root cause in shadowing effects. During deposition the nozzle was aligned such that the gas flux would come from the right side. The effect itself becomes stronger with increasing DTs, as for a short DTs (200 ns) actually the height gain per loop is lower (2.3 pm per cycle) than for longer DTs, thus in **one** cycle less precursor molecules are depleted, while for higher DTs (700 ns) more precursor molecules are depleted leading to a higher height gain during one irradiation event (5.7 pm per cycle). However, in the end a lower DT comes along with a better replenishment situation, thus a better morphology is achieved. But, it should be again mentioned, that in no way it was possible to relate the most efficient DT regarding the resistance somehow to the morphology of the deposit.

In general, the resistivity is indeed decreasing for increasing DTs. On the other hand, the volume growth rate is decreasing due to stronger local depletion for increasing beam pulses. As the final resistance is a mixture of resistivity and the total dimension the thinner deposits give lower resistances due to less efficient growth. From a materials perspective higher dwell times are indeed better but in a practical aspect, the perfect DT values are located somewhere else.

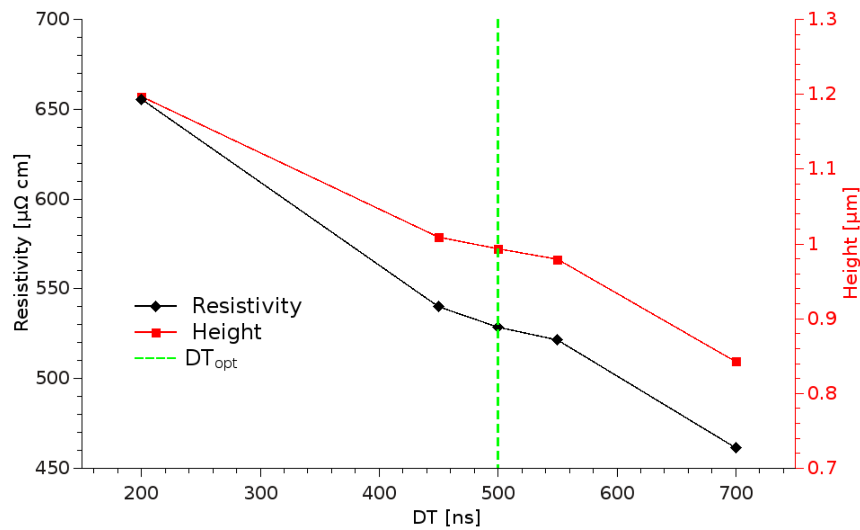

Figure 52: comparison between resistivity (black), height (red) and resistance (blue) for varying DTs, in case of a 6.5 µm long Pt connection deposited with -150 % OL at 80 pA. The green dashed line indicates the optimal DT for this particular connection.

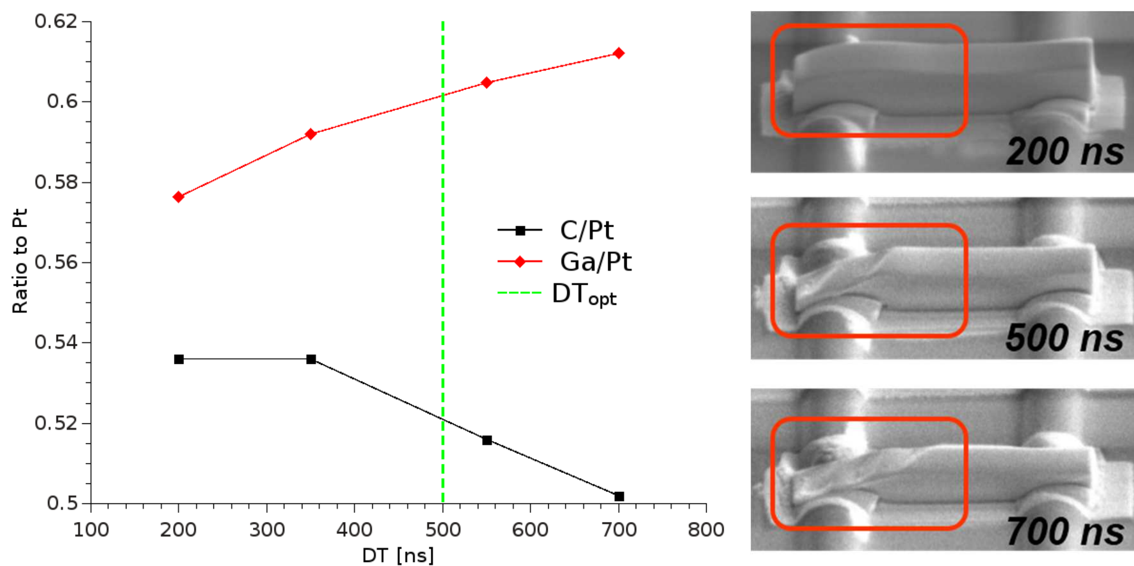

Figure 53: EDX based peak chemical ratio of C (black) and Ga (red) with respect to Pt, also showing the optimized DT (green dashed line) for this particular connection. Next to it are SEM images of the different deposits for 200 ns, 500 ns and 700 ns DT, showing morphological changes (red frame) with increasing DT.

3.2.9 Tungsten

So far the investigations carried out were using Pt precursor and showed that only a variation of DT would increase the efficiency. Therefore, only this parameter was considered for the optimization of W deposits, while the OL and defocus was kept constant at values of - 150 % and 0 µm respectively. This is a valid assumption as it is well known from literature that varying the precursor shifts the precursor regime to different process parameter values but qualitatively remains the same [2]. The investigations started with a DT variation for lengths of 20 µm and 140 µm at a beam current of 230pA.

The results in Figure 54 (a) reveal that for both connections the optimized DT is 25 ns, simply because it is the technically lowest possible DT. Considering the behavior for Pt precursor (Figure 48) it follows that W shows only the increasing branch in the DT sweeps. This is in agreement with the knowledge that the used W precursor has much shorter residence times which therefore requires very short dwell times for ideal properties. However, for shorter connections the variation shows no such clear minima anymore. As an example the resistance vs. DT variation of a 7 µm long connection for TETs of 70 s (black), 45 s (red) and 35 s (blue) is shown in Figure 54 (b). Only for a very short TET a minimum of the resistance is recognizable at 125 ns. For the other 2 series, such a single minimum cannot be exactly determined. For the series with a TET of 45 s there seem to be 3 values, which are minimizing the Resistance, i.e. 50 ns, 150 ns and 300 ns. For the series with a TET of 35 s, the minimum would be between 75 ns or 100 ns. Thus it is simply not possible to say, which DT would in the end minimize the resistance. However, in general a shift to higher DT_{opt} values was observed as the length decreased. This behavior can be attributed to the coupling between DT and RT, as the lowest possible RT is equal to the number of patterning points times the DT. Thus below a certain RT it becomes more beneficial to increase the DT, which in response increases also the RT, hence better replenishment and by that better local coverages are achieved.

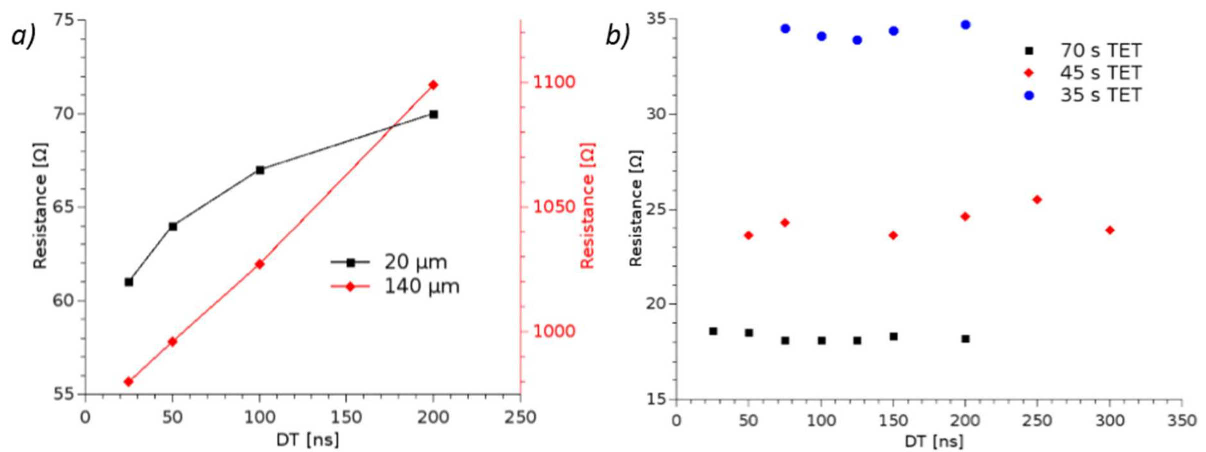

Figure 54: a) the resistance vs. DT for a connection of 20 µm (black) and 140 µm (red), both only show the increasing resistance branch, thus a minimum at a DT of 25 ns is observed, as it is the lowest possible DT. b) for short connections a distinct minima is only visible when the TET becomes short.

Measurements for the chemical composition reveal, that the Ga content is reduced for lower DTs, as can be seen in Figure 55 (a), for DT variation series at 80 pA (red diamonds) and 230 pA (black squares). The lower Ga incorporation with respect to the volume indicates higher VGRs. This is affirmed by direct height measurements on a 25 µm long connection for different DTs as shown in Figure 55 (b) (black squares). The red diamonds give the corresponding resistivity which qualitatively shows the same trend. Thus it can be concluded, that for W it is simply the case that an increased VGR is more beneficial for the efficiency regarding the overall resistance, i.e. to deposit a connection with the same TET with the lowest possible resistance, as has been shown above in Figure 54 (a). It has been shown before, in section 3.2.8, that for Pt this is not the case, at which the most efficient DT, is not only determined by the highest VGR or the lowest resistivity, but somewhere between.

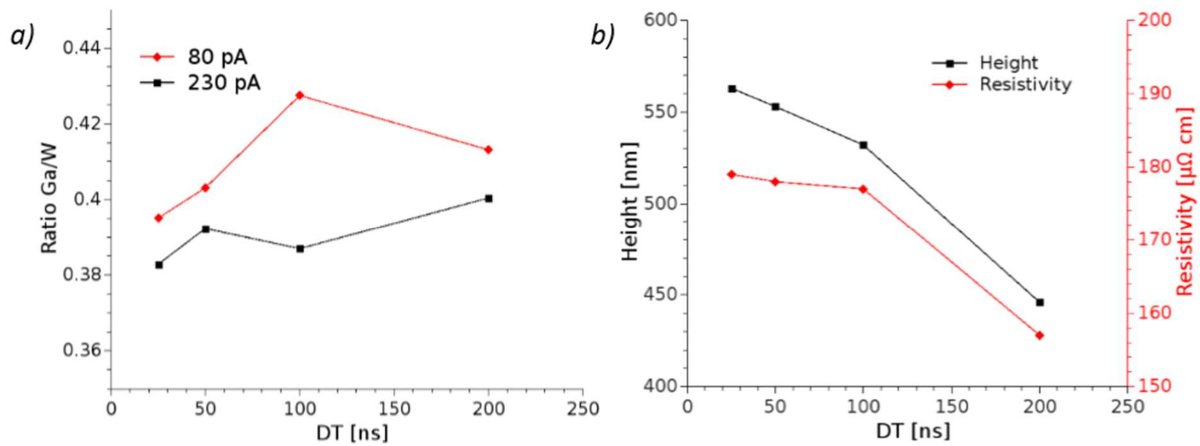

Figure 55: a) the Ga/W ratio as function of the DT for a connection with 25 µm, 80 pA (red diamonds) and 230 pA (black squares). b) the height (black) and resistivity (red) of a 25 µm long W connection, deposited with 230 pA with varying DT.

Comparing the DT_{opt} for Pt and W, shows a much lower value for W. This fact points out the substantially lower residence time of this precursor compared to Pt. Due to the lower residence time less precursor is accumulated during the RT, thus a lower DT is needed to deplete it.

The determination of the contact resistance between Al and W with the method as used for Pt gave no clear results, although for several lengths with comparable TET showed a linearity, the intercept of this curve with the ordinate would result in a negative value, which is not possible. Thus it is assumed that the contact resistance is negligible between Al metals and W / Pt.

A final comparison for the different situations for Pt and W regarding the total resistance and the VGR in dependence of varying DTs is given in Figure 56, the optimized DT in each case is highlighted with a green background. The left column represents the typical results obtained for Pt, the right column shows representative results for W. In the first row the resistance is shown, in the second row the VGR. For the resistance variation of Pt a distinct minimum can be seen, to the left (lower DTs) of this minimum a RT problem emerges (highlighted blue), as the replenishment is too high. Therefore, relatively to the volume the incorporated amount of Ga becomes too low, leading to an increase in resistance. To the right (increasing DTs) a DT problem emerges, due to a too high depletion of the precursor molecules, leading to a too low volume. If, however, one considers the VGR it is possible to see an increase of the VGR towards lower DTs, while for high values again a DT problem emerges. The reason for the increased VGR for low DTs lies in the far better replenishment situation. The fact that the highest efficiency, regarding the lowest resistance, the highest VGR or the lowest resistivity are all at different DTs, shows how strongly the interplay between ion dose, DT and RT can affect the final functionality of the deposits. Furthermore, one can see from Figure 56 how much Pt and W differ in their properties. For W it is clearly the case that the most efficient DT, regarding the total resistance **and** VGR is at low values. Thus one can conclude that for high DTs W deposits suffer from a DT problem, i.e. the balance between depletion and replenishment lies more on the depletion side. This implicates that there are too few precursor molecules for high RTs, which can be explained by a very low residence time and short diffusion length of the precursor on the surface.

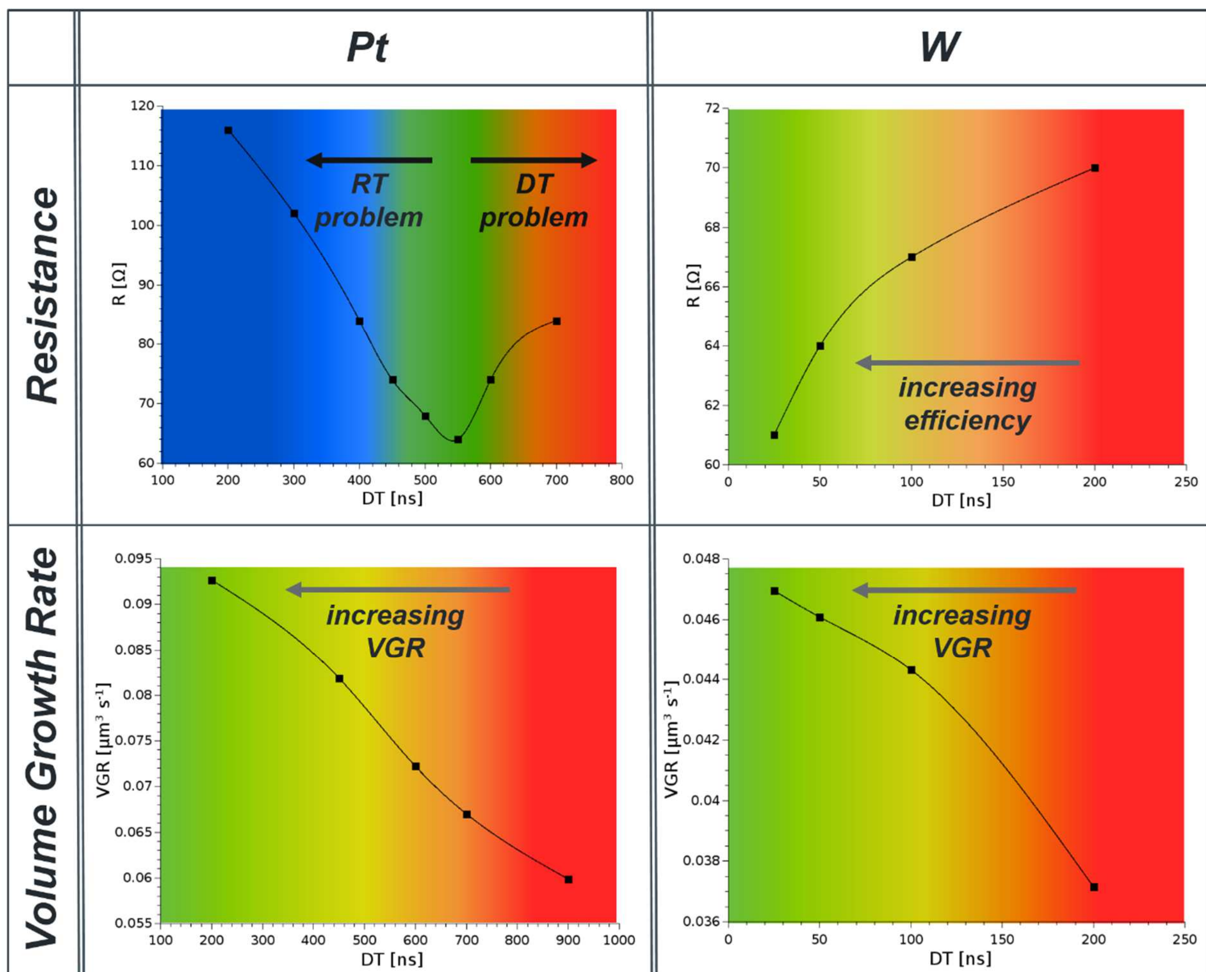

Figure 56: comparison of Pt (left) and W (right) regarding the efficiency with respect to the resistance (upper row) and the VGR (lower row). For the red regions a DT problem is evident (depletion too high), while for the blue regions a RT problem is dominant (replenishment too high). The green regions for each plot show the highest efficiency regarding the resistance and accordingly the VGR.

3.2.10 Height and Length Dependence

It has been reported before that for Pt deposits the resistivity and VGR are dependent on the height [5,23] and change as the deposit grows, therefore this section is dedicated to this topic. Similar behavior, as in the mentioned studies, was also observed in the frame of this thesis and is summarized in Figure 57. For small heights a drastic change can be observed and with increasing height, both the VGR (black circles) and the resistivity (red squares) go towards a saturation, which was determined to be 0.127 $\mu m^3\ s^{-1}$ and 518 µΩ cm, respectively. Considering that the height values where this effect takes place, one can immediately rule out a traversing interaction volume (substrate into deposit) as the origin, since ions have a penetration depth of roughly 100 nm in these materials (Figure 22 (b)). Therefore, two effects could be responsible for this effect: 1) precursor dynamics; and 2) local temperature effects. The former is known to reveal the same tendencies during focused electron beam induced deposition as described in the abovementioned study. The background are simply different replenishment components: diffusion from the surrounding substrate is getting more complicated for higher deposits as they would need to diffuse upwards toward the areas of new deposition. This, however, is limited by the average diffusion length of precursor molecules given by sticking coefficients

and residence times. Once the growth height clearly exceeds this lengths replenishment from the substrate is eliminated. The predominant reload mechanism is then direct gas flux adsorption and short range diffusion on the deposit surface. This is reflected by the constant and non-zero VGR value for higher deposits as evident in Figure 57. At the same time, the regime strongly changes into molecule limited conditions where a high dissociation degree is the consequence which is consistently reflected by the decreasing resistivity. The other effect which might play a role is local heating. The higher the deposit the more complicated the temperature decrease after a beam pulse due to the low thermal conductivity. On the one hand, this would have the consequence of reduced residence times for new precursor molecules which decreases the VGR as observed. On the other hand, increased temperatures might lead to temperature assisted decomposition which further increases the dissociation degree leading to reduced resistivities in accordance with the experiments in Figure 57. While the surface diffusion influence is definitely contributing (studied in detail by Winkler et-al [23,35]) the saturation height of about 1000 nm strongly suggests the temperature effect as additional mechanism as this length definitely exceed the average diffusion lengths of about 100 nm for Pt precursor.

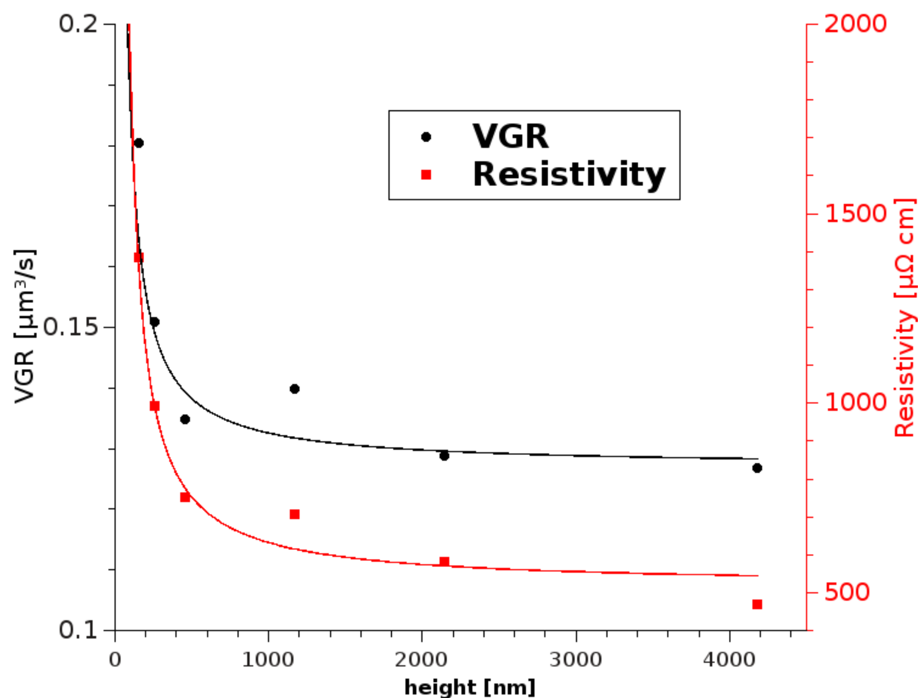

Figure 57: the VGR (black – left) and the resistivity (red - right) change during the growth, depending on the height and saturate above about 1000 nm.

To check these assumptions we repeat the experiments with W precursor while keeping in mind the much lower residence time suggested from literature and confirmed in section 3.2.9. Figure 58 gives the according results which immediately show a widely constant VGR by the black squares. Also the chemical composition is widely constant which strongly suggests a stable working regime independently on the deposit height. This is in agreement with the low residence times and short diffusion lengths for W precursor and further suggests a comparable low thermal influence. Again, this precursor turns out to be beneficial compared to Pt due to the absence of regime changes during growth leading to more controllable fabrication conditions.

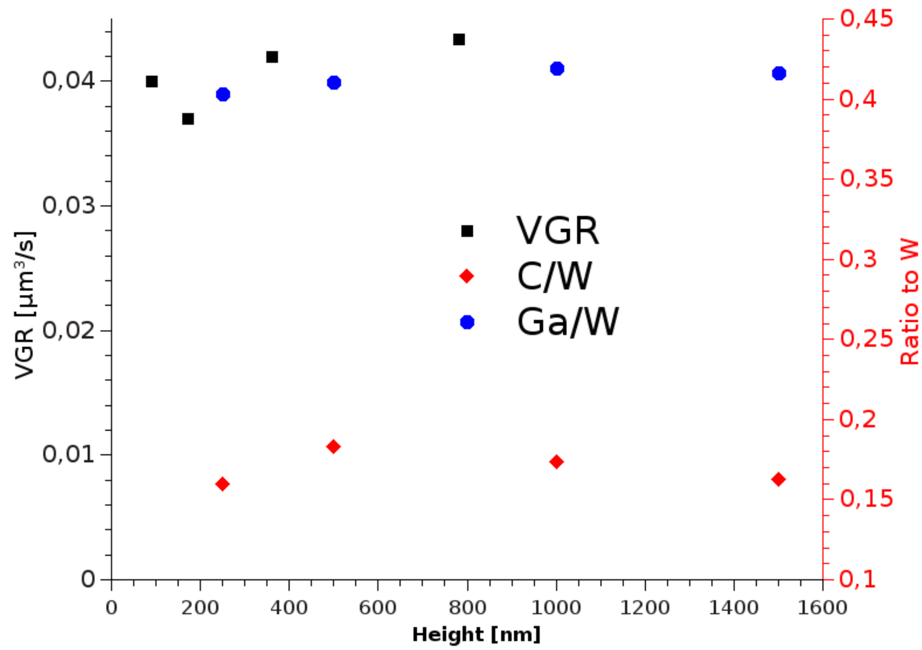

Figure 58: VGR (black, left) for W precursor deposits in dependency on the structure heights at constant footprints. The red and blue scatters give the EDX based peak ratios for C and Ga with respect to W during the growth, respectively.

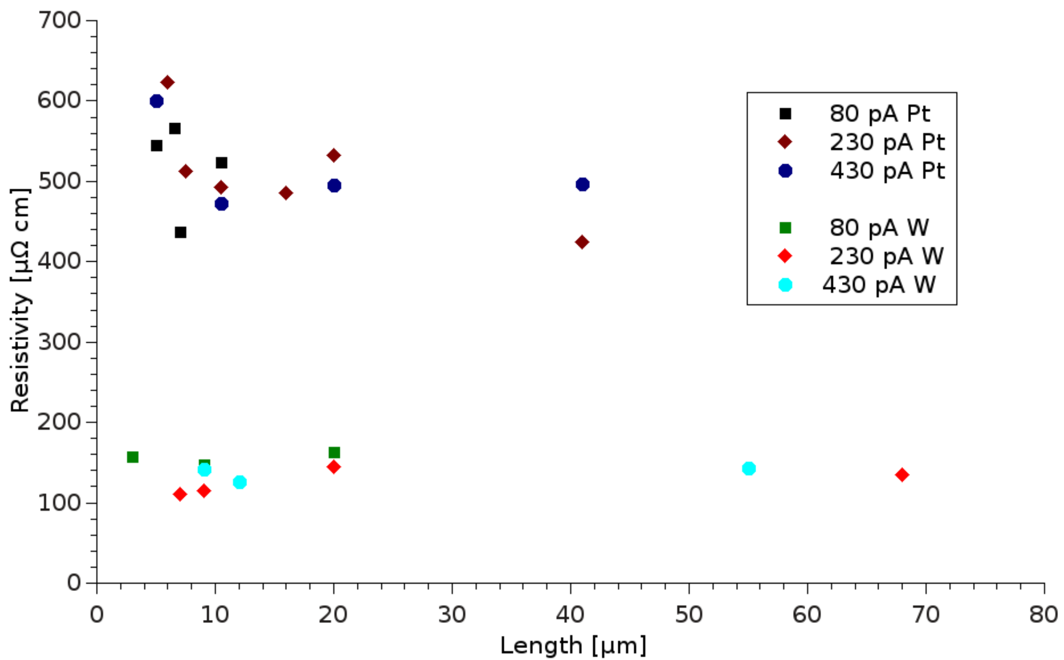

Figure 59: resistivities in dependency of the deposit lengths for different beam currents and precursor (see legend). All deposits have been fabricated at optimized DTs.

Consequently, these findings suggest that for very long replenishment times, Pt should change their behavior while W should remain stable. The enhanced reload time can also be established via longer deposits which also is relevant for technical aspects. Therefore, we compared resistivities for different lengths which indeed revealed widely constant values for W as shown in Figure 59. In contrast, Pt precursor revealed the expected behavior with initially decaying and then more stable values as evident in the same figure. To give further proof for the abovementioned statements Figure 60 shows a 4 µm long connection where about roughly 50 % of the Pt connection (a) is affected by the RT related disruption effects based on the very bad replenishment situation. W deposits, although thinner due to the lower VGR, do not show any signs of lateral disruption which further confirms a widely constant working regime even for short connections.

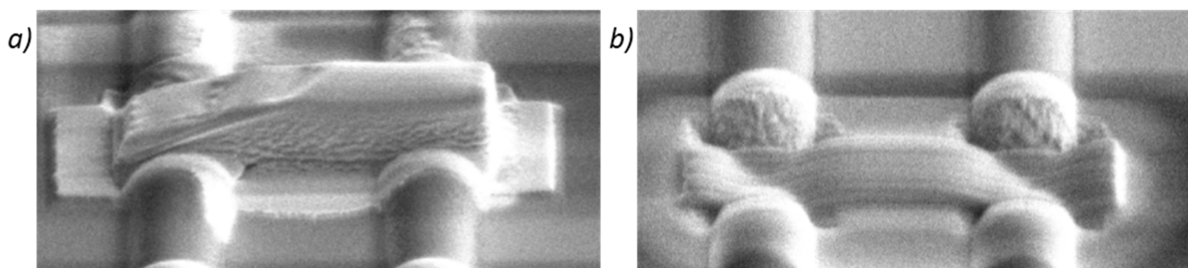

Figure 60: direct comparison of a 4 µm long Pt (a) and W connection (b) fabricated at identical TETs. While the volume growth efficiency for W is much lower, the deposit itself is much more homogeneous which indicates a widely stable working regime in consistency with electric and VGR results presented in this chapter.

3.2.11 Internal Structure and Chemistry of Pt and W Based Deposits

To get a structural and chemical insight in selected Pt and W based deposits, transmission electron microscopy (**TEM**) investigations were gratefully carried out by DI Angelina Orthacker. For that, an FEI Tecnai F20 operated at 200 kV, equipped with a Gatan Tridiem post column imaging filter and a Bruker Si(Li) energy dispersive X-ray detector was used. Initial preparation was done via FIB processing and fixation on a Cu Omnigrid followed by low energy ion milling using a Fishione Nanomill system. TEM bright field images were acquired via an UltraScan camera integrated in the GIF system. Scanning transmission electron microscopy (**STEM**) investigations were performed with a camera length of 100 mm. STEM images were acquired via high angle annular dark field (**HAADF**) detector. For analytical purposes Spectrum Image line scans were performed, which contained an EDX spectrum and an electron energy loss spectroscopy (**EELS**) spectrum in every single pixel. The platinum signal distribution was gained by mapping the Pt-M Peak from the EDX spectrum. The Carbon signal was mapped from the EELS spectrum after background subtraction.

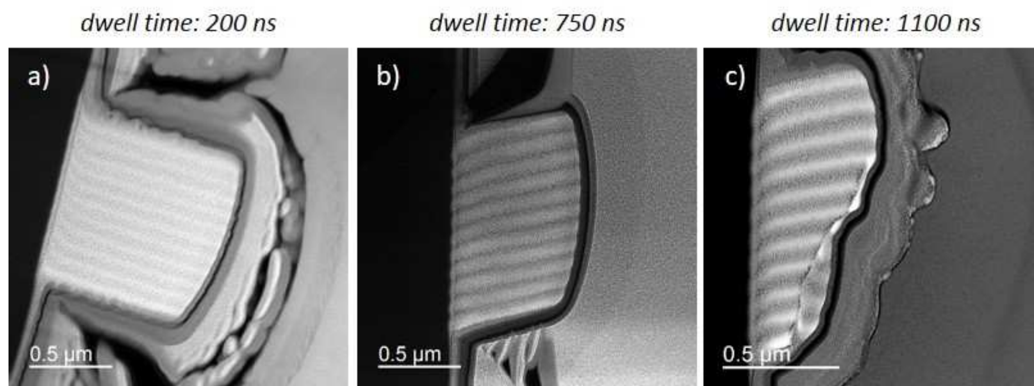

Figure 61: direct comparison of Pt based FIBAD deposits using dwell times of 200 ns (a), 750 ns (b), and 1100 ns (c) using STEM imaging. The dark left parts are the substrates while the striped regions indicate the deposits of interest.

STEM overview imaging revealed a surprising result as shown in Figure 61. Independently on the used dwell times, vertical stripes have been found for Pt based deposits. A closer look on the cover layers on top of the deposits does not reveal such structures (very clear in (b)) which allows to rule out a preparation artefact. Direct measurements of the distance between neighboured dark columns revealed 95 nm, which exactly equals the used point pitch during fabrication. Before an interpretation can be done, chemical line scan analyses have been done as representatively shown in Figure 62.

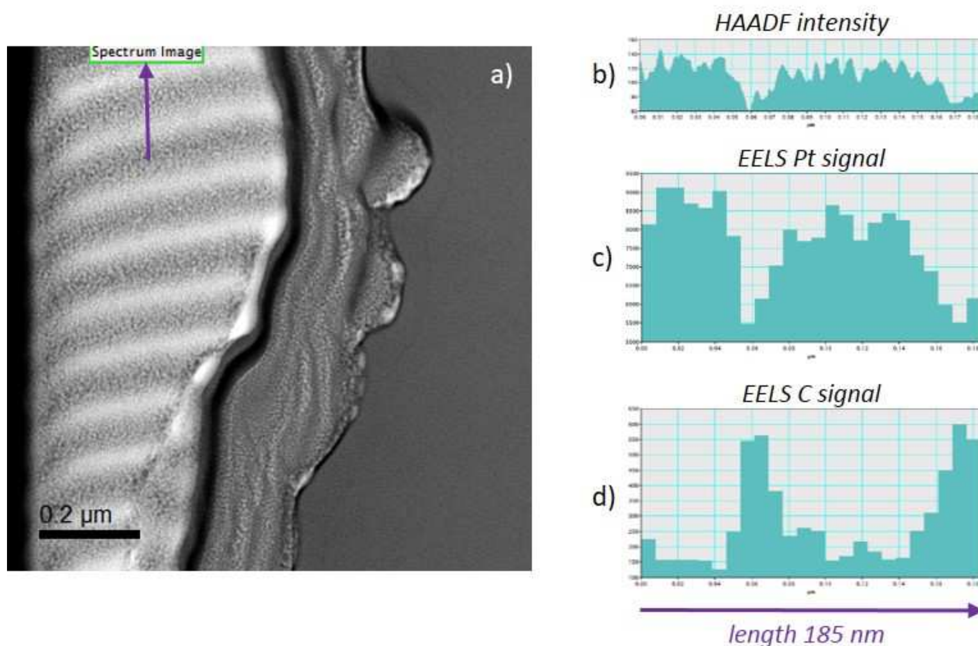

Figure 62: STEM survey image of Pt based FIBAD deposit using 1100 ns dwell time. The purple arrow indicates the line scan which allows laterally resolved information about HAADF intensities (b), the Pt content (c) and the C content (d).

As evident, STEM based line scan analyses of the HAADF intensity (b) as well as the Pt (c) and C (d) contents, the dark column indicates a much higher Pt metal content compared to the bright parts in

between. Together with the coinciding distances concerning the pixel distances, these results allow the conclusion that high ion beam densities at the beam centers induce higher metal contents by improved dissociation rates which, most likely, is thermally assisted due to the high local temperatures. Keeping in mind that the beam is spaced equally in X and Y directions during patterning it follows that in reality the deposits contain isolated columns according to the patterning points. This prevents a direct comparison between different TEM lamellas shown in Figure 61 as the results strongly depends on the cross-cut position. In worst case, the lamella could be taken from areas in between columns which would not reveal any striped patterns. A closer look to the internal structure via high-resolution TEM (**HR-TEM**) has been done as representatively shown in Figure 63 for the 750 ns deposit. First the investigations focused on the transition between dark and bright areas as indicated in (a) and shown in (b). Multiple measurements revealed two main results: ***1)*** typical Pt grain sizes of (5±1) nm widely remain the same, independently on the region (dark vs. bright); and ***2)*** the grain-to-grain distances are clearly reduced in the dark regions. By that, the assumption is further supported that the ion beam profile is reflected in the local chemistry of Pt based FIBAD deposits leading to vertical, columnar features at the patterning points.

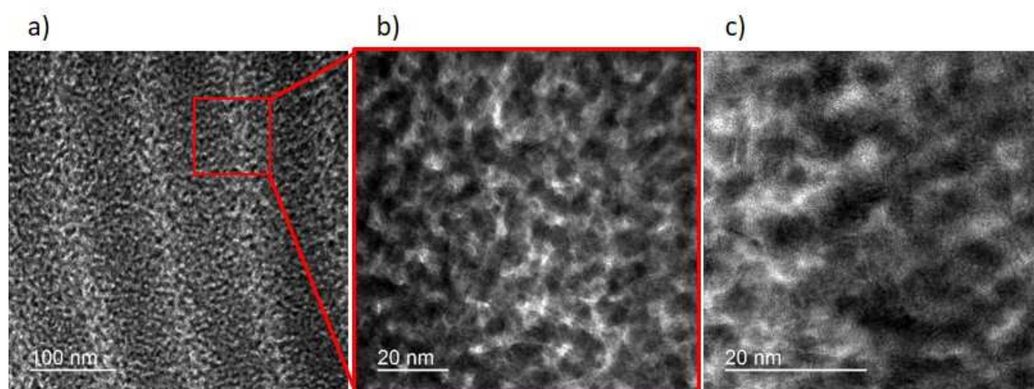

Figure 63: HR-TEM images of a 750 ns Pt deposit (shown in Figure 61 (b)) with increasing magnifications. (b) gives a closer look to a dark-bright transition as indicated in (a) which reveals larger grain-to-grain distances while their sizes are similar. HR imaging in (c) clearly reveals the crystalline features for Pt crystals as expected.

Finally, a direct comparison between Pt and W based deposits have been done. For that, deposits with ideal DTs of 750 ns and 25 ns for Pt and W (sections 3.2.5 and 3.2.9), respectively, have been directly compared. As evident from Figure 64 (a), the deposit does not show any striped features in contrast to Pt deposits shown in Figure 61. HR-TEM images (b) further confirms this observation and also do not reveal any nano-crystalline composition but distinct atomic features by the small dark spots. According FFT analyses (inset in b) further confirms a widely amorphous inner structure of W based FIBAD deposits. This can be explained by the short residence times of W precursor which prevents massive variation in the inner structures.

In conclusion it can be stated that W deposits reveal spatially homogeneous fully amorphous inner composition. In contrast, Pt based deposits reveal vertical columns in accordance with individual patterning points during processing. These columns have much lower carbon contents leading to closer spatial packing of Pt nano-crystals. The origin might be found in the very high ion / electron densities at the beam centers which lead to high dissociation further supported by thermal evaporation of carbon due to the high local temperatures.

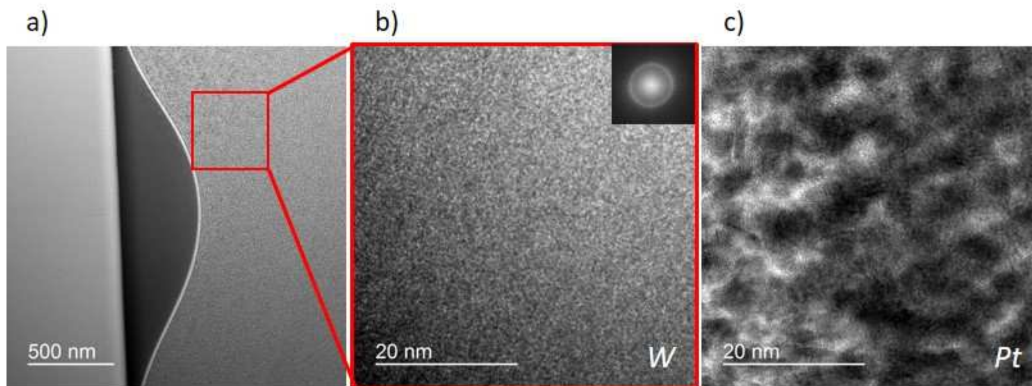

Figure 64: STEM overview of a W based FIBAD deposit (a) revealing an entirely homogeneous inner structure. (b) shows a HR-TEM image of a W deposit in direct comparison to a Pt deposit (c) which reveal neither striped features nor nano-crystalline composition. The latter is further confirmed by a FFT analyses as shown by the inset which does not reveal any indication of distinct reflexes.

3.2.12 Final Comparison between Pt and W

Regarding the efficiency for connections one can say, that W is the better choice in all ranks. Higher efficiency, i.e. to deposit a connection with the lowest achievable resistance with a certain TET, as shown in Figure 65, where both precursors are directly compared regarding their necessary TET to build a connection with 100 Ω and length of 20 µm, at different beam currents. One can clearly see that connections with the desired resistance can be build 2 times faster with W at all beam currents, although Pt is characterized by a much higher VGR. Furthermore tungsten shows less sensitivity to patterning arrangement related effects, and far less overspray, as has been shown for an example in Figure 60. Nevertheless, if one wants to build an additional high resistance in the circuit, Pt might be the better choice. Due to the higher resistivity compared to W, resistors could be built in the same manner as W connections, the current density would be due to the higher volume significantly lower, thus the edited circuit would be less prone to electro-migration.

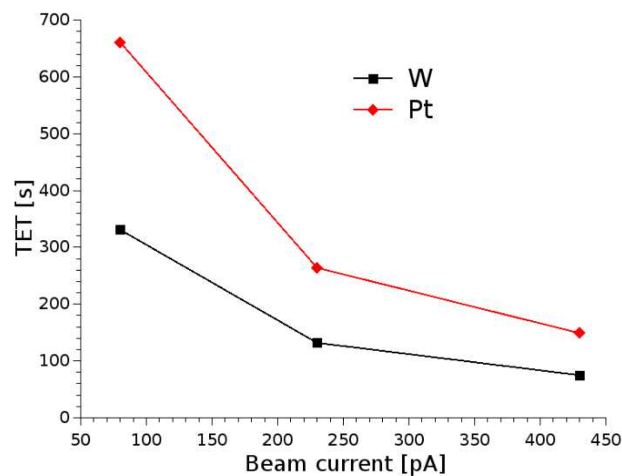

Figure 65: a comparison between W (black squares) and Pt (red diamonds) of the necessary TET to achieve a 20 µm long connection with a total resistance of 100 Ω for various beam currents.

3.2.13 Uncertainty

So far the results have shown remarkable and also surprisingly good predictability of the connections, which can be mostly attributed to the relatively large dimensions of the target regime. Nevertheless, a short section is dedicated to the influence of some side effects on the functionality.

In general, a reproducibility of the resistance measurements within 5 rel.% was achieved for both precursors, while depositing connections with the same parameters. To investigate further factors one 20 µm long connection was deposited in the beam center, no beam shift applied using optimal parameters, a TET of 400 s at a beam current of 230 pA for Pt and W precursor, which were turned on 2 minutes before patterning. For each of the listed factors another connection was deposited under differing conditions and compared.

Changing the angle of the pattern relatively to the GIS by 90° would result in a resistance of 228 Ω compared to 235 Ω for Pt and 57 Ω compared to 59 Ω for W. Thus in both cases a decrease in resistance of about 3 % is observed. This is a further confirmation of the results already discussed in section 3.1.4, which showed that due to the alignment of the pattern relative to the GIS nozzle shadowing effects can occur. Hence it is in general more favorable to align the pattern with the slow scan axis parallel to the GIS nozzle axis.

Shifting the beam center 50 µm further away from the nozzle would result in a resistance of 230 Ω compared to 235 Ω for Pt and 60 Ω compared to 59 Ω for W. The lower resistance for Pt might be accountable to a worse replenishment situation, resulting in a higher Ga incorporation. For W the shift further away from the nozzle seems also to result in a worse replenishment situation, hence increasing the resistance.

If GIS and FIB would be turned on simultaneously, without any precursor coverage before, the resistance would be 1 Ω and 4 Ω higher, for Pt and W respectively. This effect seems to be not as strong for Pt as for W, which might be explained by the fact, that for Pt the initial layers of the deposits have a higher resistivity (see section 3.2.10), due to an increased replenishment for the initial layers, thus these layers are not contributing much to the conductivity of the connection. Contrary for W deposits one can see a relatively higher increase in resistance, because already initial layers contribute to the conductivity.

Measuring the resistance at certain times after deposition showed a total increase of about 1 % of the deposit for W and Pt each, after 5 days, and after that no significant further increase. The highest change in resistance was observed directly after deposition.

As summary, we can state that an overall uncertainty of about 10 % is achieved. It should be again emphasized that this is actually a remarkable result regarding the reproducibility, which can be mostly attributed to the relatively large size of the deposits, since otherwise strongly contributing effects on the nanoscale are not significantly influencing the deposition process.

3.2.14 Functionality Summary

This section was dedicated to the major questions of this thesis, which not only was to find the optimal parameter set for deposition, thus increasing the efficiency, but also to provide a deep understanding of the underlying processes which finally allow a dedicated predictability. With the obtained results it

was possible to point out that for Pt deposits a clear relation between DT and RT exists (section 3.2.5) and dependent on the base area the optimal DT can be predicted for several beam currents. The reason for enhanced efficiency in this case is an increased incorporation of Ga, which was revealed by means of EDX measurements. For W deposits the optimal DT is technically limited by the DBM itself to 25 ns. Whereas in this case the enhanced efficiency can be regarded to a superior VGR at lower DT (section 3.2.9). Chemical composition and resistivities with respect to the length seem to be widely constant for W precursors and slightly varying for Pt precursor. This indicates widely constant regime conditions at optimal DTs for the former and slightly, but not critically, varying situations even at ideal DTs for the latter precursor (section 3.2.10). After optimization of the DT, other parameter seem to bring no further increase to the overall efficiency (section 3.2.6 and 3.2.7) which indicate a real optimization towards the intrinsic limits for the given technical setup. The uncertainty, due to some inevitable side effects, for the efficiency of the connections was estimated to be within a range of 10 % of the final resistance, thus resulting in a remarkable high reproducibility for the connections.

3.3 Easy to Use Guideline and Spreadsheets

As explained in the introduction the intention of this study was two-fold: 1) understanding the fundamental effects during FIBAD which then leads to 2) derive guidelines for a most efficient, reproducible and predictable application in the field of CE. While the former was intensively discussed in the previous chapter, the latter is now summarized in four diagrams as the main outcome for the ams AG. Before that, however, a few boundary conditions have to be fulfilled:

- In general this guideline can be used for connections with a width between 1 µm and 5 µm and a height between 0.5 µm and 3 µm.
- If possible, align the pattern for a deposit rectangular to the nozzle main axis in the beam center, with no applied beam shift. If this is not possible, the final resistance of the connection will be increased.
- If possible avoid proximity effects by depositing structures at least 5 µm apart from each other. If this is not possible, be aware that the final resistance will have an increased value.
- To obtain best results the gas flux should be started before patterning.
- For deposition of simple connections use the W precursor. For deposition of resistors use the Pt precursor.
- The final resistance of a connection can be determined from the diagrams for Pt and W for short and long connections (Figure 66 to Figure 67). For each of these diagrams the x axis represents the length, the y axis represents the total exposure time. In the diagrams for short and long connections are 3 and 2 sectors, respectively, which mark the used beam currents: 80 pA, 230 pA and 430 pA. For each current 3 curves are represented, a solid line for a value of 2.5 Ω/µm for Pt or 1 Ω /µm for W, a dashed line for a value of 5 Ω /µm for Pt or 2.5 Ω /µm for W, a dotted line for a value of 10 Ω /µm for Pt or 5 Ω /µm for W.
- In addition to that the contact resistance per contact for Pt is about 9 Ω (for 1 x 1 µm²).
- The uncertainty will be within a range of 10 % of the final value.

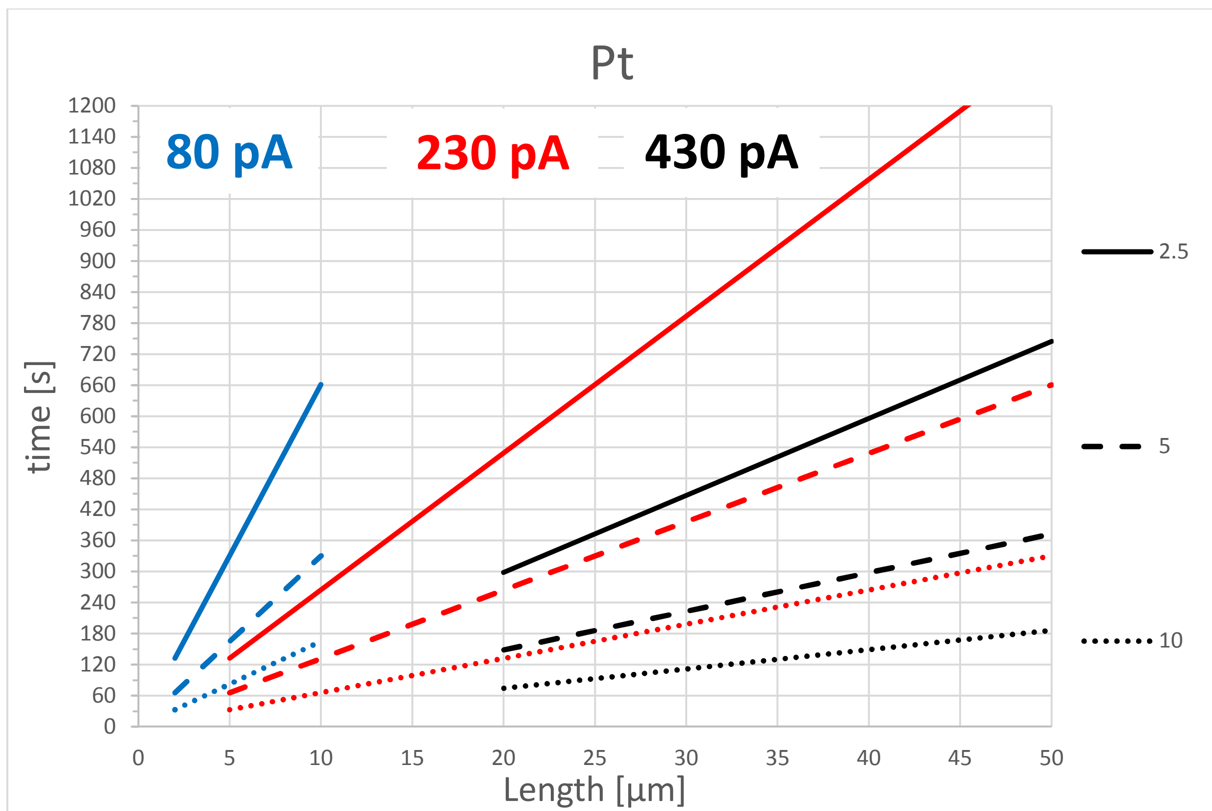

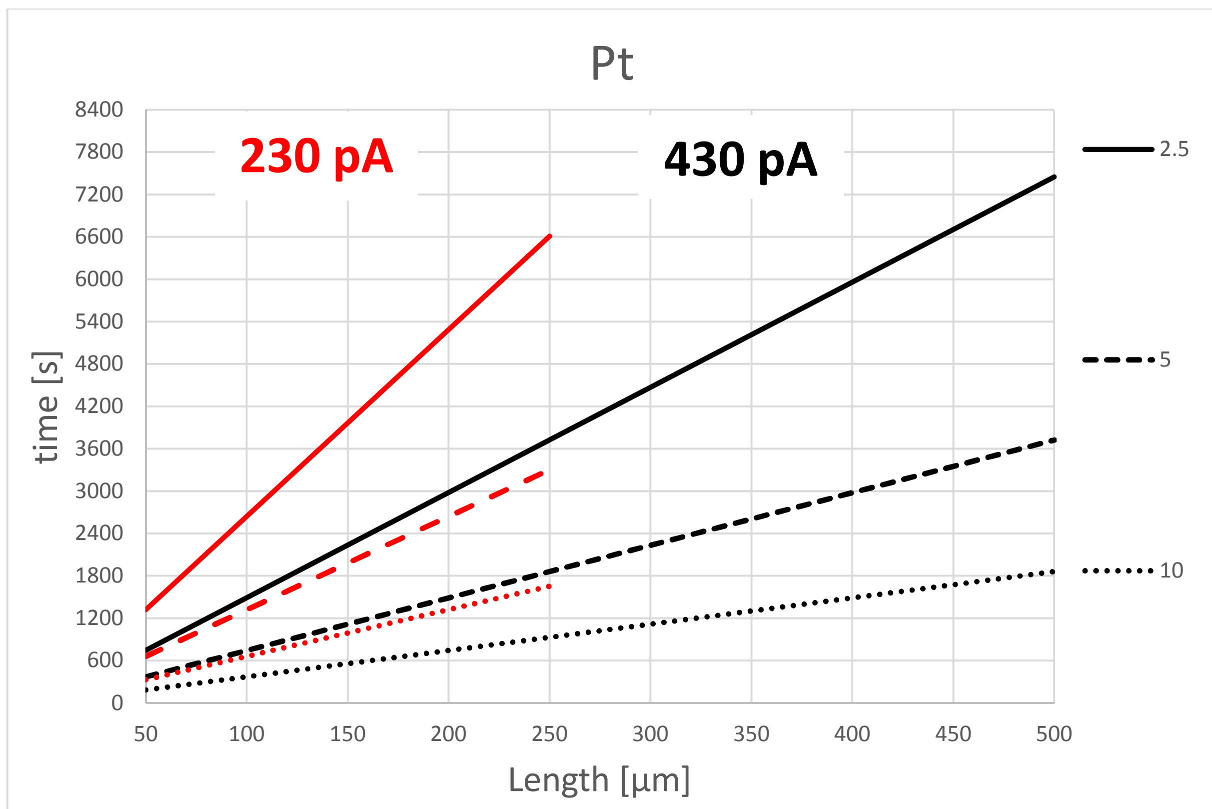

Figure 66: The required total exposure time (y-axis) to deposit Pt connections with a certain length (x-axis) for the beam current apertures 80 pA (blue lines), 230 pA (red lines) and 430 pA (black lines). The different line types represent a resistance per length of 2.5 Ω/µm (solid), 5 Ω/µm (dashed) and 10 Ω/µm (dotted). The upper diagram accounts for short connections, while the lower diagram represents medium and long connections up to 500 µm.

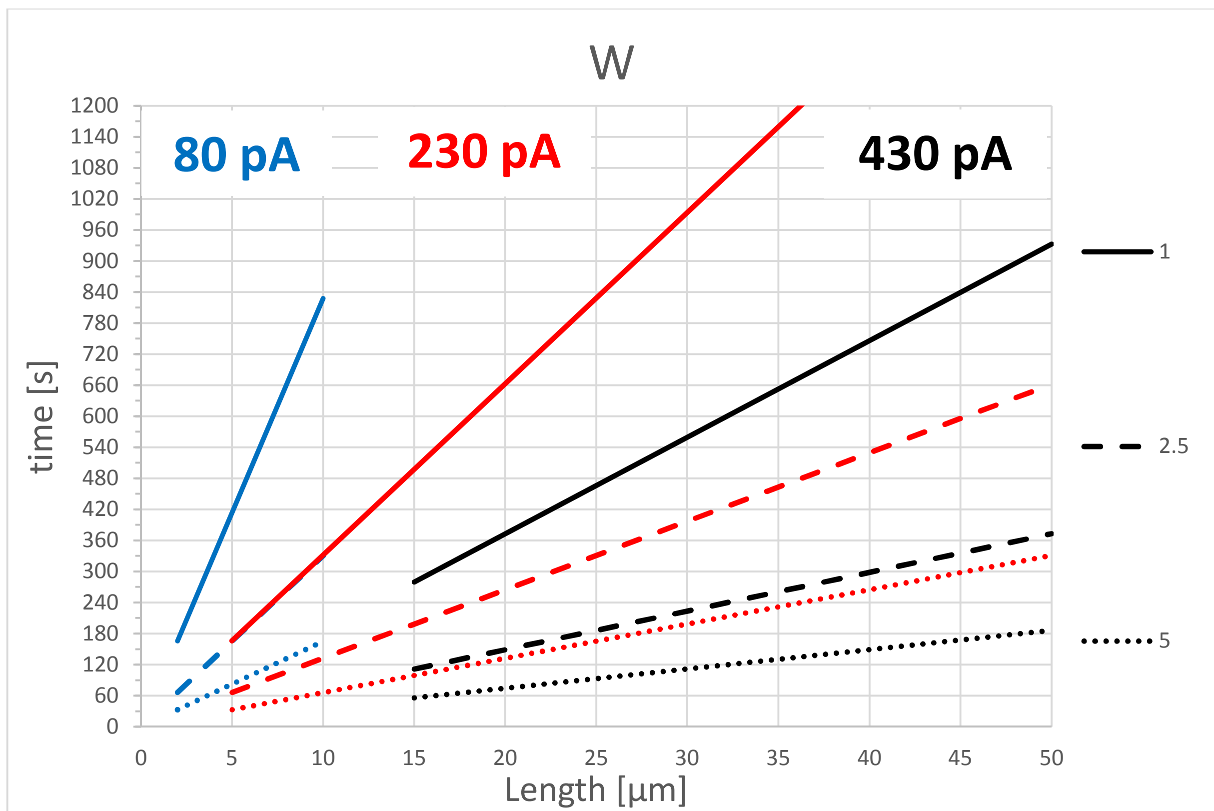

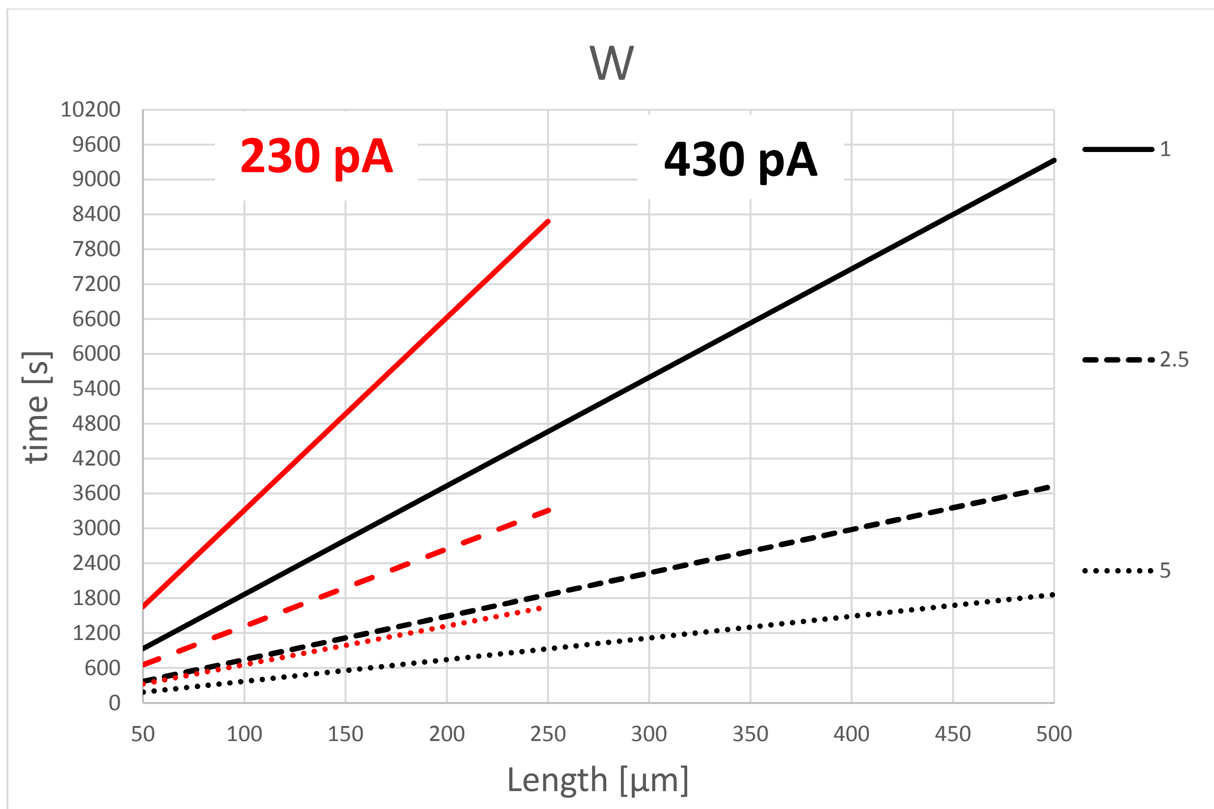

Figure 67: The required total exposure time (y-axis) to deposit W connections with a certain length (x-axis) for the beam current apertures 80 pA (blue lines), 230 pA (red lines) and 430 pA (black lines). The different line types represent a resistance per length of 2.5 Ω/µm (solid), 5 Ω/µm (dashed) and 10 Ω/µm (dotted). The upper diagram accounts for short connections, while the lower diagram represents medium and long connections up to 500 µm.

For completeness we have provided a memory device to this thesis which contains some calculation sheets which generate the above shown graphs. As mentioned in section 3.2.5, it is also possible to access the main parameters c_1 and c_2 via two simple resistivity vs. DT sweep for one beam current. These values can then be accessed by equation 5.

For finding the empirical constants c_1 and c_2, and creating a new DT_{opt} curve for Pt:

- The empirical parameters for the DT_{opt} curve can be obtained by following the steps in spreadsheet 5.1. In order to do so the whole table should be copy and paste into a new excel spreadsheet.
- Work at one particular beam current. Look up the beam diameter of this beam current in the deposition properties in the user interface.
- Write the value of the beam diameter in Cell B8, using the unit nm.
- Set the values for overlap to -150 % in the user interface, defocus and blur to 0.
- Make 2 DT sweeps with a measurement layout as given in section 3.2.4.2 at different base areas, and find the DT with the lowest resistance, which is referred to as DT_opt, while keeping the TET constant.
- For the 1st measurement write the value of the base area into cell B19, using the unit µm². Write the value of DT_opt into cell B20, using the units ns.
- For the 2nd measurement write the value of the base area into cell B25, using the unit µm². Write the value of DT_opt into cell B26, using the units ns.
- The empirical parameters c1 and c2 (as in equation 5) are now given in cell B30 and B31, respectively.

However, one should keep two things in mind.

- First of all the uncertainty of this curve will be very high. Thus to improve the accuracy of the curve and obtain more reliable results one should make several DT sweeps and interpolate the results of several DT_{opt} at those base areas.
- Furthermore, although not found in this work, there will be some limitations, e.g. if one uses too small base areas, too small TETs or too high beam currents. Thus one should work within the frame of the beam currents which were investigated in this thesis (i.e. 80 pA – 430 pA).

For updating the diagrams:

- The diagrams can be updated, if the system changes simply by updating the information and follow the steps in the spreadsheet (section 5.2). In order to do so the whole table should be copy and paste into an excel spreadsheet.
- To change the current values update the new values in B13 B15 and B17.
- To change the VGR update the value in B19, to change the resistivity update the value in B21.
- To change the values of the line representing certain Ω/µm, update the new values in A26 to A28.

3.4 High Current Induced Functionality Tuning

In this final section we present the results of some experiments, at which a high current density applied to the deposited structures led to a significant change in resistance. It should be emphasized that these experiments, undertaken out of curiosity, are just briefly overviewing the occurring effects and for a full understanding of the underlying mechanisms more dedicated investigations would be necessary but nevertheless act as basis for interesting effects which might be of future relevance.

Experiments were carried out using the first measurement layout, which is discussed in section 3.2.4.1. The connections were deposited using a beam current of 40 pA, a DT of 200 ns, OL of -150 %, and the GIS was opened 2 minutes prior to deposition to ensure similar coverage for all deposits. The number of loops was varied, hence deposits with different heights were investigated.

For the investigations of the electrical properties the voltage was measured along a path of a 4 µm in the middle of the deposit, while the current, applied at the ends of the deposit, would change like a triangular function. At first steadily increasing from zero up to a certain limit then decreasing with the same ramp to the negative limit, followed again by an increase in current. Such a sweep would be repeated several times with the same upper and lower limits. After a few cycles the current limits would be increased. With this experiment it is possible to distinguish between reversible and irreversible changes within the deposit, since the voltage is measured for several cycles. Additionally, it is possible to determine the cause of physical changes in the deposit, because the direction of the current flow is reversed in one cycle one can tell apart temperature induced effects and those which are caused by ion- or electromigration. The former results in a shift towards the same direction regardless of the direction of the applied current, while for the latter the resistance change depends on the direction of the applied current.

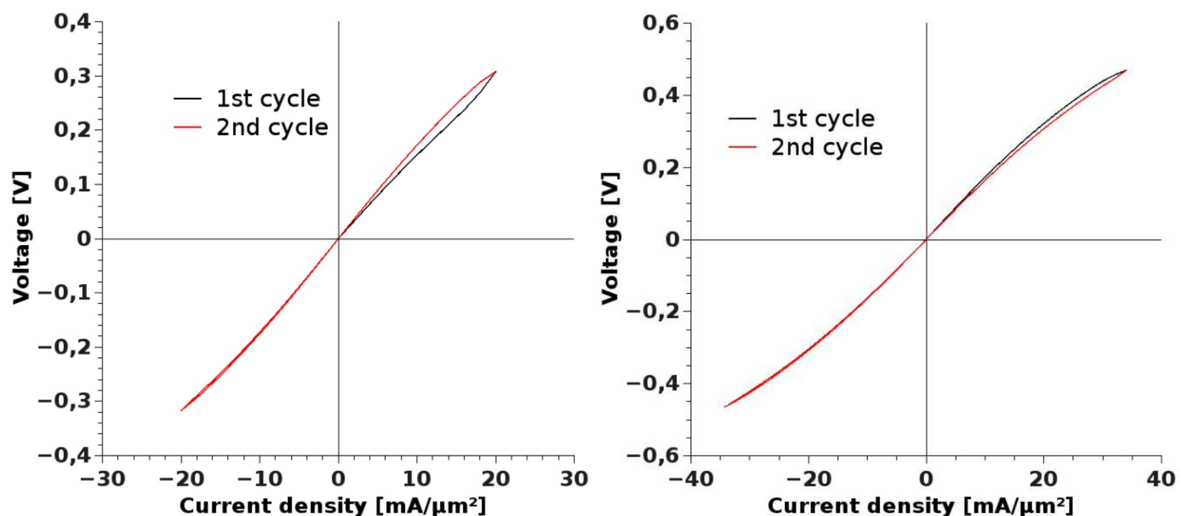

Figure 68: I-V curves with high current densities reveal a permanent non reversible change of the resistance, which is indicated by different curves of consecutive measurements. For different current density limits a change towards different directions was observed.

The results show, that for current densities of up to ~ 10 mA per µm² the I-V curve exhibits linear behavior (Figure 68, left). Above this value the I-V curve becomes non-linear and certain effects take place resulting in a shift of the total resistance (Figure 68, left). At about 20 mA per µm² an increase and at about 30 mA per µm² a decrease is observed. The first increase of the current is represented by the black curve, while subsequent cycles are follow the red curve, which represents a different resistance.

Although the resistance shifts towards different directions, both these effects show similar characteristics. The change is permanent, that is to say that measurements which were conducted afterwards with the same or a lower current limit revealed the same resistance. They are non-reversible, i.e. changing the polarization of the applied current will not reverse the change in resistance, but even further increase/decrease it. Also the second effect cannot be reversed by the first, i.e. applying a current density of 30 mA per µm² and then 20 mA per µm² will decrease the resistance but nothing changed during the second step.

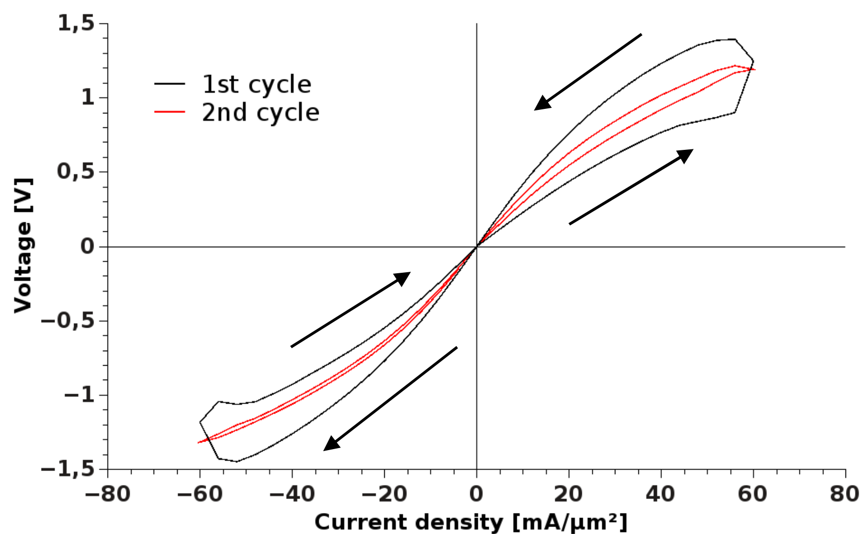

Figure 69: an I-V curve with high current density reveal a reversible change of the resistance depending on the direction (black arrows) of the current.

Due to the indifference regarding the polarization and the non-reversibility we assume that the resistance changes are caused by a temperature induced structural change of the deposit, since the temperature increases with increasing current density. Such a process might be comparable to some kind of annealing of the structure, which might be a consequence of the highly inhomogeneous distribution of Ga and Pt within the deposit. However, it was not yet possible to explain or determine why exactly the resistance first increases and then reduces. To clarify this issue more sophisticated experiments are necessary. So far we can only say that since the measurements were performed with a classical 4 point measurement it is unlikely that the hysteresis is somehow related to the interface between the metal connections of the IC and the deposited structures. Visual investigations using the SEM also didn't reveal any change on the surface of the deposit.

If the current density would be even further increased to about 55 mA per µm² another effect occurs. This one is very different to the previously discussed ones and can be seen in Figure 69. As the figure reveals the most significant difference is that the change in resistance seems to be reversible in this regime. The positive branch of the 1st current sweep (black curve) led to an increase of the resistance, while the negative branch of the first cycle led to a decrease. The second cycle (red curve) showed the same behavior, though not as strong as the first one. The sweep direction is indicated by the black arrows in the figure. However the reversibility due to the changing polarization points out that this effect is caused by electro/ion migration, since the force of the electric field associated with the high current density has a distinguished direction. Though it should be emphasized that due to the measurement layout not the whole deposit was investigated, but only the path between the two inner metal connects. We assume that the underlying mechanism can be explained by the following process, which is depictured in Figure 70. At which the amount of high conducting material (Pt and Ga) is indicated by the grey background. In the beginning (1) the Pt and Ga is about equally distributed, considering the scale of the whole deposit. Then (2) a high electric field (blue arrow) leads to electro/ion migration, subsequently leading to a reduction of Pt or Ga in the middle region which is indicated by the red lines, hence the resistance increases. As the polarization is reversed the ions migrated towards the other direction (3), subsequently leading to an accumulation in the middle region at first, resulting in a decrease of the resistance. Therefore, if the current would be applied for a too long time the Pt and Ga would migrate through the middle region leading to an increase of the resistance at one point just as like in the second step. Electro/ion migration was also confirmed by visual investigations, which clearly showed a change of the structure of the deposit.

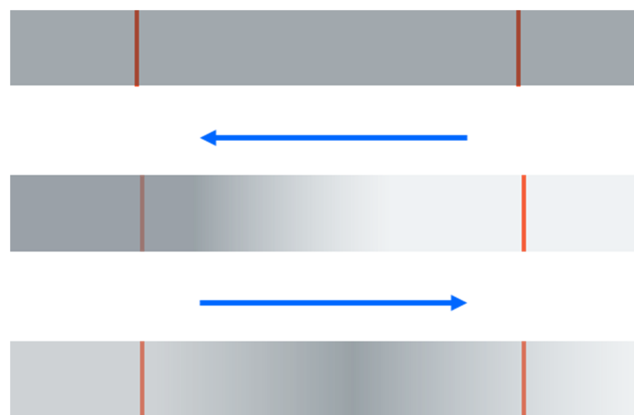

Figure 70: a simple explanation for the underlying mechanism of the resistance change, which is reversible. The voltage was measured for the path between the two red lines. Areas low resistance are indicated by a higher value of grey, the direction of the electric field is indicated by the blue arrow.

The experiments done in this section show that principally focused ion beam deposited Pt structures might be used as a memory unit, at which a high current density pulse would change the resistance, which would be equal to switching between certain states. However, for this purpose much smaller dimensions of the deposits would be necessary. Furthermore various aspects would have to be clarified, i.e. how much current density and how much time is needed to switch the resistance, also how many cycles would such a structure withstand and finally a layout embedding multiple elements

would have to be found. If all these questions can be answered this principle would certainly be one step closer to an IC completely manufactured by FIBAD/FEBID.

4 Summary and Outlook

This thesis focused on the functionality of focused ion beam assisted deposited (FIBAD) structures, fabricated via the organometallic precursors $MeCpPt^{IV}Me_3$ and $W(CH)_6$, for the application as conductive paths for circuit editing. Key result of this study was the finding of a scaling law relating the optimized pixel dwell times, with respect to lowest achievable resistances for fixed total exposure times, including the main patterning parameters beam current, beam overlap and the number of patterning points which are equivalent to the structure footprints. In summary, this thesis successfully demonstrates a FIBAD process window which allows a predictability of electric resistances with an accuracy of more than 90 %. At the same time, these parameters provide fastest processing at the intrinsic limit of FIBAD. Thus, this study provides the framework for highly efficient and defined fabrication of electric connections in the field of circuit editing as an essential part in research and development.

The study started with an investigation of the volume growth rate (VGR) during fabrication of Pt based deposits and its chemical composition accessed via scanning electron microscopy (SEM) and energy dispersive X-ray measurements (EDX). Due to the systematic patterning arrangement certain side effects became evident. In particular, the investigations revealed a strong variation of VGR's and chemical composition in dependence on the distance to the gas injection (GIS) nozzle along its main axis. This could successfully be assigned to the highly inhomogeneous precursor gas flux leading to position dependent replenishment effects of the precursor molecules. In addition to these well-known effects it was possible to experimentally confirm a geometry related effect, denoted as pad reflection, which occurs if structures are built too close together (< 5 µm) as predicted by simulations in the past. By that a set of design rules could successfully be derived which strongly increased the reproducibility.

To obtain a deeper understanding of its material functionalities, electric 4-point measurements were performed *in-situ*. The aim was to find the set of parameters for pixel dwell time (DT), pixel overlap (OL), beam defocus and ion beam currents to minimize the total resistance of the deposits for lowest total exposure time to maximize the throughput. It could be shown, that the main driving force for varying results relies on the local precursor working regime which describes the ratio between local precursor molecules and potentially dissociating particles. The strongest effect was found during DT sweeps where two intermixing trends were identified: ***1)*** the electric resistances decreased with longer beam pulses; and ***2)*** the VGRs as well as the shape fidelity strongly decreased with longer beam pulses. As the latter influences the volume and by that the resistivity straightforward increase of DTs were identified as an impossible route towards ideal results. However, systematic investigations revealed a well pronounced process window for intermediated beam pulses where lowest resistivities at stable shape fidelities are provided. Further investigations of this process window in dependency on beam overlap, beam focus and ion beam currents successfully allowed to derive a semi-empiric mathematical model which allows prediction of ideal process parameters with sub 10% variation of the final resistivities range for FIBAD processing of Pt based structures. Considering the internal structure of Pt-C-Ga deposits a surprising result was found via transmission electron microscopy (TEM).

It could be shown that the structure reveals vertical columns with lower carbon contents and slightly larger Pt nano-crystals in agreement with the beam center positions. This is attributed to the ion beam profile where higher ion densities at the center lead to higher dissociation and temperature assisted evaporation of carbonaceous contents.

Repeating the key experiments for tungsten based precursor, basically revealed the same dwell time dependency, however, for much smaller absolute values. This in turn, is consistent with previous studies which revealed much shorter residence times of the precursor molecules on the surface which ultimately shifts the ideal working regime towards shorter pulse durations. Apart from that, the above mentioned model also holds for this precursor type and allows the predication of electric resistances with an accuracy higher than 90 %. In contrast to Pt based materials, W-C-Ga deposits did not reveal any columnar effects via TEM. This is attributed to the different precursor chemistry and the fact that W precursor can be dissociated much more efficiently. The latter effect of a lower carbon content is also reflected by the absolute resistivity of W based materials which is almost one order of magnitude lower than for Pt materials.

The above mentioned scaling laws, derived from the result for both precursor, were finally adapted into a strategy map for the fast selection of deposition time for different deposit lengths with different target resistances. The elegant aspect of this model is that it only requires one dwell time sweep for each ion beam current and precursor material of interest to calibrate the mathematical model in the background. That makes this model applicable on different machines and technical GIS setups which points out the practical value of this study.

By that it becomes evident that this master thesis spans the bow from fundamental towards practical aspects concerning FIBAD based fabrication of conductive Pt and W microstructures. While the former enabled a deep insight in working regime variations, its origins and consequences, the latter provide the framework for a highly efficient application in the field of circuit editing as essential part in science and technology.

5 Appendix

5.1 Appendix 1 – Spreadsheet for calculating the empirical parameters

Instructions for determining the empirical parameters

Choose a certain beam current for the investigation
For this certain beam current look up the beam diameter d_B
within the user interface
Type the obtained value into cell B7

d_B =	38

Set the overlap to -150 % in the user interface
set the defocus and blur to 0

Make 2 DT sweeps at different base areas of the connection

Make the 1st DT variation, type the base area [µm] in cell B17
Write the DT [ns] with the lowest resistance into cell B19

Base Area:	6
DT_opt:	250

Make the 2nd DT variation, type the base area [µm] in cell A17
Write the DT [ns] with the lowest resistance into cell B19

Base Area:	32
DT_opt:	650

You obtain the following constants for your DT_opt curve:

c_1:	=(B26-B20)/LN(B25/B19)
c_2:	=EXP(B26/B30)/B25*(2.5*B8*0.001)^2

5.2 Appendix 2 – Spreadsheets for updating the diagrams

Instructions for recalculating the curves:

Write the real current values of the ion beam into the colum
"Measured", next to the aperture values
The dose dependent volume growth rate (DVGR) is ESTIMATED from the performed measurements.
The DVGR can be changed in the green framed field next to **DVGR**.
In the cell next to it the uncertainty for the DVGR can be stated
The DVGR can is determined as the deposited Volume (base area times height)
divided by charge (beam current times deposition time).
The resistivity is measured determined by a resistance measurement and the volume.

It can be changed below Resistivity. As well the uncertainty can be changed

Aperture [pA]	Measured [pA]	Uncertainty	Unit
80			pA
------------------------	------------------------	------------------------	
230			pA
------------------------	------------------------	------------------------	
430			pA
------------------------	------------------------	------------------------	
DVGR			**µm³ / (pA s)**
Resistivity			**µΩ cm**

Set the resistance per length (R / L) and calculate their uncertainty.

R / L [Ω/µm]	+ / -	Ω/µm
2.5	=($C$21*0.01/A26+$B$21*0.01*$C$19/$B$19)	
5	=($C$21*0.01/A27+$B$21*0.01*$C$19/$B$19)	
10	=($C$21*0.01/A28+$B$21*0.01*$C$19/$B$19)	

Adjust the Diagrams:	Regime	
Aperture	From	To
=A13	2	50
=A15	2	50
=A17	2	50

Copy the text starting at cell A 77.
Click on View -> Macros -> type in "Create_Diagram" and press the button Create.
Paste in the code and save
Click on View -> Macros -> select "Create_Diagram" and press the button run
Adjust the Diagram as you wish

Create the diagrams:

I_1 R / L 1 =A26&C25
=B21*B32/B19/B13/A26*0.01
=B21*C32/B19/B13/A26*0.01
I_1 R / L 2 =A27&C25
=B21*B32/B19/B13/A27*0.01
=B21*C32/B19/B13/A27*0.01
I_1 R / L 3 =A28&C25
=B21*B32/B19/B13/A28*0.01
=B21*C32/B19/B13/A28*0.01

I_2 R / L 1
=B21*B32/B19/B15/A26*0.01
=B21*C32/B19/B15/A26*0.01
I_2 R / L 2
=B21*B32/B19/B15/A27*0.01
=B21*C32/B19/B15/A27*0.01
I_2 R / L 3
=B21*B32/B19/B15/A28*0.01
=B21*C32/B19/B15/A28*0.01
I_3 R / L 1
=B21*B32/B19/B17/A26*0.01
=B21*C32/B19/B17/A26*0.01
I_3 R / L 2
=B21*B32/B19/B17/A27*0.01
=B21*C32/B19/B17/A27*0.01
I_3 R / L 3
=B21*B32/B19/B17/A28*0.01
=B21*C32/B19/B15/A28*0.01

```
Sub Create_Diagram()
'
' Create_Diagram Macro

    ActiveSheet.Shapes.AddChart2(240, xlXYScatterLinesNoMarkers).Select
    ActiveChart.Parent.Name = "Diagram"

'The Data is imported into the chart


    ActiveChart.SeriesCollection.NewSeries
    ActiveChart.FullSeriesCollection(1).XValues = "=Sheet1!$B$32:$C$32"
    ActiveChart.FullSeriesCollection(1).Values = "=Sheet1!$A$49:$A$50"
    ActiveChart.SeriesCollection.NewSeries
    ActiveChart.FullSeriesCollection(2).XValues = "=Sheet1!$B$32:$C$32"
    ActiveChart.FullSeriesCollection(2).Values = "=Sheet1!$A$52:$A$53"
    ActiveChart.SeriesCollection.NewSeries
    ActiveChart.FullSeriesCollection(3).XValues = "=Sheet1!$B$32:$C$32"
    ActiveChart.FullSeriesCollection(3).Values = "=Sheet1!$A$55:$A$56"
    ActiveChart.SeriesCollection.NewSeries
    ActiveChart.FullSeriesCollection(4).XValues = "=Sheet1!$B$33:$C$33"
    ActiveChart.FullSeriesCollection(4).Values = "=Sheet1!$A$58:$A$59"
    ActiveChart.SeriesCollection.NewSeries
    ActiveChart.FullSeriesCollection(5).XValues = "=Sheet1!$B$33:$C$33"
    ActiveChart.FullSeriesCollection(5).Values = "=Sheet1!$A$61:$A$62"
    ActiveChart.SeriesCollection.NewSeries
    ActiveChart.FullSeriesCollection(6).XValues = "=Sheet1!$B$33:$C$33"
```

```
    ActiveChart.FullSeriesCollection(6).Values = "=Sheet1!$A$64:$A$65"
    ActiveChart.SeriesCollection.NewSeries
    ActiveChart.FullSeriesCollection(7).Name = "=Sheet1!$B$48"
    ActiveChart.FullSeriesCollection(7).XValues = "=Sheet1!$B$34:$C$34"
    ActiveChart.FullSeriesCollection(7).Values = "=Sheet1!$A$67:$A$68"
    ActiveChart.SeriesCollection.NewSeries
    ActiveChart.FullSeriesCollection(8).Name = "=Sheet1!$B$51"
    ActiveChart.FullSeriesCollection(8).XValues = "=Sheet1!$B$34:$C$34"
    ActiveChart.FullSeriesCollection(8).Values = "=Sheet1!$A$70:$A$71"
    ActiveChart.SeriesCollection.NewSeries
    ActiveChart.FullSeriesCollection(9).Name = "=Sheet1!$B$54"
    ActiveChart.FullSeriesCollection(9).XValues = "=Sheet1!$B$34:$C$34"
    ActiveChart.FullSeriesCollection(9).Values = "=Sheet1!$A$73:$A$74"

'Set the axis labels
 With ActiveChart
    .HasTitle = False
    .Axes(xlCategory, xlPrimary).HasTitle = True
    .Axes(xlCategory, xlPrimary).AxisTitle.Characters.Text = "Length [µm]"
    .Axes(xlValue, xlPrimary).HasTitle = True
    .Axes(xlValue, xlPrimary).AxisTitle.Characters.Text = "Time [s]"

    End With

' The line specs are set

    ActiveChart.FullSeriesCollection(1).Select
    With Selection.Format.Line
        .Visible = msoTrue
        .ForeColor.RGB = RGB(0, 0, 255)
        .Transparency = 0
    End With
    ActiveChart.FullSeriesCollection(2).Select
    With Selection.Format.Line
        .Visible = msoTrue
        .ForeColor.RGB = RGB(0, 0, 255)
        .Transparency = 0
        .DashStyle = msoLineDash
    End With
        ActiveChart.FullSeriesCollection(3).Select
    With Selection.Format.Line
        .Visible = msoTrue
        .ForeColor.RGB = RGB(0, 0, 255)
        .Transparency = 0
        .DashStyle = msoLineSysDot
    End With
```

```
    ActiveChart.FullSeriesCollection(4).Select
  With Selection.Format.Line
    .Visible = msoTrue
    .ForeColor.RGB = RGB(255, 0, 0)
    .Transparency = 0
  End With
    ActiveChart.FullSeriesCollection(5).Select
  With Selection.Format.Line
    .Visible = msoTrue
    .ForeColor.RGB = RGB(255, 0, 0)
    .Transparency = 0
    .DashStyle = msoLineDash
  End With
    ActiveChart.FullSeriesCollection(6).Select
  With Selection.Format.Line
    .Visible = msoTrue
    .ForeColor.RGB = RGB(255, 0, 0)
    .Transparency = 0
    .DashStyle = msoLineSysDot
  End With
    ActiveChart.FullSeriesCollection(7).Select
  With Selection.Format.Line
    .Visible = msoTrue
    .ForeColor.RGB = RGB(0, 0, 0)
    .Transparency = 0
  End With
    ActiveChart.FullSeriesCollection(8).Select
  With Selection.Format.Line
    .Visible = msoTrue
    .ForeColor.RGB = RGB(0, 0, 0)
    .Transparency = 0
    .DashStyle = msoLineDash
  End With
    ActiveChart.FullSeriesCollection(9).Select
  With Selection.Format.Line
    .Visible = msoTrue
    .ForeColor.RGB = RGB(0, 0, 0)
    .Transparency = 0
    .DashStyle = msoLineSysDot
  End With

' The Legend is adjusted

  ActiveChart.SetElement (msoElementLegendRight)
  ActiveChart.ChartArea.Select
```

```
For i = 1 To 6
ActiveChart.Legend.Select
ActiveChart.Legend.LegendEntries(1).Select
Selection.Delete
Next i

End Sub
```

References

[1] PRESENT, I. "Cramming more components onto integrated circuits." *Readings in computer architecture* (2000): 56.

[2] Utke Ivo, Stanislav Moshkalev, and Phillip Russel, eds. *Nanofabrication using focused ion and focused electron beams: principles and applications*, Oxford University Press, 2012.

[3] Tao, Tao et al. "Focused ion beam induced deposition of Platinum" Journal of *Vacuum Science & Technology B* 8.6 (1990): 1826-1829.

[4] Langford, R.M., T.-X. Wang, and D. Ozkaya. "Reducing the resistivity of electron and ion beam assisted deposited Pt." *Microelectronic Engineering* 84.5 (2007): 784-788.

[5] Fernandez-Pacheco, A. et al. "Metal-insulator transition in Pt-C nanowires grown by focused-ion-beam-induced deposition." *Physical Review B* 79.17 (2009): 174204.

[6] Geier, Barbara, et al. "Rapid and Highly Compact Purification for Focused Electron Beam Induced Deposits: A Low Temperature Approach Using Electron Stimulated H2O Reactions." *The Journal of Physical Chemistry C* 118.25 (2014): 14009-14016.

[7] ams AG, Tobelbader Straße 30, 8141 Unterpremstätten Styria, Austria

[8] Courtesy of Univ.-Doz. Dipl.-Ing. Dr.techn. Harald Plank, Institute for Electron Microscopy and Nanoanalysis, Graz University of Technology, Austria, 2013.

[9] Mayer, Joachim, et al. "TEM sample preparation and FIB-induced damage." *Mrs Bulletin* 32.05 (2007): 400-407.

[10] Courtesy of Dipl.-Ing. Robert Winkler, Graz Centre of Electron Microscopy, Graz, Austria, 2013.

[11] Courtesy of Dipl.-Ing. Dr.techn. Thomas Haber, ams AG, Unterpremstätten, Austria, 2013.

[12] FEI Company, Achtseweg Noord 5, Bldg, 5651 GG Eindhoven, The Netherlands.

[13] Goldstein, Joseph, et al. *Scanning electron microscopy and X-ray microanalysis: a text for biologists, materials scientists, and geologists*. Springer Science & Business Media, 2012.

[14] Drouin, Dominique, et al. "CASINO V2. 42-A fast and easy-to-use modeling tool for scanning electron microscopy and microanalysis users." *Scanning* 29.3 (2007): 92-101.

[15] Giannuzzi, Lucille A., ed. *Introduction to focusied ion beams: instrumentation, theory, techniques and practice*. Springer Science & Business Media, 2006.

[16] Plank, Harald. "Focused particle beam nano-machining: the next evolution step towards simulation aided process prediction." *Nanotechnology* 26.5 (2015): 050501

[17] Alkemade, P.F.A, and H. Miro. "Focused helium-ion-beam-induced deposition." *Applied Physics A* 117.4 (2014): 1727-1747.

[18] Ziegler, James F., Matthias D. Ziegler, and Jochen P. Biersack. *SRIM*. Cadence Design Systems, 2008.

[19] Volkert, Cynthia A., and Andrew M. Minor. "Focused ion beam microscopy and micromachining." *MRS bulletin* 32.05 (2007): 389-399.

[20] Schmied, Roland, et al. "New possibilities for soft matter applications: eliminating technically induced thermal stress during FIB processing." *RSC Advances* 2.17 (2012): 6932-6938.

[21] Orthacker, A., et al. "Chemical degradation and morphological instabilities during focused ion beam prototyping of polymers." *Physical Chemistry Chemical Physics* 16.4 (2014): 1658-1666.

[22] Plank, Harald, et al. „Chemical tuning of PtC nanostructures fabricated via focused electron beam induced deposition." *Nanotechnology* 24.17 (2013): 175305

[23] Winkler, Robert, et al. "The nanoscale implications of a molecular gas beam during electron beam induced deposition." *ACS applied materials & interfaces* 6.4 (2014): 2987 – 2995

[24] Wnuk, Joshua D., et al. "Electron induced surface reactions of the organometallic precursor trimethyl (methylcyclopentadienyl) platinum (IV)" *The journal of Physical Chemistry C* 113.6 (2009): 2487-2496.

[25] F. Kolb et al., “Variable tunneling barriers in FEBID based PtC metal-matrix nanocomposites as a transducing element for humidity sensing.” *Nanotechnology*, 23.30, 2013, 305501

[26] Huth, Michael, Florian Kolb, and Harald Plank. “Dielectric sensing by charging energy modulation in a nano-granular metal.” *Applied Physcs A* 117.4 (2014): 1689-1696.

[27] Geier, Barbara et al. , “Rapid and Highly Compact Purification for Focused Electron Beam Induced Deposits: A Low Temperature Approach Using Electron Stimulated H2O Reactions” *The Journal of Physical Chemistry C*, 118.25 (2014), 14009 - 14016

[28] Huth, Michael, et al. „Focused electron beam induced deposition: A perspective.“ *Beilstein journal of nanotechnology* 3.1 (2012): 597-619.

[29] Sachser, Roland, et al. “Universal conductance correction in a tunable strongly coupled nanogranular metal.” *Physical review letters* 107.20 (2011): 206803.

[30] Plank, Harald, et al. „Optimization of postgrowth electron-beam curing for focused electron-beam-induced Pt deposits“ *Journal of Vacuum Science & Technology B* 29.5 (2011): 051801

[31] Reguer, A., et al. „Structural and electrical studies of conductive nanowires prepared by focused ion beam induced deposition.“ *Journal of Vacuum Science & Technology B* 26.1 (2008): 175 - 180

[32] Courtesy of Prof. Dr. Grogger, Institute for Electron Microscopy and Nanoanalysis, Graz University of Technology, Austria, 2013.

[33] D.B. Williams and C.B. Carter. *Transmission Electron Microscopy: A Textbook for Materials Science*, Springer 2009

[34] Kleindiek Prober Shuttle (PS4) manual.

[35] Winkler Robert, et al. “Toward Ultraflat Surface Morphologies During Focused Electron Beam Induced Nanosynthesis: Disruption Origins and Compensation.” *ACS applied materials & interfaces* 7.5 (2015): 3289-3297.

[36] Friedlie, V., and I. Utke. „Optimized molecule supply from nozzle-based gas injection systems for focused electron- and ion-beam induced deposition and etching: simulation and experiment.“ *Journal of Physics D: Applied Physics* 42.12 (2009): 125305.

[37] Langford, R.M., T-X. Wang, and D. Ozkaya. “Reducing the resistivity of electron and ion beam assisted deposited Pt.” *Microelectronic Engineering*, 84.5 (2007): 784-788.

[38] Lipp, S., et al. “A comparison of focused ion beam and electron beam induced deposition processes.” *Microelectronics Reliability* 36.11 (1996): 1779-1782.

[39] Puretz, J. and L. W. Swanson. “Focused ion beam deposition of Pt containing films.” *Journal of Vacuum Science & Technology B* 10.6 (1992): 2695-2698.

[40] Faraby, H., M. DiBattista, and P.R. Bandaru. “Percolation of gallium dominates the electrical resistance of focused ion beam deposited metals.” *Applied Physics Letters* 104.17 (2014): 173107.

[41] Esposito, Marco, et al. „Nanoscale 3D Chiral Plasmonic Helices with Circular Dichroism at Visible Frequencies.“ *ACS Photonics* 2.1 (2014): 105-114.